



NAVAL  
POSTGRADUATE  
SCHOOL

MONTEREY, CALIFORNIA

**DISSERTATION**

**COUPLED FINITE ELEMENT AND CELLULAR  
AUTOMATA METHODS FOR ANALYSIS OF COMPOSITE  
STRUCTURES IN AN ACOUSTIC DOMAIN**

by

Linda E. Craugh

September 2012

Dissertation Supervisor:

Young W. Kwon

**Approved for public release; distribution is unlimited**

THIS PAGE INTENTIONALLY LEFT BLANK

REPORT DOCUMENTATION PAGE			Form Approved OMB No. 0704-0188	
Public reporting burden for this collection of information is estimated to average 1 hour per response, including the time for reviewing instruction, searching existing data sources, gathering and maintaining the data needed, and completing and reviewing the collection of information. Send comments regarding this burden estimate or any other aspect of this collection of information, including suggestions for reducing this burden, to Washington headquarters Services, Directorate for Information Operations and Reports, 1215 Jefferson Davis Highway, Suite 1204, Arlington, VA 22202-4302, and to the Office of Management and Budget, Paperwork Reduction Project (0704-0188) Washington DC 20503.				
<b>1. AGENCY USE ONLY (Leave blank)</b>		<b>2. REPORT DATE</b> September 2012	<b>3. REPORT TYPE AND DATES COVERED</b> Dissertation	
<b>4. TITLE AND SUBTITLE:</b> Coupled Finite Element and Cellular Automata Methods for Analysis of Composite Structures in an Acoustic Domain			<b>5. FUNDING NUMBERS</b>	
<b>6. AUTHOR(S):</b> Linda E. Craugh				
<b>7. PERFORMING ORGANIZATION NAME(S) AND ADDRESS(ES)</b>			<b>8. PERFORMING ORGANIZATION REPORT NUMBER</b>	
<b>9. SPONSORING/MONITORING AGENCY NAME(S) AND ADDRESS(ES)</b>			<b>10. SPONSORING/MONITORING AGENCY REPORT NUMBER</b>	
<b>11. SUPPLEMENTARY NOTES:</b> The views expressed in this thesis are those of the author and do not reflect the official policy or position of the Department of Defense or the U.S. Government. IRB Protocol Number: NA				
<b>12a. DISTRIBUTION / AVAILABILITY STATEMENT</b> Approved for public release; distribution is unlimited			<b>12b. DISTRIBUTION CODE</b> A	
<b>13. ABSTRACT (maximum 200 words)</b> This study examines various computational techniques to analyze dynamic response and failure of sandwich composite materials subject to fluid-structure interaction characterized by an acoustic field or the propagation of velocity potential according to the wave equation. A displacement-only plate finite element is developed and implemented using Discontinuous Galerkin (DG) methodology; its accuracy compares favorably to both theory and Continuous Galerkin methods. Several approaches to analyzing debonding failure between skin and core layers of sandwich composite structures are demonstrated and evaluated; partial disconnection between neighboring elements at a debonding site shows good qualitative agreement with known physical phenomena. A hybrid Finite Element-Cellular Automata (FE+CA) approach to modeling an acoustic field with non-reflecting boundary conditions is presented, validated numerically, and favorably compared with experimental results. The FE+CA fluid model is then combined with the DG structural model to simulate fluid-structure interaction; this combined model compared favorably with experimental results for the strain field of laminated plates subject to low-velocity impact. Each technique addressed shows promise for flexible and accurate modeling of failure initiation and propagation in sandwich and laminate composites subject to fluid-structure interaction with moderate computational costs.				
<b>14. SUBJECT TERMS</b> Discontinuous Galerkin, sandwich composites, Cellular Automata, fluid-structure interaction, failure, delamination, debonding, finite difference			<b>15. NUMBER OF PAGES</b> 137	
			<b>16. PRICE CODE</b>	
<b>17. SECURITY CLASSIFICATION OF REPORT</b> Unclassified	<b>18. SECURITY CLASSIFICATION OF THIS PAGE</b> Unclassified	<b>19. SECURITY CLASSIFICATION OF ABSTRACT</b> Unclassified	<b>20. LIMITATION OF ABSTRACT</b> UU	

THIS PAGE INTENTIONALLY LEFT BLANK

**Approved for public release; distribution is unlimited**

**COUPLED FINITE ELEMENT AND CELLULAR AUTOMATA METHODS FOR  
ANALYSIS OF COMPOSITE STRUCTURES IN AN ACOUSTIC DOMAIN**

Linda E. Craugh  
Commander, United States Navy  
B.S., Cornell University, 1991  
M.S., Naval Postgraduate School, 1999

Submitted in partial fulfillment of the  
requirements for the degree of

**DOCTOR OF PHILOSOPHY IN  
MECHANICAL ENGINEERING**

from the

**NAVAL POSTGRADUATE SCHOOL  
September 2012**

Author:

---

Linda E. Craugh

Approved By:

---

Young W. Kwon  
Distinguished Professor  
Dept. of Mech. & Aero. Engineering  
Dissertation Committee Chair

---

Garth V. Hobson  
Professor  
Dept. of Mech. & Aero. Engineering

---

Joshua H. Gordis  
Associate Professor  
Dept. of Mech. & Aero. Engineering

---

Clyde L. Scandrett  
Professor  
Dept. of Applied Mathematics

---

Francis X. Giraldo  
Professor  
Dept. of Applied Mathematics

Approved By:

---

Knox T. Millsaps, Professor & Chair, Dept. of Mechanical & Aerospace Engineering

Approved By:

---

Doug Moses, Vice Provost for Academic Affairs

THIS PAGE INTENTIONALLY LEFT BLANK

## ABSTRACT

This study examines various computational techniques to analyze dynamic response and failure of sandwich composite materials subject to fluid-structure interaction characterized by an acoustic field or the propagation of velocity potential according to the wave equation. A displacement-only plate finite element is developed and implemented using Discontinuous Galerkin (DG) methodology; its accuracy compares favorably to both theory and Continuous Galerkin methods. Several approaches to analyzing debonding failure between skin and core layers of sandwich composite structures are demonstrated and evaluated; partial disconnection between neighboring elements at a debonding site shows good qualitative agreement with known physical phenomena. A hybrid Finite Element-Cellular Automata (FE+CA) approach to modeling an acoustic field with non-reflecting boundary conditions is presented, validated numerically, and favorably compared with experimental results. The FE+CA fluid model is then combined with the DG structural model to simulate fluid-structure interaction; this combined model compared favorably with experimental results for the strain field of laminated plates subject to low-velocity impact. Each technique addressed shows promise for flexible and accurate modeling of failure initiation and propagation in sandwich and laminate composites subject to fluid-structure interaction with moderate computational costs.

THIS PAGE INTENTIONALLY LEFT BLANK

# TABLE OF CONTENTS

<b>I.</b>	<b>INTRODUCTION . . . . .</b>	<b>1</b>
	<b>A. MOTIVATION AND OBJECTIVE . . . . .</b>	<b>1</b>
	<b>B. PRIOR WORK . . . . .</b>	<b>2</b>
	<b>C. ORGANIZATION . . . . .</b>	<b>4</b>
<b>II.</b>	<b>STRUCTURAL MODEL . . . . .</b>	<b>7</b>
	<b>A. LINEAR ELASTICITY . . . . .</b>	<b>7</b>
	<b>B. DISCONTINUOUS GALERKIN FORMULATION . . . . .</b>	<b>9</b>
	<b>1. Solid Element . . . . .</b>	<b>9</b>
	<b>a. Validation . . . . .</b>	<b>19</b>
	<b>2. Plate Element . . . . .</b>	<b>19</b>
	<b>a. Validation . . . . .</b>	<b>21</b>
	<b>3. Stabilization and Penalty Parameters . . . . .</b>	<b>25</b>
<b>III.</b>	<b>COMPOSITE STRUCTURES . . . . .</b>	<b>27</b>
	<b>A. MULTI-SCALE MODEL . . . . .</b>	<b>27</b>
	<b>B. SANDWICH COMPOSITES . . . . .</b>	<b>28</b>
	<b>C. FAILURE MODES AND IDENTIFICATION . . . . .</b>	<b>32</b>
	<b>D. FAILURE MODELING . . . . .</b>	<b>37</b>
	<b>1. Damage via Complete Disconnection . . . . .</b>	<b>37</b>
	<b>2. Damage via Partial Disconnection . . . . .</b>	<b>42</b>
	<b>3. Damage via Reduced Moduli . . . . .</b>	<b>47</b>
	<b>E. SYNTHESIS . . . . .</b>	<b>50</b>
<b>IV.</b>	<b>FLUID MODEL . . . . .</b>	<b>51</b>
	<b>A. VELOCITY POTENTIAL AND WAVE EQUATION THEORY . . . . .</b>	<b>51</b>
	<b>B. FINITE ELEMENT MODEL OF THE WAVE EQUATION . . . . .</b>	<b>53</b>
	<b>C. CELLULAR AUTOMATA MODEL OF THE WAVE EQUATION . . . . .</b>	<b>54</b>
	<b>1. One Dimension . . . . .</b>	<b>55</b>
	<b>2. Boundary Conditions . . . . .</b>	<b>57</b>
	<b>3. Discretization and Model Fidelity . . . . .</b>	<b>58</b>
	<b>4. Convergence . . . . .</b>	<b>62</b>
	<b>5. Three Dimensions . . . . .</b>	<b>63</b>

D.	COUPLING OF FINITE ELEMENT AND CELLULAR AUTOMATA MODELS OF THE WAVE EQUATION . . . . .	68
1.	Comparison with Homogeneous Fluid Domain . . . . .	73
V.	RESULTS . . . . .	75
A.	ACOUSTIC FIELD FLUID-STRUCTURE INTERACTION . . . . .	75
1.	Information Exchange . . . . .	75
2.	Homogeneous Isotropic Single-Layer Structure . . . . .	75
3.	Two-layer Plates . . . . .	78
4.	Three-layer Plates . . . . .	81
B.	EXPERIMENTAL VALIDATION . . . . .	86
VI.	CONCLUSION . . . . .	95
A.	SUMMARY OF FINDINGS . . . . .	95
B.	FUTURE WORK . . . . .	96
	APPENDIX A. TIME INTEGRATION ALGORITHMS . . . . .	98
A.	NEWMARK- $\beta$ METHOD . . . . .	99
B.	$\alpha$ -METHOD . . . . .	100
C.	TIME DISCONTINUOUS GALERKIN METHOD . . . . .	100
	APPENDIX B. IMPLEMENTATION DETAILS . . . . .	103
A.	MESHING . . . . .	103
B.	NUMERICAL INTEGRATION . . . . .	103
C.	APPLICATION OF BOUNDARY CONDITIONS AND EXTER- NAL LOADS . . . . .	104
D.	MATLAB SPECIFICS . . . . .	105
1.	Sparse Matrices . . . . .	105
2.	CA Implementation . . . . .	105
E.	MATERIAL PROPERTIES . . . . .	106
	LIST OF REFERENCES . . . . .	109
	INITIAL DISTRIBUTION LIST . . . . .	115

## LIST OF FIGURES

Figure 1.	Canonical hexahedral finite element . . . . .	9
Figure 2.	Connectivity between adjacent Continuous Galerkin (CG) elements. After [31] . . . . .	16
Figure 3.	Connectivity between adjacent Discontinuous Galerkin (DG) elements. After [31] . . . . .	17
Figure 4.	Sparsity pattern of CG global stiffness matrix for a 4x2x1 element structure . . . . .	17
Figure 5.	Sparsity pattern of DG global stiffness matrix for a 4x2x1 element structure . . . . .	18
Figure 6.	Convergence of three-dimensional DG formulation vs. discretization for cantilever beam deflection . . . . .	19
Figure 7.	Convergence of three-dimensional DG formulation vs. discretization for simply-supported beam deflection . . . . .	20
Figure 8.	Convergence of center deflection of a clamped plate comprised of plate elements . . . . .	22
Figure 9.	Comparison of displacement calculated for Continuous Galerkin and Discontinuous Galerkin models of a center loaded clamped plate . . . .	23
Figure 10.	Comparison of velocity calculated for Continuous Galerkin and Dis- continuous Galerkin models of a center loaded clamped plate . . . . .	23
Figure 11.	Convergence of central deflection of uniformly loaded clamped lam- inated plate, comparison with [34] . . . . .	24
Figure 12.	Multi-scale analysis cycle for a fibrous composite. From [40] . . . . .	28
Figure 13.	Three and Five Layer Sandwich Plate models . . . . .	29
Figure 14.	Convergence of DG Sandwich Plate max deflection (due to uniform load) to predicted, comparison with [41, 42] . . . . .	31
Figure 15.	Relative convergence of DG Sandwich Plate max deflection and skin stress (due to concentrated load) . . . . .	31
Figure 16.	Planar stress on the skin of a clamped three-layer sandwich plate sub- ject to concentrated center force . . . . .	33
Figure 17.	Planar stress on the core of a clamped three-layer sandwich plate sub- ject to concentrated center force . . . . .	34
Figure 18.	Planar stress on the skin of a clamped five-layer sandwich plate sub- ject to concentrated center force . . . . .	34
Figure 19.	Planar stress on the core of a clamped five-layer sandwich plate sub- ject to concentrated center force . . . . .	35

Figure 20.	Planar stress on the bottom of a resin layer of a clamped five-layer sandwich plate subject to concentrated center force . . . . .	35
Figure 21.	Planar stress on the top of a resin layer of a clamped five-layer sandwich plate subject to concentrated center force . . . . .	36
Figure 22.	Planar stress on the skin of a damaged via complete disconnection clamped five-layer sandwich plate subject to concentrated center force	39
Figure 23.	Planar stress on the core of a damaged (via complete disconnection) clamped five-layer sandwich plate subject to concentrated center force	39
Figure 24.	Planar stress on the bottom of the resin layer of a damaged (via complete disconnection) clamped five-layer sandwich plate subject to concentrated center force . . . . .	40
Figure 25.	Planar stress on the top of the resin layer of a damaged (via complete disconnection) clamped five-layer sandwich plate subject to concentrated center force . . . . .	40
Figure 26.	Static deflection along centerline of damaged (via complete disconnection) clamped five-layer sandwich plate subject to concentrated center force . . . . .	41
Figure 27.	Planar stress on the skin of a damaged (by partial disconnection clamped) five-layer sandwich plate subject to concentrated center force . . . . .	43
Figure 28.	Planar stress on the core of a damaged (by partial disconnection clamped) five-layer sandwich plate subject to concentrated center force . . . . .	43
Figure 29.	Planar stress on the bottom of the resin layer of a damaged (by partial disconnection) clamped five-layer sandwich plate subject to concentrated center force . . . . .	44
Figure 30.	Planar stress on the top of the resin layer of a damaged (by partial disconnection) clamped five-layer sandwich plate subject to concentrated center force . . . . .	44
Figure 31.	Static deflection along centerline of damaged (via partial disconnection) five-layer sandwich plate subject to concentrated center force . . . . .	45
Figure 32.	Planar stress on the skin of a damaged (by partial disconnection) clamped five-layer sandwich plate subject to concentrated center force, fine view . . . . .	45
Figure 33.	Planar stress on the core of a damaged (by partial disconnection) clamped five-layer sandwich plate subject to concentrated center force, fine view . . . . .	46
Figure 34.	Planar stress in the resin layer of a damaged (by partial disconnection) clamped five-layer sandwich plate subject to concentrated center force, fine view . . . . .	46

Figure 35.	Planar stress on the skin of a damaged (by reduced modulus) clamped five-layer sandwich plate subject to concentrated center force . . . . .	47
Figure 36.	Planar stress on the core of a damaged (by reduced modulus) clamped five-layer sandwich plate subject to concentrated center force . . . . .	48
Figure 37.	Planar stress on the bottom of the resin layer of a damaged (by reduced modulus) clamped five-layer sandwich plate subject to concentrated center force . . . . .	48
Figure 38.	Planar stress on the top of the resin layer of a damaged (by reduced modulus) clamped five-layer sandwich plate subject to concentrated center force . . . . .	49
Figure 39.	Center node (black) and its Von Neumann neighbors (white) . . . . .	55
Figure 40.	Initial perturbation of an infinite string . . . . .	56
Figure 41.	CA solution vs. D'Alembert's solution to the one-dimensional wave equation in an infinite string . . . . .	57
Figure 42.	Virtual cell values for various boundary conditions in one dimension. After [25] . . . . .	58
Figure 43.	Application of various boundary conditions to CA calculation of one-dimensional wave propagation . . . . .	59
Figure 44.	Initial perturbations of varying widths . . . . .	60
Figure 45.	CA solution to 1d wave equation convergence as a function of $dx$ for various initial conditions . . . . .	60
Figure 46.	Critical discretization vs. initial perturbation width . . . . .	61
Figure 47.	Convergence of CA wave equation rule to analytic solution as a function of $dx$ . . . . .	62
Figure 48.	Three-dimensional wave model at domain origin: time vs. iterations .	64
Figure 49.	Three-dimensional wave model at a point inside the initial perturbation: time vs. iterations . . . . .	65
Figure 50.	Three-dimensional wave model at a point outside the initial perturbation: time vs. iterations . . . . .	65
Figure 51.	Three-dimensional wave model at a point inside the initial perturbation: analytic solution vs time, CA solution vs $\frac{dx}{c}$ . . . . .	66
Figure 52.	Three-dimensional wave model at a domain origin . . . . .	66
Figure 53.	Three-dimensional wave model at a point inside the initial perturbation	67
Figure 54.	Three-dimensional wave model at a point outside the initial perturbation	67
Figure 55.	Finite Element fluid domain surrounded by Cellular Automata fluid domain . . . . .	69
Figure 56.	Node sets for exchange of data between fluid domains . . . . .	70

Figure 57.	Comparison of velocity potential propagation between finite element and cellular automata models with common Dirichlet boundary conditions . . . . .	71
Figure 58.	Velocity potential propagation between finite element and cellular automata domains, velocity potential ( $\phi(\text{top})$ ) specified . . . . .	71
Figure 59.	Velocity potential propagation between finite element and cellular automata domains, velocity ( $v(\text{top})$ ) specified . . . . .	72
Figure 60.	Velocity potential propagation between finite element and cellular automata domains, FE inside CA, velocity ( $v(\text{top})$ ) specified, non-reflecting boundary conditions . . . . .	72
Figure 61.	Comparison of velocity potential at mid-domain resulting from specified value on one face: FE + CA domain vs. homogeneous CA domain	73
Figure 62.	Displacement of clamped plate with and without fluid-structure interaction . . . . .	76
Figure 63.	Displacement of clamped plate of double modulus with and without fluid-structure interaction . . . . .	77
Figure 64.	Displacement of clamped plate of double density with and without fluid-structure interaction . . . . .	77
Figure 65.	Displacement of damaged clamped two layer E-glass plate with and without fluid-structure interaction . . . . .	79
Figure 66.	Velocity of damaged clamped plate two layer E-glass plate with and without fluid-structure interaction . . . . .	79
Figure 67.	Strain at center of clamped two layer E-glass plate with and without fluid-structure interaction . . . . .	80
Figure 68.	Strain at center and edge of damage zone of clamped two layer E-glass plate with and without fluid-structure interaction . . . . .	80
Figure 69.	Displacement of clamped three layer E-glass plate with and without fluid-structure interaction and with and without damage . . . . .	81
Figure 70.	Velocity of clamped three layer E-glass plate with and without fluid-structure interaction and with and without damage . . . . .	82
Figure 71.	Strain of clamped three layer E-glass plate with and without fluid-structure interaction and with and without damage at center of lower E-glass layer . . . . .	82
Figure 72.	Strain of clamped three layer E-glass plate with and without fluid-structure interaction and with and without damage at center of interface layer . . . . .	83
Figure 73.	Strains in dry clamped three layer E-glass plate with and without damage . . . . .	84

Figure 74.	Strains in wet clamped three layer E-glass plate with and without damage . . . . .	85
Figure 75.	Schematic of Vacuum Assisted Resin Transfer Molding technique (VARTM) for plate manufacture. From [49] . . . . .	86
Figure 76.	Drop Weight Rig used in Impact Testing. From [48] . . . . .	87
Figure 77.	Drop Weight Rig as used for Impact Testing with Fluid-Structure Interaction (FSI). From [48] . . . . .	88
Figure 78.	Raw and smoothed experimental force data for dry plate . . . . .	89
Figure 79.	Measured versus calculated strain, dry plate, gage 1 . . . . .	90
Figure 80.	Measured versus calculated strain, dry plate, gage 2 . . . . .	90
Figure 81.	Measured versus calculated strain, dry plate, gage 3 . . . . .	91
Figure 82.	Raw and smoothed experimental force data for wet plate . . . . .	91
Figure 83.	Measured versus calculated strain, wet plate, gage 1 . . . . .	92
Figure 84.	Measured versus calculated strain, wet plate, gage 2 . . . . .	92
Figure 85.	Measured versus calculated strain, wet plate, gage 3 . . . . .	93
Figure 86.	Temporal elements for TDG method. From [55] . . . . .	102

THIS PAGE INTENTIONALLY LEFT BLANK

## LIST OF ACRONYMS AND NOMENCLATURE

<b>CA</b>	Cellular Automata
<b>CG</b>	Continuous Galerkin
$\delta_p$	penalty parameter
<b>DG</b>	Discontinuous Galerkin
<b>dof</b>	degree(s) of freedom
$\varepsilon_x$	$x$ component of strain
$\varepsilon_y$	$y$ component of strain
<b>FE</b>	Finite Element
<b>FEM</b>	Finite Element Method
<b>FSI</b>	Fluid-Structure Interaction
<b>IIPG</b>	Incomplete Interior Penalty Galerkin
<b>LDG</b>	Local Discontinuous Galerkin
<b>NIPG</b>	Non-symmetric Interior Penalty Galerkin
<b>OBB</b>	Oden, Babuska, and Baumann
<b>SIPG</b>	Symmetric Interior Penalty Galerkin
$\sigma_x$	$x$ component of stress
$\theta_{DG}$	DG method selector
<b>TDG</b>	Time Discontinuous Galerkin
<b>TSF</b>	time scaling factor
<b>VARTM</b>	Vacuum Assisted Resin Transfer Molding technique

THIS PAGE INTENTIONALLY LEFT BLANK

## LIST OF TABLES

Table 1.	Comparison of maximum planar stress values (in MPa) and locations for damaged and undamaged clamped sandwich plates subject to a concentrated center force . . . . .	50
Table 2.	Material Properties of aluminum honeycomb, From [41], [42] . . . . .	106
Table 3.	Material Properties of aluminum skins, From [41], [42] . . . . .	106
Table 4.	Material Properties of E-glass, From [56] . . . . .	106
Table 5.	Material Properties of Epoxy Resin, From [57] . . . . .	107

THIS PAGE INTENTIONALLY LEFT BLANK

## ACKNOWLEDGEMENTS

This work is dedicated to the memory of my grandparents, Thomas P. and Doris E. Lawn and Edward A. and Margaret F. Craugh, who taught in word and deed the value of education. It would not have been possible without the love and support of my parents, sisters, and their families; in particular, my nieces Sasha, Sarah, and Anna Maslowski and my goddaughter Sarah Haynes inspire me constantly.

I am also indebted to Professor Young Kwon for his guidance and apparently inexhaustible patience.

THIS PAGE INTENTIONALLY LEFT BLANK

# I. INTRODUCTION

## A. MOTIVATION AND OBJECTIVE

Composite materials can have very beneficial properties for structural applications. In particular, polymer composites generally have low density but high strength and stiffness, or a very high specific strength and stiffness. Their resistance to corrosion is another tremendous advantage. Consequently, composite materials are used in a number of both civil and military applications. Aerospace structures are among the major applications of polymer composite materials, especially carbon fiber composites. Increasingly, composite materials are used in marine structures, making their use in Naval applications likewise more common.

One of the major difficulties associated with design and analysis of composite structures is their anisotropic material properties and complex failure modes and mechanisms when compared to metallic structures. Anisotropic composite material behavior can be tailored to optimize their use in structures; however, diverse and inter-connected failure modes in composites remain a challenge for the composite community. Traditional metallic structures differ from composites in one other key aspect: resilience and ductility. That is, their ability to deform and recover in the elastic zone gives the designer a safety margin much larger than that found in the composite world. Composite materials have long been used as primary hull materials for sailboats and other small craft, but the nature of larger Naval applications of composite materials demands a fuller understanding of the survivability and mission impacts of using such structures in the marine environment.

A great deal of research in FSI has been conducted for aerospace applications, tending to focus on the effect of the structure on the fluid field. For marine applications with a polymer composite structure in contact with water, the comparable density of the composite materials to that of water results in a significant hydrodynamic mass effect on the structure. Therefore, the goal of this study is to develop computational techniques to model

and simulate transient dynamic responses and failures of composite structures with FSI. To this end, it is necessary to develop computational techniques for composite structures as well as the fluid medium. Eventually, a method to couple both structural and fluid solvers is developed.

## **B. PRIOR WORK**

The Finite Element Method (FEM) is a well established tool for generating numerical solutions to the partial differential equations that describe a wide range of physical phenomena. In structural solvers, the method combines the geometry and constraints of the structure with the material properties of its components to generate a response (e.g., displacement, stress, and/or strain) to given loading. This is accomplished by treating the structure as a collection of smaller domains (finite elements) of relatively simpler geometry, applying and solving the simpler problem on a smaller scale with constraints dictated by internal compatibility, and then combining the smaller solutions into a global solution. This collection of potentially tedious but simple calculations is an ideal job for a computer. The method of weighted residual used in most finite element codes is a Galerkin method in which the test function is the derivative of the trial function with respect to the unknown variable(s). Requiring continuity between neighboring elements makes physical sense and is the norm, but Discontinuous Galerkin (DG) methods have become an active area of research in the last several decades.

DG approaches to solving boundary-value problems have their genesis in the work of Nitsche [1] who first proposed weak enforcement of boundary conditions. Douglas and Dupont [2], Arnold [3], Baker [4], and Wheeler [5] expanded the concept to weak enforcement of continuity between elements and applied it to elliptic problems. Easing of the continuity constraints between elements suggests a number of potential advantages to this methodology: element-wise computations lend themselves to parallel computing, the independence of the elements from each other allows different orders of interpolation within neighboring elements, and the potential to model failure without having to re-mesh

is intriguing. In recent years discontinuous approaches have been increasingly applied to elliptic partial differential equations such as those that dominate linear elasticity. Arnold and colleagues have produced two excellent overviews of the development and characteristics of various methods in [6] and [7]. In particular, they gathered the various formulations and cast them all in both flux and primal forms to more clearly see the differences and identifying characteristics. Castillo [8] conducted a cost and performance analysis of three of these methods. Brezzi, Cockburn, Marini, and Suli [9] discuss the stabilization mechanisms necessary for effective DG formulations. Specific work in DG for solid mechanics can be found in the List of References, [10] – [22] among many others.

Not all parts of a finite element analysis are of equal interest. A homogeneous beam or plate, for example, can be modeled with relative fidelity with just a few elements; while the analysis of air-flow over a golf ball would require elements of a size comparable to the ball's dimples, which could lead to an exorbitant computational cost for a domain on the order of three ball diameters. The obvious solution to such a dilemma is to selectively refine the mesh in the area of interest while using a mesh as coarse as possible in other parts of the domain. This work seeks to explore the potential of using Discontinuous Galerkin (DG) finite element methodology to enable failure to initiate in its natural location anywhere in the domain.

In analysis of structures consisting of composite materials, multiple scales of analysis can be used in conjunction with each other. That is, the analysis can proceed from the micro- (atomic or molecular) level to the meso- (material) level and on to the macro- (structural) level and back down again as necessary with smearing or decomposition of properties and loads as dictated by the analysis required. The properties of a laminated fibrous composite, for example, are a function of the properties of both fiber and matrix as well as the weave pattern of individual laminae and lay-up pattern of the assembled laminate. Similarly, failure of the same laminate can result from separation between laminae, separation of fibers from matrix, or failure of individual fibers.

To accurately model FSI an appropriate fluid model is also required. In this work no attempt is made to model or solve the full Navier-Stokes equations, a subset that will allow compatibility between fluid and solid regimes and approximate the hydrodynamic pressure or acoustic field will suffice. Olson and Bathe [23] developed a directly coupled formulation that solves for the velocity potential and hydrostatic pressure in the fluid domain and displacements in the structural; this will be the starting point for development of the fluid model in this work. In order to apply the fluid model to a maritime domain, appropriate boundary conditions must also be included. Two general approaches are to model a vast domain and concern oneself with a small subset relatively far from simple but inaccurate boundaries—a computationally expensive proposition—or to model an appropriately sized domain with non-reflecting boundary conditions—a challenging proposition that remains an active area of research [24]. Application of Cellular Automata (CA) to modeling the acoustic field following from the work of Chopard [25, 26], Krutar et al. [27], and Kwon and Hosoglu [28] will be explored.

Increasing application of composite technology in maritime applications requires further work examining the mass effects imparted to composite structures in contact with a fluid environment. In particular, evaluation of damage and residual strength are necessary for a proper evaluation of the survivability potential of a proposed design.

## **C. ORGANIZATION**

The balance of this thesis is organized as follows: Chapter II includes a short review of linear elasticity followed by development of both full three-dimensional and plate elements using DG techniques. Chapter III includes further discussion of the advantages and challenges of composite materials and sandwich plates, validation of the developed DG structural model’s applicability to sandwich constructs, followed with an examination of various failure models. Development and validation of the fluid model incorporating velocity potential formulation and non-reflecting boundary conditions comprises Chapter IV. Chapter V contains a demonstration of the coupling of the fluid and structural models

as well as comparisons with experimental work [29]. Conclusions and recommendations for continuing research in this vein will be addressed in Chapter VI.

THIS PAGE INTENTIONALLY LEFT BLANK

## II. STRUCTURAL MODEL

This chapter will discuss the formulation and various components of the structural models used in this work. After first reviewing the equation(s) to be solved and traditional numerical approaches, Discontinuous Galerkin (DG) methods will be discussed in general followed by a detailed formulation for a three-dimensional solid element. That approach will be modified to model a plate element. A discussion of the sensitivities of each element to discretization and penalty parameters will ensue.

### A. LINEAR ELASTICITY

In Voigt notation, the governing equation for the static structural model is the equation of equilibrium,

$$\nabla \cdot \vec{\sigma} + \vec{f} = 0 \quad (1)$$

in which

$$\vec{\sigma} = \{\sigma_x \ \sigma_y \ \sigma_z \ \tau_{xy} \ \tau_{yz} \ \tau_{xz}\}^T \quad (2)$$

is the stress vector and

$$\vec{f} = \{f_x \ f_y \ f_z\}^T \quad (3)$$

is the body force vector. Combining the constitutive equation of generalized Hooke's Law,

$$\vec{\sigma} = [D]\vec{\varepsilon} \quad (4)$$

where  $\vec{\varepsilon} = \{\varepsilon_x \ \varepsilon_y \ \varepsilon_z \ \gamma_{xy} \ \gamma_{yz} \ \gamma_{xz}\}^T$  is the strain vector and  $[D]$  is the 6x6 material property matrix, and the kinematic strain-displacement relationship,

$$\vec{\varepsilon} = \frac{1}{2}(\nabla\vec{u} + \nabla\vec{u}^T) \quad (5)$$

in which  $\vec{u} = \{u_x \ u_y \ u_z\}^T = \{u \ v \ w\}^T$ . Equation (1) can be solved for displacement or deflection of a body subject to a load described by  $\vec{f}(x, y, z)$  and appropriate boundary conditions. Displacement at specified points or nodes in the domain of interest are the unknown quantities or degree(s) of freedom (dof).

The desired solution,  $\vec{u}(x, y, z)$ , is expressed in terms of the displacement vector at each nodal point in the domain and the interpolation functions within each element. If we define  $U$  as the vector of nodal displacements with the three components for each node grouped together,

$$\vec{u}(x, y, z) = N(x, y, z)U \quad (6)$$

where

$$N = \begin{bmatrix} H_1 & 0 & 0 & H_2 & 0 & 0 & \dots & \dots & \dots & H_8 & 0 & 0 \\ 0 & H_1 & 0 & 0 & H_2 & 0 & \dots & \dots & \dots & 0 & H_8 & 0 \\ 0 & 0 & H_1 & 0 & 0 & H_2 & \dots & \dots & \dots & 0 & 0 & H_8 \end{bmatrix} \quad (7)$$

for a three-dimensional hexahedral element where  $H_i$  is the three-dimensional cardinal basis function corresponding to node  $i$ . Similarly, the strain matrix  $[B]$  is defined such that

$$\vec{\varepsilon}(x, y, z) = B(x, y, z)U \quad (8)$$

$$B = \begin{bmatrix} \frac{\partial H_1}{\partial x} & 0 & 0 & \frac{\partial H_2}{\partial x} & 0 & 0 & \dots & \dots & \dots & \frac{\partial H_8}{\partial x} & 0 & 0 \\ 0 & \frac{\partial H_1}{\partial y} & 0 & 0 & \frac{\partial H_2}{\partial y} & 0 & \dots & \dots & \dots & 0 & \frac{\partial H_8}{\partial y} & 0 \\ 0 & 0 & \frac{\partial H_1}{\partial z} & 0 & 0 & \frac{\partial H_2}{\partial z} & \dots & \dots & \dots & 0 & 0 & \frac{\partial H_8}{\partial z} \\ \frac{\partial H_1}{\partial y} & \frac{\partial H_1}{\partial x} & 0 & \frac{\partial H_2}{\partial y} & \frac{\partial H_2}{\partial x} & 0 & \dots & \dots & \dots & \frac{\partial H_8}{\partial y} & \frac{\partial H_8}{\partial x} & 0 \\ 0 & \frac{\partial H_1}{\partial z} & \frac{\partial H_1}{\partial y} & 0 & \frac{\partial H_2}{\partial z} & \frac{\partial H_2}{\partial y} & \dots & \dots & \dots & 0 & \frac{\partial H_8}{\partial z} & \frac{\partial H_8}{\partial y} \\ \frac{\partial H_1}{\partial z} & 0 & \frac{\partial H_1}{\partial x} & \frac{\partial H_2}{\partial z} & 0 & \frac{\partial H_2}{\partial x} & \dots & \dots & \dots & \frac{\partial H_8}{\partial z} & 0 & \frac{\partial H_8}{\partial x} \end{bmatrix} \quad (9)$$

and

$$\vec{\sigma}(x, y, z) = [D]B(x, y, z)U. \quad (10)$$

The dimensions of these elemental matrices and vectors for tri-linear three-dimensional hexahedral elements are  $[U] = 24 \times 1$  (8 nodes, 3 degrees of freedom per node),  $[N] = 3 \times 24$ ,  $[B] = 6 \times 24$ , and  $[D] = 6 \times 6$ .  $U$  can then be post-processed to calculate the stress and strain fields as necessary. Figure 1 shows a notional hexahedral finite element of the sort used here.

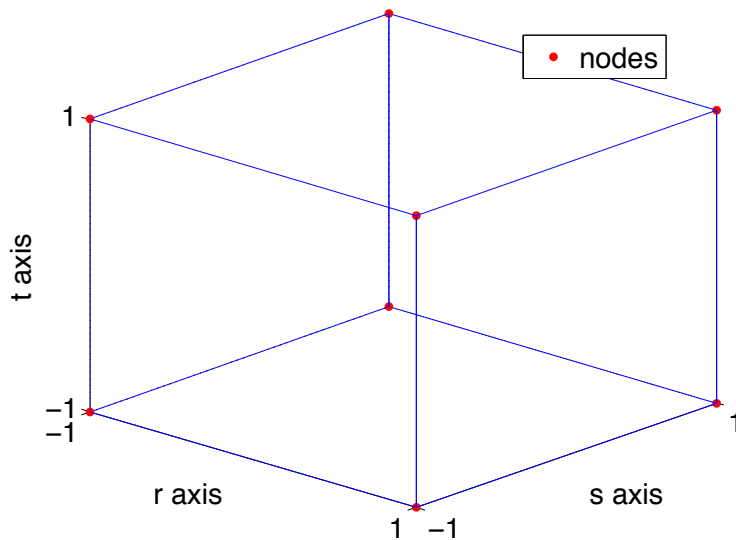


Figure 1: Canonical hexahedral finite element

## B. DISCONTINUOUS GALERKIN FORMULATION

This section will detail the formulation of nodal DG solid (three-dimensional) and plate elements to be used to solve for the displacement field in a given linearly elastic structure. The plate element to be developed is based on Reissner-Mindlin theory but all dof are displacements.

### 1. Solid Element

Liu, Wheeler, and Dawson [21] proposed and implemented a nodal DG formulation that can be simply coupled with existing codes for continuous models and can be switched

between three different specific methods via the selection of a single scalar parameter,  $\theta_{DG}$ . Their formulation is the starting point for this work and is summarized below.

The domain,  $\Omega \subset R^3$ , has a boundary,  $\partial\Omega$ , comprised of non-intersecting Dirichlet,  $\Gamma_u$ , and Neumann,  $\Gamma_t$ , boundaries upon which displacement,  $\bar{u} \in H^1(\Gamma_u)$ , and surface traction,  $\bar{t} \in L^2(\Gamma_t)$  are specified.  $\chi = \{E_1, E_2, \dots, E_N\}$  is a non-degenerate discretization of  $\Omega$ ; in this work,  $E_j$  are hexahedra.  $S = S_i + \Gamma_u + \Gamma_t$  is the set of faces of  $\chi$  where  $S_i$  are interior faces.

Following standard weighted residual methodology, Equation (1) is multiplied by a test function and integrated over the domain with the intent of finding a solution that leaves no residual from that integral. Since this is a Galerkin formulation, the test function to be used is the interpolation function used in the discretization of the domain; as a Discontinuous Galerkin formulation the test function need only be defined within each element. Symbolically,

$$\int_E \sigma(u) : \nabla v dV - \int_{\partial E} (\sigma n) \cdot v dS = \int_E f \cdot v dV. \quad (11)$$

Taking advantage of the fact that

$$\sigma(u) : \nabla v = \sigma(u) : \nabla v^T = \sigma(u) : \varepsilon(v) \quad (12)$$

the elemental equation in question is

$$\int_E \sigma(u) : \varepsilon(v) dV - \int_{\partial E} (\sigma n) \cdot v dS = \int_E f \cdot v dV. \quad (13)$$

Or, summed over all elements,

$$\sum_{E \in \chi} \int_E \sigma(u) : \varepsilon(v) dV - \sum_{\partial E \in S} \int_{\partial E} (\sigma n) \cdot v dS = \sum_{E \in \chi} \int_E f \cdot v dV. \quad (14)$$

In a continuous formulation the second term of the last equation would disappear on inter-elemental boundaries and only exist on the domain boundary; for DG, however, that is not the case. Define jump and average functions across such an interior boundary, between two

elements arbitrarily labeled as “Left” and “Right” as

$$[w] = w_L - w_R \quad (15)$$

$$\{w\} = \frac{1}{2}(w_L + w_R). \quad (16)$$

Combining those definitions with the identity

$$[\phi\varphi] = \{\phi\}[\varphi] + [\phi]\{\varphi\} \quad (17)$$

and the assumption that traction across interfaces is continuous, results in

$$\begin{aligned} \sum_{E \in \mathcal{X}} \int_E \sigma(u) : \epsilon(v) dV - \sum_{\partial E \in (S - \Gamma_u)} \int_{\partial E} \{\sigma(u)n^s\} \cdot [v] dS \\ = \sum_{E \in \mathcal{X}} \int_E f \cdot v dV + \sum_{\partial E \in \Gamma_t} \int_{\partial E} \bar{t} \cdot v dS. \end{aligned} \quad (18)$$

Liu et al. [21] add face integrals  $\int_{\partial E} \{\sigma(v)n^s\} \cdot [u] dS$  and  $\frac{\delta_p G}{|s|} \int_{\partial E} [u] \cdot [v] dS$ , both of which disappear for an exact solution, to control symmetry and provide stabilization; they generate the following bilinear and linear forms:

$$\begin{aligned} a(u, v) = \sum_{E \in \mathcal{X}} \int_E \sigma(u) : \epsilon(v) dV - \sum_{\partial E \in (S_i + \Gamma_u)} \int_{\partial E} \{\sigma(u)n^s\} \cdot [v] dS \\ + \sum_{\partial E \in (S_i + \Gamma_u)} \theta_{DG} \int_{\partial E} \{\sigma(v)n^s\} \cdot [u] dS \\ + \sum_{\partial E \in (S_i + \Gamma_u)} \frac{\delta_p G}{|s|} \int_{\partial E} [u] \cdot [v] dS \end{aligned} \quad (19)$$

$$L(v) = \sum_{E \in \chi} \int_E f \cdot v dV + \sum_{\partial E \in \Gamma_t} \int_{\partial E} \bar{t} \cdot v dS + \sum_{\partial E \in \Gamma_u} \theta_{DG} \int_{\partial E} \{\sigma(v)n^s\} \cdot \bar{u} dS + \sum_{\partial E \in \Gamma_u} \frac{\delta_p G}{|s|} \int_{\partial E} \bar{u} \cdot [v] dS \quad (20)$$

where  $G$  is the shear modulus,  $\delta_p$  is a scalar penalty parameter,  $|s|$  is the square root of the area of the element's face, and  $\theta_{DG}$  indicates the DG method in use. For non-zero  $\delta_p$ , if  $\theta_{DG} = -1$  the method is the Symmetric Interior Penalty Galerkin (SIPG), which also corresponds to the Local Discontinuous Galerkin (LDG) method of Cockburn and Shu with  $\beta = 0$  [30]; if  $\theta_{DG} = +1$  it is Non-symmetric Interior Penalty Galerkin (NIPG); if  $\theta_{DG} = 0$  it is Incomplete Interior Penalty Galerkin (IIPG). If  $\theta_{DG} = 0$  and  $\delta_p = 0$  the method is that of Oden, Babuska, and Baumann (OBB). The problem statement is now: find  $u \in V$  such that

$$a(u, v) = L(v) \quad \forall v \in V \quad (21)$$

$$H^1(\chi) = \{v \in L^2(\Omega) : v|_{E_j} \in H^1(E_j) \forall E_j \in \chi\}; \quad V = \{v \in H^1(\chi)\}. \quad (22)$$

Equations (19) and (20) can be converted into matrix-vector form. The integrand of the first term of (19) is:

$$\sigma(u) : \varepsilon(v) = DB(x, y, z)U : B(x, y, z) = B^T(x, y, z)DB(x, y, z)U. \quad (23)$$

Since  $U$  is independent of  $(x, y, z)$ , it can be taken outside the integral

$$\int_E \sigma(u) : \varepsilon(v) dV = \int_E B^T DB dV U = K_v U \quad (24)$$

so that the matrix,  $K_v$  resulting from the volume integral is multiplied by the displacement vector. This  $K_v$  is the identical to the elemental stiffness matrix common to continuous Galerkin formulations.

In a similar fashion, the surface integrals of Equation (19) can also be expressed as matrix-vector products. Once expanded the vector components will be comprised of

various products of the unknown vector,  $u_L$  or  $u_R$  and the test function,  $v_L$  or  $v_R$ . The interface stiffness matrices will be referred to as  $K_{MN}^i$  where the superscript,  $i$  refers to the integrals in the order they appear in Equation (19); the subscripts will take the values  $L$  and  $R$ , referring to the left and right sides of the interface, respectively. The subscript  $M$  will correspond to the  $v$  component and the  $N$  will correspond to the  $u$  component.

For example, the expansion of the first surface integral into the  $K_{MN}^1$  components is

$$\begin{aligned} \int_S \{\sigma(u)n^s\} \cdot [v]dS &= - \int_S \left( \frac{\sigma(u_L) + \sigma(u_R)}{2} n^s \right) \cdot (v_L - v_R) dS \\ &= -\frac{1}{2} \int_S (\sigma(u_L)n^s) \cdot v_L dS + \frac{1}{2} \int_S (\sigma(u_L)n^s) \cdot v_R dS \\ &\quad - \frac{1}{2} \int_S (\sigma(u_R)n^s) \cdot v_L dS + \frac{1}{2} \int_S (\sigma(u_R)n^s) \cdot v_R dS. \end{aligned} \quad (25)$$

Expressing the normal vector in terms of a matrix of the direction cosines,

$$\Lambda^s = \begin{bmatrix} n_x & 0 & 0 & n_y & 0 & n_z \\ 0 & n_y & 0 & n_x & n_z & 0 \\ 0 & 0 & n_z & 0 & n_y & n_x \end{bmatrix} \quad (26)$$

the terms of Equation (25) can be expressed as

$$-\frac{1}{2} \int_S (\sigma(u_L)n^s) \cdot v_L dS = -\frac{1}{2} \int_S N_L^T \Lambda^s D B_L dS U_L = K_{LL}^1 U_L \quad (27)$$

$$\frac{1}{2} \int_S (\sigma(u_L)n^s) \cdot v_R dS = \frac{1}{2} \int_S N_R^T \Lambda^s D B_L dS U_L = K_{RL}^1 U_L \quad (28)$$

$$-\frac{1}{2} \int_S (\sigma(u_R)n^s) \cdot v_L dS = -\frac{1}{2} \int_S N_L^T \Lambda^s D B_R dS U_R = K_{LR}^1 U_R \quad (29)$$

$$\frac{1}{2} \int_S (\sigma(u_R)n^s) \cdot v_R dS = \frac{1}{2} \int_S N_R^T \Lambda^s D B_R dS U_R = K_{RR}^1 U_R. \quad (30)$$

Conveniently the interface stiffness matrices that result from the third term of (19) are simple re-arrangements of those calculated from the second term. That is,  $K_{LL}^1 = K_{LL}^2{}^T$ ,  $K_{RR}^1 = K_{RR}^2{}^T$ ,  $K_{LR}^1 = K_{RL}^2{}^T$ , and  $K_{RL}^1 = K_{LR}^2{}^T$ . The final term of (19) is referred to as the interface penalty stiffness,  $K_{MN}^3$  and its components are calculated as follows:

$$\begin{aligned} \frac{\delta_p G}{|s|} \int_S [u] \cdot [v] dS &= \frac{\delta_p G}{|s|} \int_S (u_L - u_R)(v_L - v_R) dS \\ &= \frac{\delta_p G}{|s|} \int_S (u_L v_L - u_L v_R - u_R v_L + u_R v_R) dS \end{aligned} \quad (31)$$

$$\frac{\delta_p G}{|s|} \int_S u_L v_L dS = \frac{\delta_p G}{|s|} \int_S N_L^T N_L dS U_L = K_{LL}^3 U_L \quad (32)$$

$$- \frac{\delta_p G}{|s|} \int_S u_L v_R dS = - \frac{\delta_p G}{|s|} \int_S N_R^T N_L dS U_L = K_{RL}^3 U_L \quad (33)$$

$$- \frac{\delta_p G}{|s|} \int_S u_R v_L dS = - \frac{\delta_p G}{|s|} \int_S N_L^T N_R dS U_R = K_{LR}^3 U_R \quad (34)$$

$$\frac{\delta_p G}{|s|} \int_S u_R v_R dS = \frac{\delta_p G}{|s|} \int_S N_R^T N_R dS U_R = K_{RR}^3 U_R. \quad (35)$$

The terms of  $L(v)$  are vectors resulting from integrating the body forces and given boundary conditions (both displacement and traction) over the volume and surfaces.

$$\int_E f \cdot v dV = \int_E N^T f dV = F^b \quad (36)$$

where  $f = (f_x, f_y, f_z)^T$  for the element in question.

$$\int_{\partial E} \bar{t} \cdot v dS = \int_{\partial E} N^T \bar{t} dS = F^t \quad (37)$$

$$\int_{\partial E} \{\sigma(v)n^s\} \cdot \bar{u} dS = \int_{\partial E} B^T D^T (\Lambda^s)^T \bar{u} dS = F^u \quad (38)$$

$$\frac{\delta_p G}{|s|} \int_{\partial E} \bar{u} \cdot [v] dS = \frac{\delta_p G}{|s|} \int_{\partial E} N^T \bar{u} dS = F^p \quad (39)$$

where  $\bar{t} = (t_x, t_y, t_z)^T$  and  $\bar{u} = (u, v, w)^T$  for the boundary face in question.

To ensure each interface integral is calculated once and only once, as the loop through the elements progresses surface integrals are calculated only for those faces corresponding to the positive canonical directions. This convention relies on element numbering also proceeding in the positive directions, or element  $e$ 's  $+r$  neighbor is an element numbered greater than  $e$ .

One of the advantages of discontinuous Galerkin formulations is the independence of the elements with the exception of the numerical fluxes between them. If this were a time-dependent problem or if there were some other source of data about neighboring elements, the various terms of  $a(u, v)$  could be computed for each element using the displacement data from the previous time step as the  $U_R$  terms for its neighbors. In a static treatment, the various  $K_{MN}^i$  matrices will be assembled into a total system stiffness matrix; likewise, the various  $F^i$  vectors will be assembled into a total system force vector and a global  $KU = F$  and solved simultaneously.

Assembly of the global  $[K]$  matrix highlights the most obvious difference between CG and DG methods: the relationships between the elements. Figures 2 and 3 illustrate the relationships between neighboring elements in the two methods. The interface between the DG elements may have the same geometric location initially, but the faces are treated as separate entities; each element's dofs are wholly contained in that element. The CG elements actually share the face/edge and have common nodes and dofs there. Figures 4 and 5 show the connectivity and sparsity patterns for the assembled global stiffness matrices of the same four element by two element by one element discretization generated by the two methods. cursory examination of Figure 5 reveals the elemental connectivity: the full blocks along the diagonal are the eight elemental stiffness matrices; the sparser off-diagonal blocks represent the interfaces. It is apparent, therefore, that element one's neighbors are element two and element five. The connectivity of Figure 4 is related to the individual nodes and dofs as opposed to the elemental connectivity of Figure 5. These two figures also illustrate one of the significant disadvantages of DG methods – a tremendous growth

in the scope of the numerical problem; these two matrices can be used to solve the same physical problem, yet the CG version is only half as large.

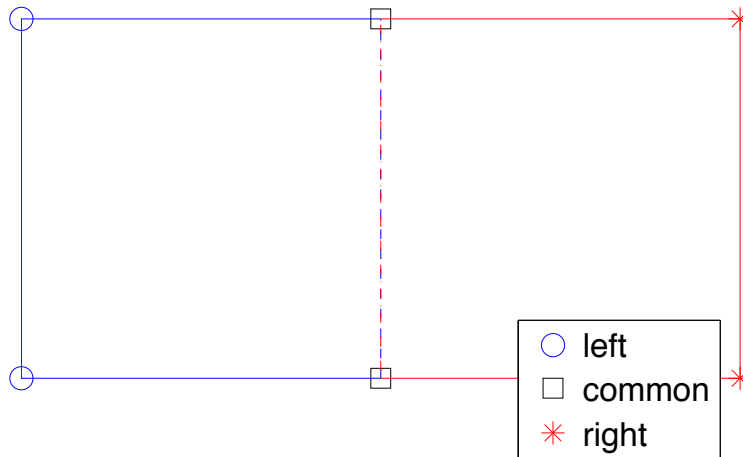


Figure 2: Connectivity between adjacent CG elements. After [31]

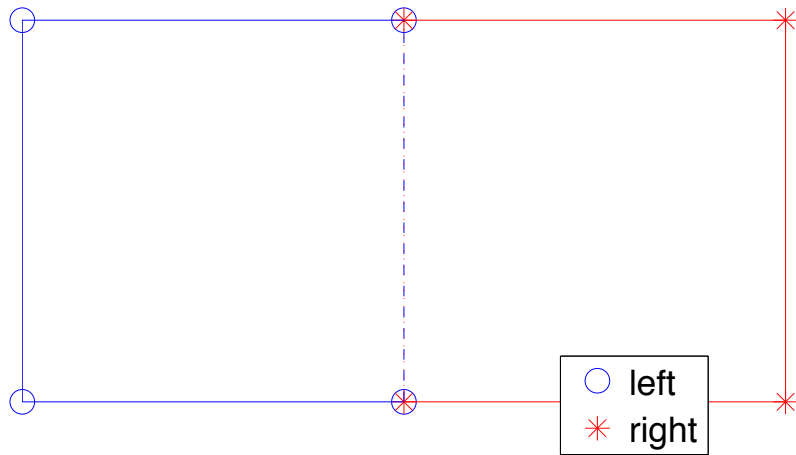


Figure 3: Connectivity between adjacent DG elements. After [31]

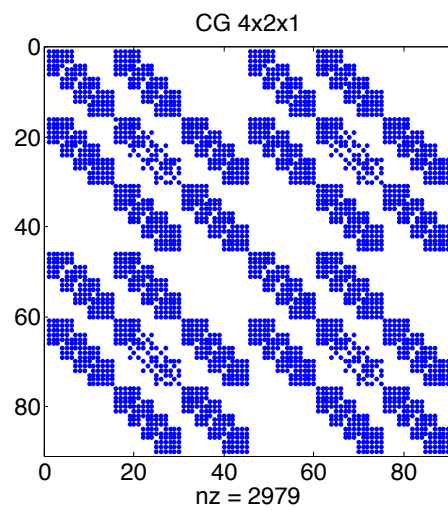


Figure 4: Sparsity pattern of CG global stiffness matrix for a 4x2x1 element structure

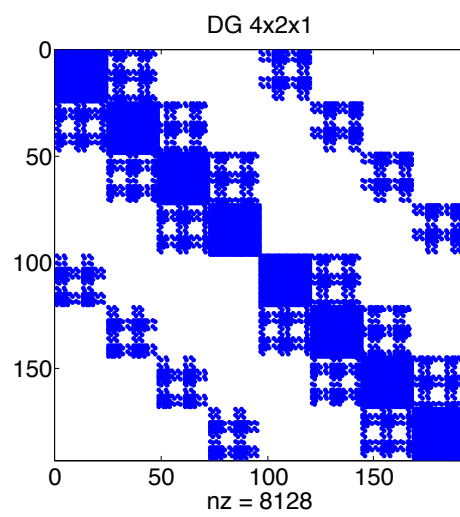


Figure 5: Sparsity pattern of DG global stiffness matrix for a 4x2x1 element structure

*a. Validation*

A pair of beam problems were used to validate code derived from this formulation: a cantilever subjected to a concentrated force at the free end and a simply-supported beam subjected to a concentrated force at mid-span. Both beams are 8m long and have unit cross-sectional area and the same isotropic material properties. Errors relative to maximum deflections predicted by Euler Beam theory were calculated for various discretizations and plotted in Figures 6–7, both of which demonstrate quadratic convergence rates (the predicted rate for linear elements) for all three methods (NIPG, SIPG, IIPG).

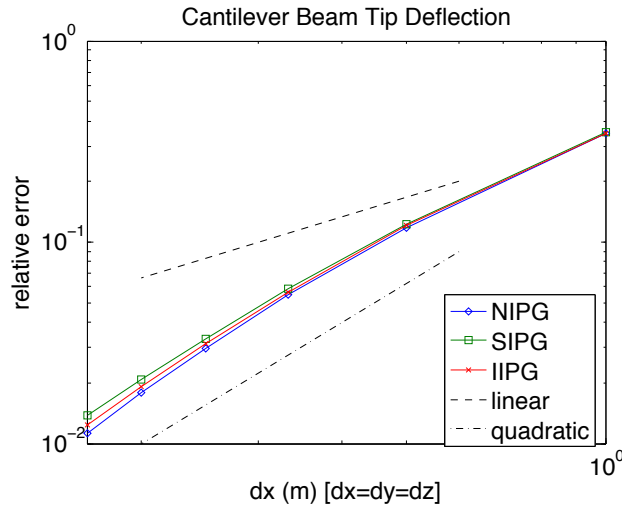


Figure 6: Convergence of three-dimensional DG formulation vs. discretization for cantilever beam deflection

**2. Plate Element**

Adapting the above formulation to different types of elements is a matter of using appropriate  $[N]$ ,  $[B]$ , and  $[D]$  matrices. Kwon and Bang [32] developed a displacement

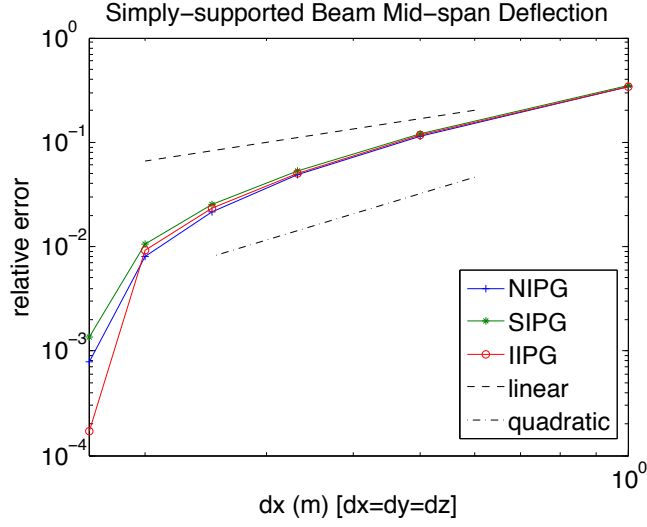


Figure 7: Convergence of three-dimensional DG formulation vs. discretization for simply-supported beam deflection

only plate model following Mindlin-Reissner plate theory with the following definitions.

$$\{U\} = \{u_1 \ v_1 \ u_{1+n} \ v_{1+n} \ w_1 \ u_2 \ v_2 \ u_{2+n} \ v_{2+n} \ w_2 \ \dots \ u_n \ v_n \ u_{2n} \ v_{2n} \ w_n\}^T \quad (40)$$

where  $n$  is the number of nodes on the bottom of the plate, node  $i + n$  is taken to be above node  $i$  and transverse deflection of top and bottom are taken to be equal, or  $w_i = w_{i+n}$ , eliminating the need for  $w_{i>n}$ .

$$\{\epsilon_b\} = \{\epsilon_x \ \epsilon_y \ \gamma_{xy}\}^T = [B_b]\{U\} \quad (41)$$

$$\{\sigma_b\} = \{\sigma_x \ \sigma_y \ \tau_{xy}\}^T = [D_b]\{\epsilon_b\} \quad (42)$$

$$\{\epsilon_s\} = \{\gamma_{yz} \ \gamma_{xz}\}^T = [B_s]\{U\} \quad (43)$$

$$\{\sigma_s\} = \{\tau_{yz} \ \tau_{xz}\}^T = [D_s]\{\epsilon_s\} \quad (44)$$

where the subscripts  $b$  and  $s$  indicate bending and shear, respectively. The volume integral that is used as the stiffness matrix then takes the form

$$[K] = \int_{\Omega^e} [B_b]^T [D_b] [B_b] d\Omega + \int_{\Omega^e} [B_s]^T [D_s] [B_s] d\Omega \quad (45)$$

$$[B_b] = [[B_{b1}] \quad [B_{b2}] \quad [B_{b3}] \quad [B_{b4}]] \quad (46)$$

$$[B_{bi}] = \begin{bmatrix} H_1 \frac{\partial N_i}{\partial x} & 0 & H_2 \frac{\partial N_i}{\partial x} & 0 & 0 \\ 0 & H_1 \frac{\partial N_i}{\partial y} & 0 & H_2 \frac{\partial N_i}{\partial y} & 0 \\ H_1 \frac{\partial N_i}{\partial y} & H_1 \frac{\partial N_i}{\partial x} & H_2 \frac{\partial N_i}{\partial y} & H_2 \frac{\partial N_i}{\partial x} & 0 \end{bmatrix} \quad (47)$$

$$[B_s] = [[B_{s1}] \quad [B_{s2}] \quad [B_{s3}] \quad [B_{s4}]] \quad (48)$$

$$[B_{si}] = \begin{bmatrix} N_i \frac{\partial H_1}{\partial z} & 0 & N_i \frac{\partial H_2}{\partial z} & 0 & \frac{\partial N_i}{\partial x} \\ 0 & N_i \frac{\partial H_1}{\partial z} & 0 & N_i \frac{\partial H_2}{\partial z} & \frac{\partial N_i}{\partial x} \end{bmatrix}. \quad (49)$$

In the bending and shear strain matrices,  $[B_b]$  and  $[B_s]$ ,  $H_i(x, y)$  are the two dimensional nodal interpolation functions in the planar directions and  $N_i(z)$  are the one dimensional transverse nodal interpolation functions. The shear term must be under-integrated numerically to prevent shear locking for thin elements. Further discussion of the numerical integration schemes used can be found in Appendix B. An approach used in other DG formulations of the plate bending problem is to use a lower order interpolant for shear terms than that used for bending terms [15].

### *a. Validation*

A clamped square plate subject to a concentrated load applied at its center was used to validate the plate element model. The plate is .3048 m x .3048 m x .00635 m (12 in x 12 in x 1/4 in) and isotropic. Theoretical values were calculated according to Timoshenko [33]. All three methods demonstrate quadratic convergence when linear elements are used, as shown in Figure 8.

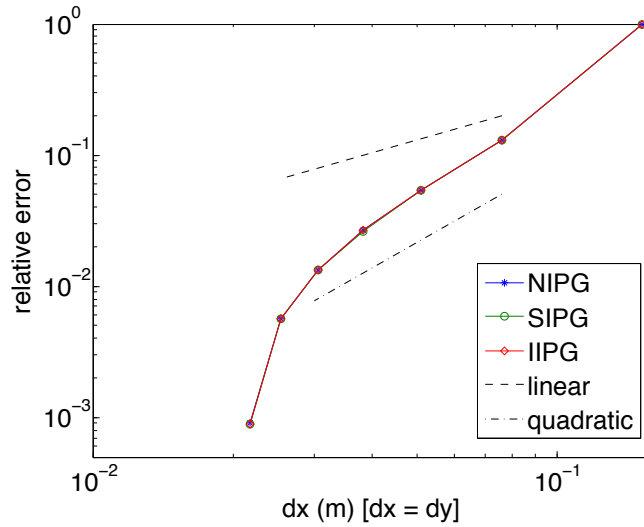


Figure 8: Convergence of center deflection of a clamped plate comprised of plate elements

A second validation was conducted by comparing dynamic continuous and discontinuous models of the same square plate. Both models consist of 144 square elements such that the characteristic length of each element is four times its thickness. Clamped boundary conditions and zero deflection and velocity initial conditions were applied and both models have lumped (diagonal) mass matrices. Figures 9 and 10 show excellent agreement between the two models for the transverse displacement and velocity of the center of the plate subjected to a constant concentrated force applied at its center. Appendix A details the time integration algorithms used.

One further validation compares the present formulation with central deflection of uniformly loaded composite plates as described by Lok and Cheng [34]. A square discretization with progressively more elements per side in plate and a single thickness element were modeled.

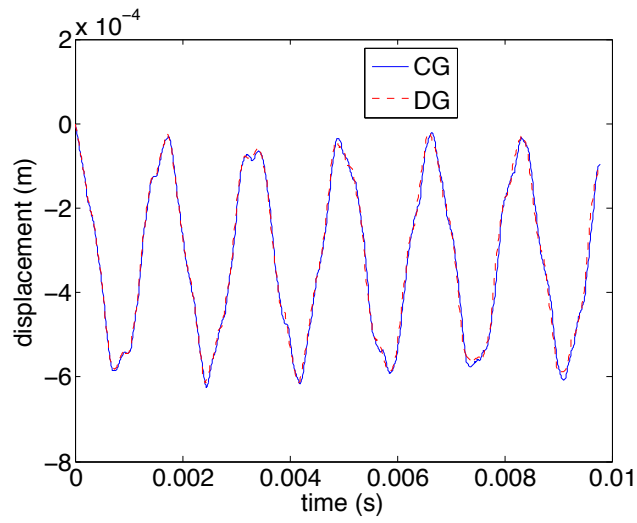


Figure 9: Comparison of displacement calculated for Continuous Galerkin and Discontinuous Galerkin models of a center loaded clamped plate

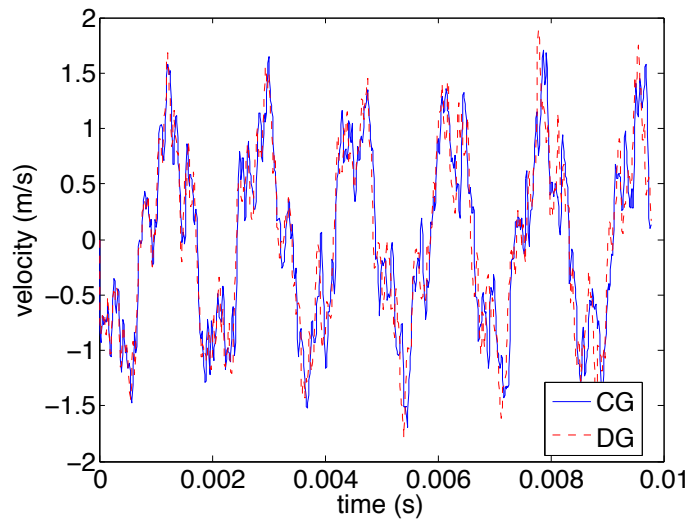


Figure 10: Comparison of velocity calculated for Continuous Galerkin and Discontinuous Galerkin models of a center loaded clamped plate

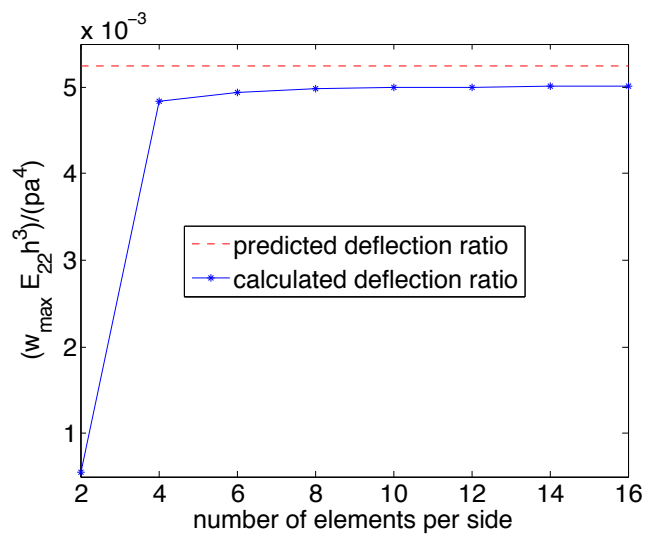


Figure 11: Convergence of central deflection of uniformly loaded clamped laminated plate, comparison with [34]

### 3. Stabilization and Penalty Parameters

One challenge in using these discontinuous Galerkin elements is selection of an appropriate penalty parameter for the last two terms of Equations (19) and (20). As  $\delta_p$  approaches infinity the methods return to their continuous roots, so selection of too large a penalty is a waste of computing resources. The penalty must also be large enough to guarantee existence and uniqueness of the solution [35]. Additionally, the nature of the penalty is often described as a function of the local element order or size with little other clarification. The nature of penalizing the jump as a stabilization mechanism is discussed by Brezzi et al. [9] for elliptic DG formulations in general. Others have computed lower bounds on penalties for various formulations, [36], [37], [38] among others.

In Liu's formulation [21], the penalty term is a surface integral multiplied by a parameter to be determined and the material shear modulus divided by the square root of the area over which the integral is calculated. Another intriguing approach is that of Ainsworth and Rankin [39] in which they compute a lower bound on the penalty parameter that is a function of the method selector ( $\theta_{DG}$  above) and the maximum eigenvalue of the elemental stiffness matrix; that value is also divided by a term analogous to the square root of the area of the integral. In view of this approach, the presence of the shear modulus in Liu's penalty term serves as a scaling factor to keep the penalty in the same numerical neighborhood as that of the volume integral,  $K_v$  or elemental stiffness matrix. Anticipating using this formulation for a composite material with potentially vastly different shear moduli between elements, we will combine these two approaches, replacing  $\delta_p G$  with  $\delta_p \cdot \max(\rho(K_v))$ . As long as  $\delta_p > (1 - \theta_{DG})^2$ , a unique solution will exist [39].

THIS PAGE INTENTIONALLY LEFT BLANK

### **III. COMPOSITE STRUCTURES**

Composite materials can provide designers with optimal combinations of strength, weight, flexibility, and other physical characteristics for their application. Effective design, however, requires a thorough understanding of material behavior in the expected operating environment—data which can be cumbersome to obtain, making the development of effective simulations key.

The strength of a chain is determined by that of its weakest link, but the utility of composite materials is the improvement each constituent element brings to the desired material properties of the whole. Like alloys, particulate composites generally demonstrate better properties than the homogeneous matrix material by virtue of the reinforcement provided by specifically chosen additives.

#### **A. MULTI-SCALE MODEL**

Analysis of structures consisting of composite materials, and of the materials themselves, require multiple scales of analysis to be used in conjunction with each other. That is, the analysis can proceed from the micro- (atomic or molecular) level to the meso- (material) level and on to the macro- (structural) level and back down again as necessary with smearing or decomposition of properties and loads as dictated by the analysis required. The properties of a laminated fibrous composite, for example, are a function of the properties of both fiber and matrix as well as the weave pattern of individual laminae and lay-up pattern of the assembled laminate. Similarly, failure of the same laminate can result from separation between laminae, separation of fibers from matrix, or failure of individual fibers. An illustration of this process is shown in Figure 12. Kwon [40] presents an extensive discussion of these cycles.

This study's focus on structural responses of existing composites allows the acceptance of micro-level analysis already conducted in the design and construction of the

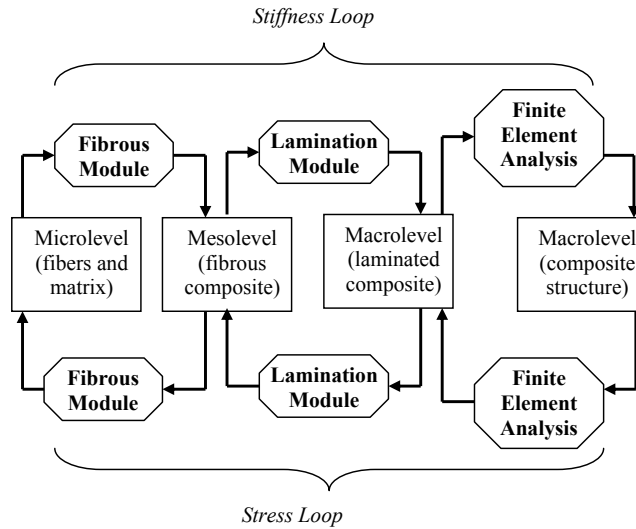


Figure 12: Multi-scale analysis cycle for a fibrous composite. From [40]

composite materials that will be assembled to create the sandwich plates of interest. That is, we will not deal with the properties of the fibers that are woven into E-glass, but will instead treat the manufacturer’s given orthotropic properties of a ply as known. Specific material properties used are listed in Appendix B.

## B. SANDWICH COMPOSITES

This work will attempt to model sandwich composites for plate and shell applications. These materials are comprised of low density cores that are relatively stiff transversely and skin layers that provide in-plane strength to the structure. Because the core material is used to provide transverse stiffness, it is tempting to model it using full three-dimensional solid finite elements; however, the aspect ratio of the plate structure and its included elements makes solutions generated using a plate element for all layers more accurate. That is, while the core is generally the thickest component in the sandwich, it is still thin relative to its planar cross-section, giving it a sub-optimal aspect ratio for solution with three-dimensional elements. This model of a composite material will consist of an as-

semblage of elements that are each homogeneously comprised of the constituent materials and of the type of element described. That is, the elemental models developed in Chapter II will be used with  $[D]$  matrices describing the material properties of constituent materials inserted appropriately. Care must be used to ensure the material property matrix contains not only the correct individual properties for each element, but also that it is of the correct form. Modeling an orthotropic material with a  $[D]$  matrix calculated in isotropic form may result in significant loss of accuracy. Figure 13 illustrates the two different transverse lay-ups used to model sandwich plates in this work; the three layer model includes only the core and two skin faces; the five layer or “with resin” model includes a relatively thin layer with material properties similar to common adhesives used in assembling sandwich composites. The two models vary slightly in thickness as well as in overall stiffness due to the inclusion of the extra layers.

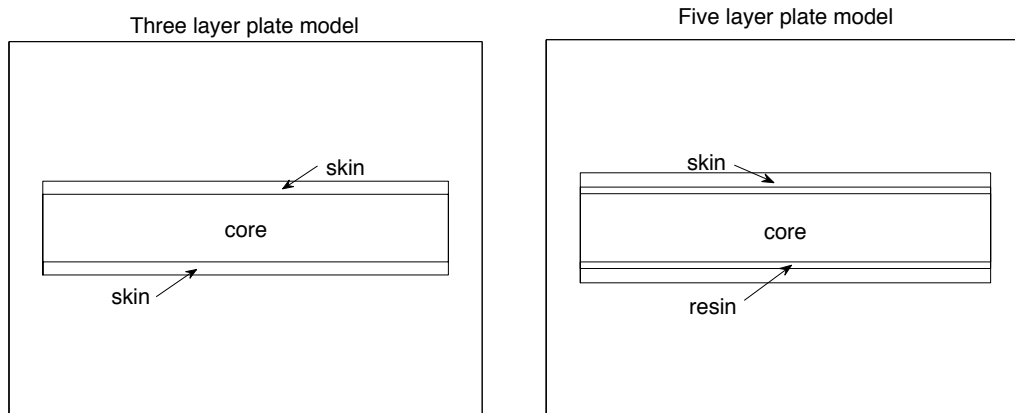


Figure 13: Three and Five Layer Sandwich Plate models

Schmit and Monforton [41] developed a discrete element method to predict the static deflection of sandwich plates and shells with laminated faces under a variety of boundary conditions. Kanematsu and Hirano [42] expanded on that work to examine both bending and vibration of sandwich plates; their work also included experimental validation. The deflection of a 50 inch square clamped plate with a one inch thick core of aluminum

honeycomb faced by two 0.015in thick aluminum skins under uniform pressure was calculated by both papers and is used here to validate the DG structural model developed in the previous chapter. Using one thickness element for each face and one for the core, maximum static deflection was calculated for a range of square planar discretizations; they are plotted in Figure 14. Good agreement was reached with as few as four elements in each direction, and refinement further than twelve elements in each direction was shown to be unnecessary. Both sets of authors neglected in-plane bending of the core material, which the present formulation does not, therefore the current model is stiffer and returns a slightly lesser static deflection.

Relative convergence of both maximum deflection and maximum bending stress in a clamped, square, five-layer sandwich plate subject to a concentrated center force was examined by modeling a quarter of the plate, taking advantage of symmetry to achieve finer discretizations without incurring excessive computational cost. For this study, a range of twelve to thirty elements per side of the quarter-plate was modeled. Deflection is the primary variable and bending stresses are post-processed quantities. Both skin and core stresses were calculated, but as there was minimal difference between the two, core stresses are omitted from the plot for clarity. Convergence was calculated relative to the finest discretization calculated, thirty elements per quarter-plate side ( $dx=0.0075$  m) and is shown in Figure 15. Both quantities converge at better than quadratic rates, the predicted rate for linear elements.

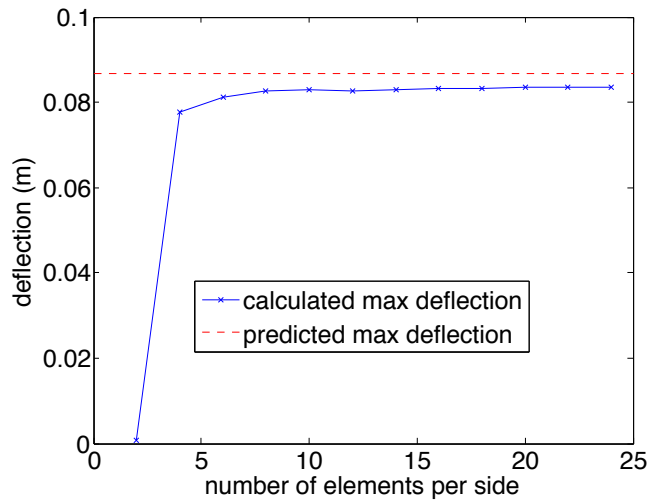


Figure 14: Convergence of DG Sandwich Plate max deflection (due to uniform load) to predicted, comparison with [41, 42]

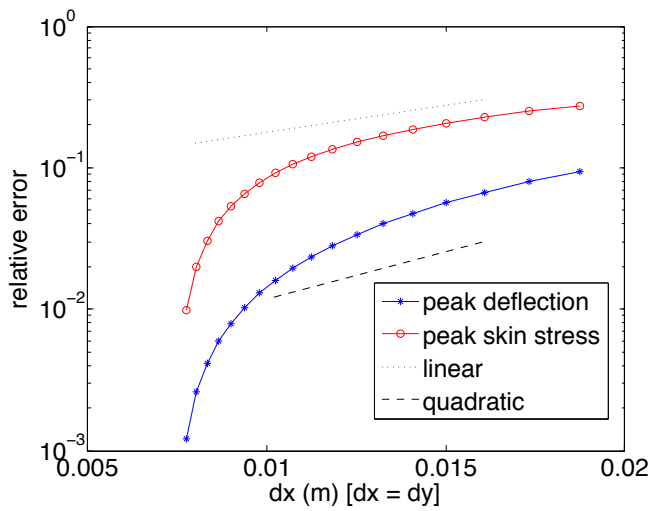


Figure 15: Relative convergence of DG Sandwich Plate max deflection and skin stress (due to concentrated load)

### C. FAILURE MODES AND IDENTIFICATION

Failure of sandwich structures is a function of the constituent materials, the geometry of the structure, and the nature of the loading. Common failure modes of such structures include debonding, delamination, core crushing, skin wrinkling, and general buckling. Debonding is the separation of the skin material from the core and delamination usually refers to the separation of layers within the skin material. In this work, debonding will be the primary failure mode examined. No attempt is made here to develop failure criteria; we will instead attempt to develop an appropriate method to reflect failure within a structural model.

Previous work [43] concluded that modeling an independent layer representing the adhesive between laminae of composites was necessary to observe the delamination failure mode. In this work we will examine whether such a layer can be omitted when Discontinuous Galerkin (DG) techniques are applied in assembling the structure.

One-quarter of a twenty-four by twenty-four element square clamped plate with the same aluminum skins and honeycomb core as was used in the previous section was the basis for this examination. This plate model is 450 mm x 450 mm, the core is 10 mm thick, each skin is 0.375 mm thick, and the load is a concentrated force of 1000 N applied to the center of the plate. The model was assembled as described in Chapter II and the global displacement vector was calculated. The degrees of freedom of interest, those on the interface between the bottom of the core and the top of the lower skin, were extracted and post-processed to calculate the bending stress vector at each point on that interface. In order to display the calculated data, an interpolation function describing resulting stress values of interest,  $\sigma_x$ , was generated using MATLAB's `TriScatteredInterp` function and then applied over a grid of the same dimension as the original discretization and plotted using `contourf`.

Figures 16 and 17 show the resulting normal stress in the  $x$  direction on the top of the lower skin (the side facing the core) and on the bottom of the core (the side facing the lower skin) for a three layer model. The upper right-hand corner of these quarter-plate

plots corresponds to the center of the whole plate and is the point of application of the concentrated load. As expected, the peak stress values for both components are located at the center of the plate, and the stiffer skin is taking a significantly larger portion of this in-plane load. The effects of the clamped boundary conditions can also be seen at the edges of both graphs. This process was repeated for a five-layer model with a lay-up of: skin-resin-core-resin-skin. In this case the resultant stresses were calculated for the top of the lower skin and bottom of the core as before as well as both the top and bottom of the intervening resin layer. The results are displayed in Figures 18 – 21. The stresses on the two faces of the resin layer are close enough in magnitude to treat them as equal. Additionally, the stresses on the skin and core are negligibly affected by the insertion of the resin layer into the model. Unfortunately, the relative magnitudes of the stresses do not suggest an intuitive or convenient stress-based failure criteria that could be applied to the resin in absentia based on the calculated values on the faces of the skin and core. Therefore, the inclusion of an interface layer is needed to accurately model debonding of skin faces from cores of sandwich composites.

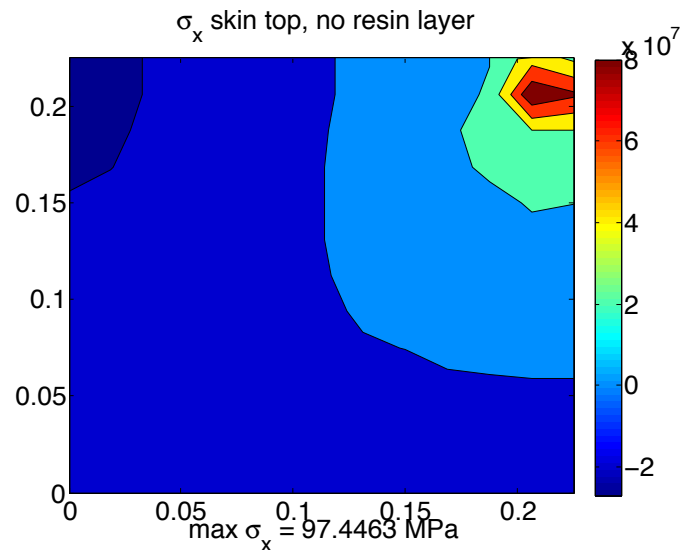


Figure 16: Planar stress on the skin of a clamped three-layer sandwich plate subject to concentrated center force

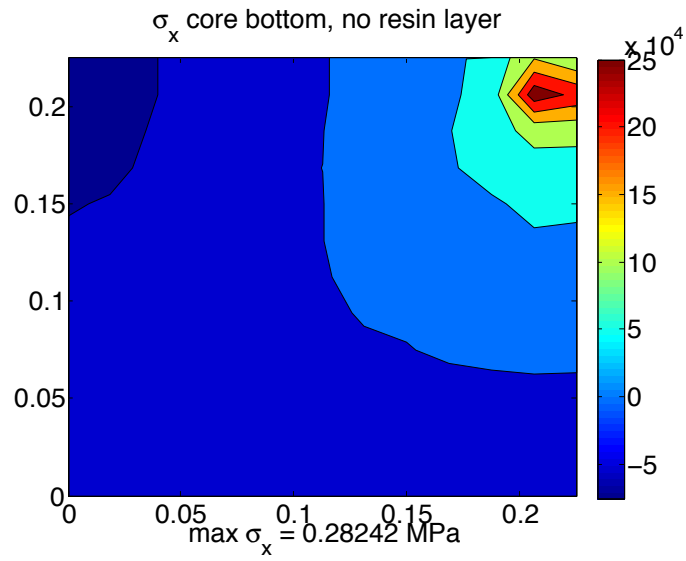


Figure 17: Planar stress on the core of a clamped three-layer sandwich plate subject to concentrated center force

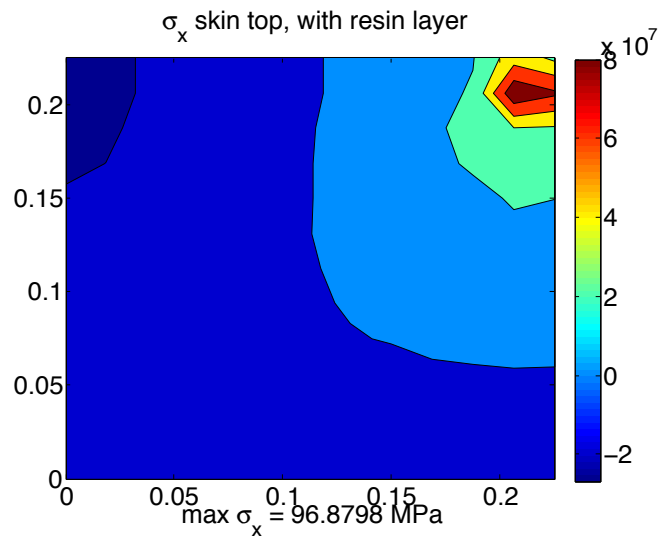


Figure 18: Planar stress on the skin of a clamped five-layer sandwich plate subject to concentrated center force

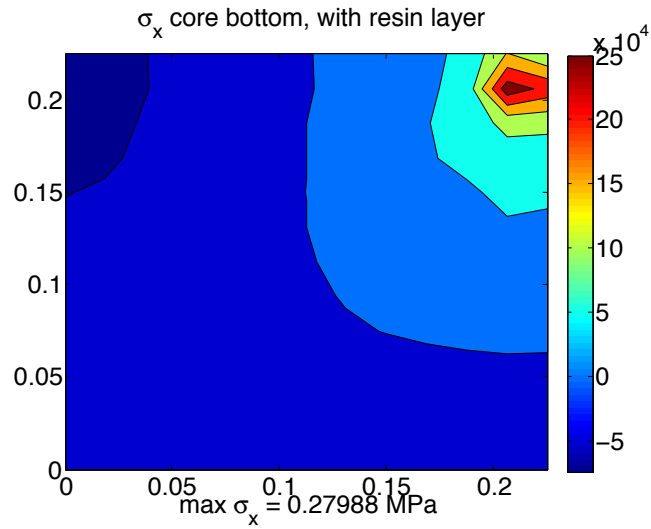


Figure 19: Planar stress on the core of a clamped five-layer sandwich plate subject to concentrated center force

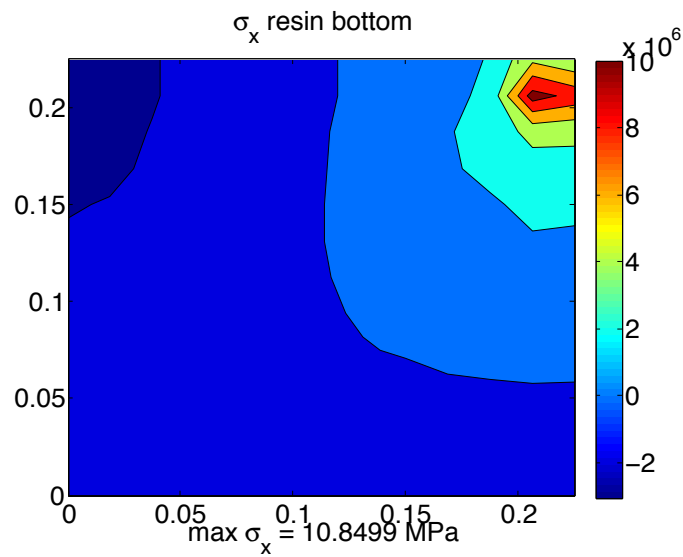


Figure 20: Planar stress on the bottom of a resin layer of a clamped five-layer sandwich plate subject to concentrated center force

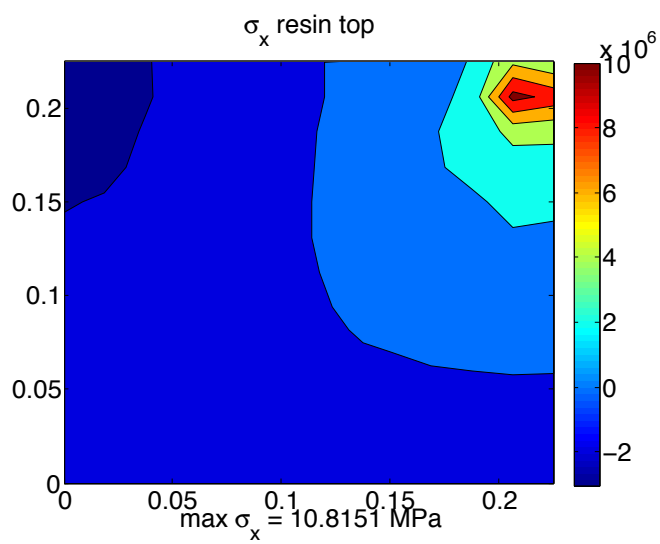


Figure 21: Planar stress on the top of a resin layer of a clamped five-layer sandwich plate subject to concentrated center force

## D. FAILURE MODELING

This section will compare and contrast three proposed methods of modeling debonding failure between the core and the resin layer opposite an imposed concentrated force at the center of a sandwich plate. Each of the methods to follow will be demonstrated using a five layer plate discretized into a twenty-four by twenty-four element mesh. The calculated planar stress values on the bottom of the core, the top and bottom of the lower resin layer and the top of the skin layers will be displayed and discussed. The undamaged model as displayed in Figures 18–21 will be used as a baseline reference case.

### 1. Damage via Complete Disconnection

Mergheim et al. [22] introduce a scheme that combines DG methods with existing interface methods for modeling failure. Specifically, they propose re-defining Equation (19) as follows:

$$\begin{aligned}
 a(u, v) = & \sum_{E \in \mathcal{X}} \int_E \sigma(u) : \varepsilon(v) dV - \sum_{\partial E \in (S_i + \Gamma_u)} (1 - \alpha) \int_{\partial E} \{\sigma(u)n^s\} \cdot [v] dS \\
 & + \sum_{\partial E \in (S_i + \Gamma_u)} \theta_{DG} (1 - \alpha) \int_{\partial E} \{\sigma(v)n^s\} \cdot [u] dS \\
 & + \sum_{\partial E \in (S_i + \Gamma_u)} \int_{\partial E} [v] \cdot \left( (1 - \alpha) \frac{\delta_p G}{|s|} [u] + \alpha \mathbf{t}[u] \right) dS. \quad (50)
 \end{aligned}$$

where  $\alpha$  is a switching factor and  $\mathbf{t}$  is a traction vector governed by a traction-separation law. In the pre-critical or undamaged regime,  $\alpha = 0$  and Equation (50) is identical to Equation (19); in the post-critical or damaged regime,  $\alpha = 1$  and the surface integrals representing connected interfaces are replaced by a traction-separation law that models progressive failure.

Adapting this concept and assuming complete failure of the interface between the core and resin, debonding damage was simulated by separating a four by four array of resin elements surrounding the center of the plate from their core element neighbors. In

the present formulation, all of the area integrals of Equation (19) are calculated for both interior and Dirichlet exterior boundaries. If the interface between two elements is deemed to have failed, those faces can then be considered members of  $\Gamma_u$  rather than  $S_i$ , so the  $K_{LL}^i$  and  $K_{RR}^i$  terms remain and the various left and right components ( $K_{LR}^i$  and  $K_{RL}^i$ ) are simply deleted from the global  $K$  matrix.

All other parameters were unchanged from the undamaged case. The resulting stress fields are displayed in Figures 22 – 25. The skin stresses are largely unchanged from the undamaged state. The core, however, bears the brunt of this simulated debonding; its maximum stress value is twenty times that of its undamaged version. This is because this simulation has effectively removed all constraints on/supports to the core in the area of greatest load. In the undamaged model, the static deflection at the center of the plate is consistent through the thickness; that is, the transverse displacement at all center nodes, in both skin layers, both resin layers, and the core, has been the same. In this example, the static deflection is consistent from the top of the structure (point of load application) down to the bottom of the core; the deflection of the lower resin and lower skin layers was consistent within those two layers, but markedly less than that above. Deflection curves along the centerline of the plate for the bottoms of the core, resin, and lower skin layers are shown in Figure 26. This is because this method of debonding the plate has also eliminated any means of transferring the load between those layers within the damage zone. Complete disconnection of inter-elemental interfaces is not the proper way to model this sort of damage. A more consistent approach may be to disconnect the planar dofs between elements, but leave the transverse dofs connected.

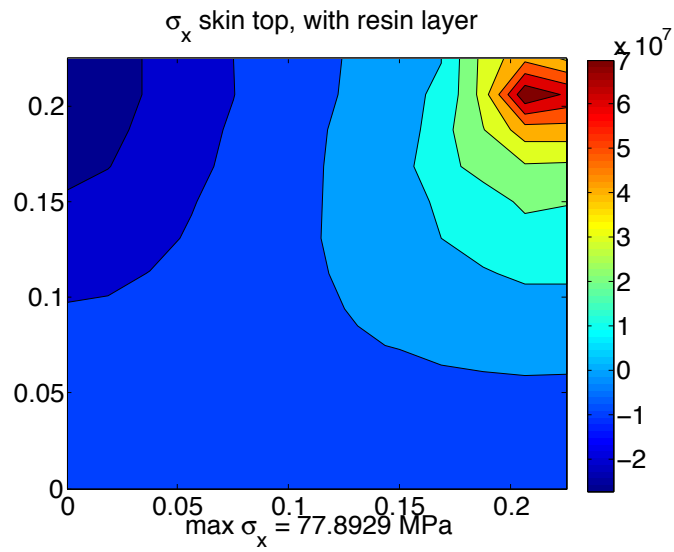


Figure 22: Planar stress on the skin of a damaged via complete disconnection clamped five-layer sandwich plate subject to concentrated center force

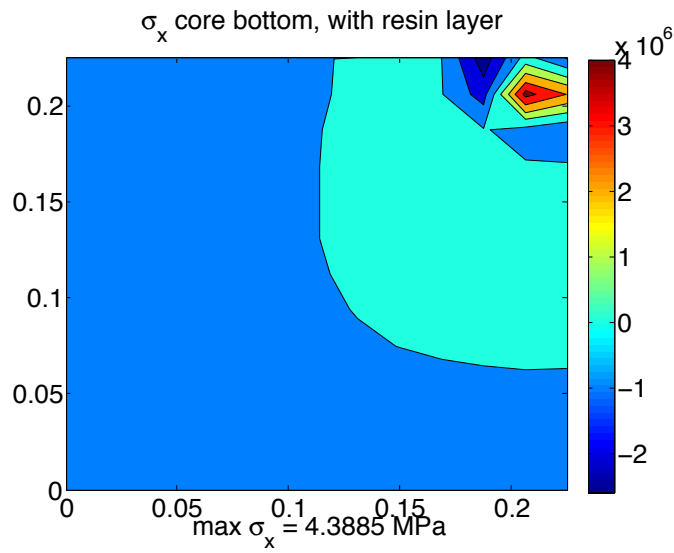


Figure 23: Planar stress on the core of a damaged (via complete disconnection) clamped five-layer sandwich plate subject to concentrated center force

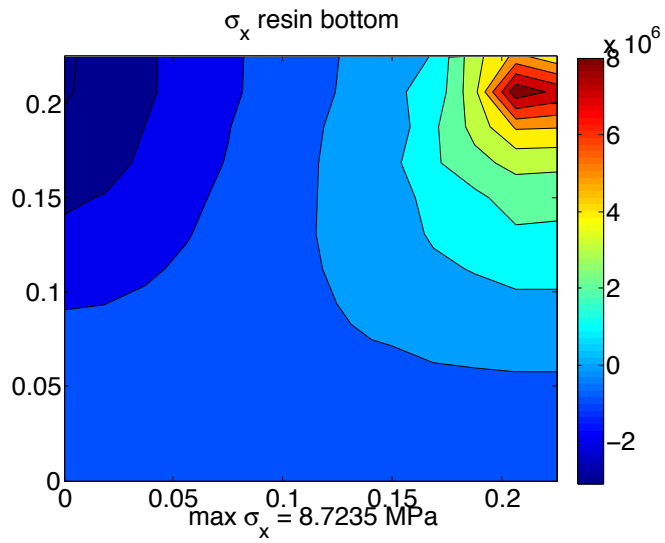


Figure 24: Planar stress on the bottom of the resin layer of a damaged (via complete disconnection) clamped five-layer sandwich plate subject to concentrated center force

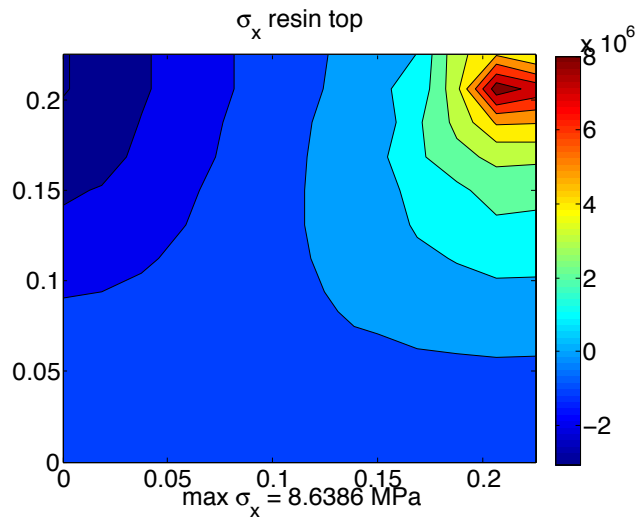


Figure 25: Planar stress on the top of the resin layer of a damaged (via complete disconnection) clamped five-layer sandwich plate subject to concentrated center force

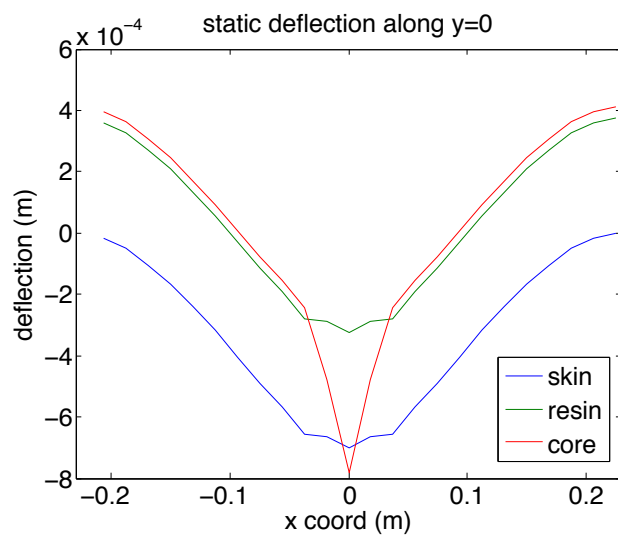


Figure 26: Static deflection along centerline of damaged (via complete disconnection) clamped five-layer sandwich plate subject to concentrated center force

## 2. Damage via Partial Disconnection

To implement a more physically consistent disconnection between core and resin elements in the debonding zone, only those rows and columns of the interface sub-matrices that correspond to the planar ( $u_i$  and  $v_i$ ) dofs will be removed. That is, the entries in those sub-matrices that correspond to the transverse ( $w_i$ ) dofs will be left in place. Once again, this removal of entries from the global stiffness matrix is executed after its assembly – a step that can be repeated as necessary for progressive failure with relative simplicity. The resultant stresses can be seen in Figures 27 – 30. The maximum stress values are consistently lower than the undamaged case in all three materials, but more noteworthy is the movement of the location of maximum stress from the center of the domain, directly below the imposed load, to the edge of the debonding zone. This behavior appears to be consistent with a physical stress concentration on the edge of a discontinuity in a structure and may be useful in modeling damage propagation. Figure 31 shows that the static deflection corresponding to this failure model is physically consistent: the core does not deflect beyond or through the resin and skin layers below it, but all three layers show sharper deflection within the debonding zone than in the rest of the domain.

Figures 32 – 34 show the stress profile generated using this partial disconnection method with the quarter-plate model and a discretization of thirty elements per side. The stress concentration effect observed in the relatively coarse meshes of Figures 27 – 30 are clearly present in the finer model as well.

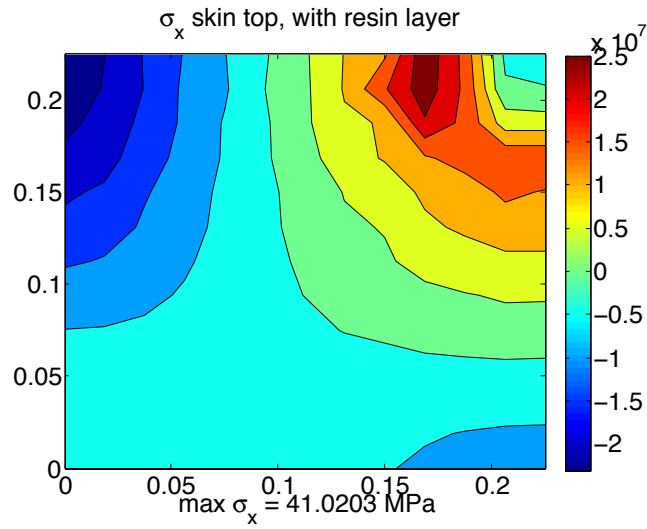


Figure 27: Planar stress on the skin of a damaged (by partial disconnection clamped) five-layer sandwich plate subject to concentrated center force

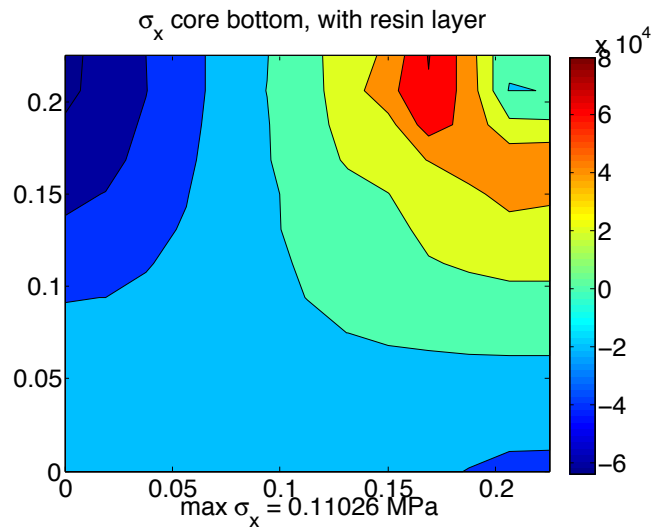


Figure 28: Planar stress on the core of a damaged (by partial disconnection clamped) five-layer sandwich plate subject to concentrated center force

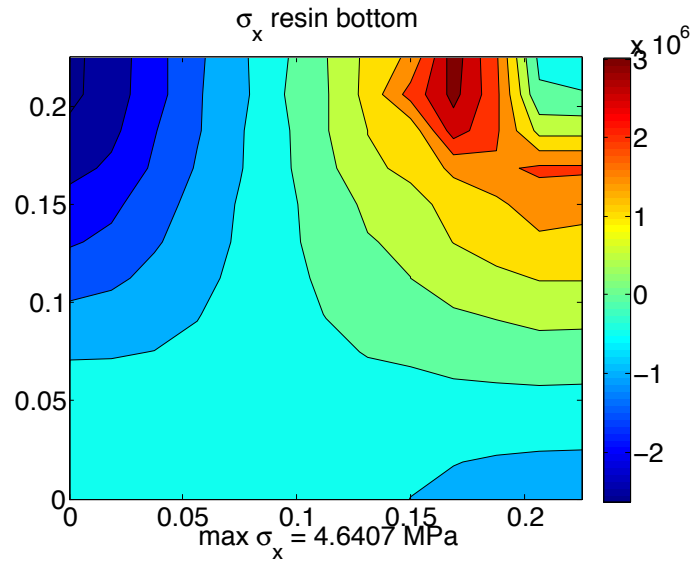


Figure 29: Planar stress on the bottom of the resin layer of a damaged (by partial disconnection) clamped five-layer sandwich plate subject to concentrated center force

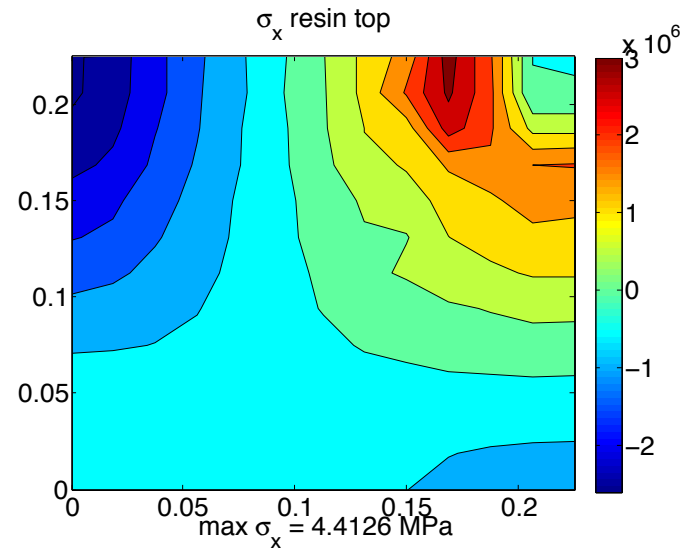


Figure 30: Planar stress on the top of the resin layer of a damaged (by partial disconnection) clamped five-layer sandwich plate subject to concentrated center force

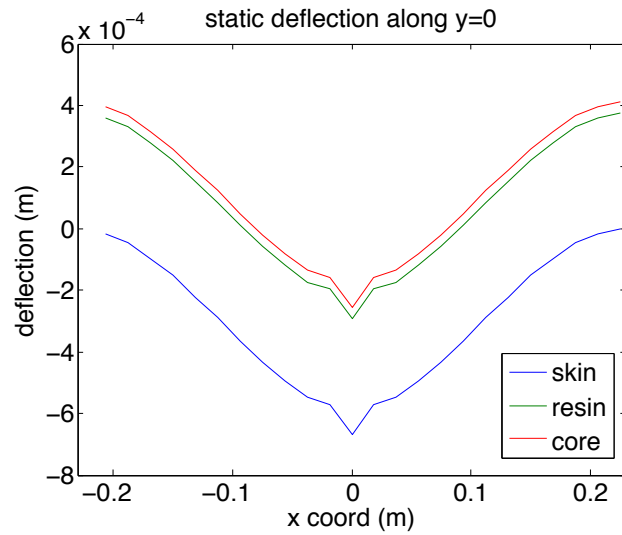


Figure 31: Static deflection along centerline of damaged (via partial disconnection) five-layer sandwich plate subject to concentrated center force

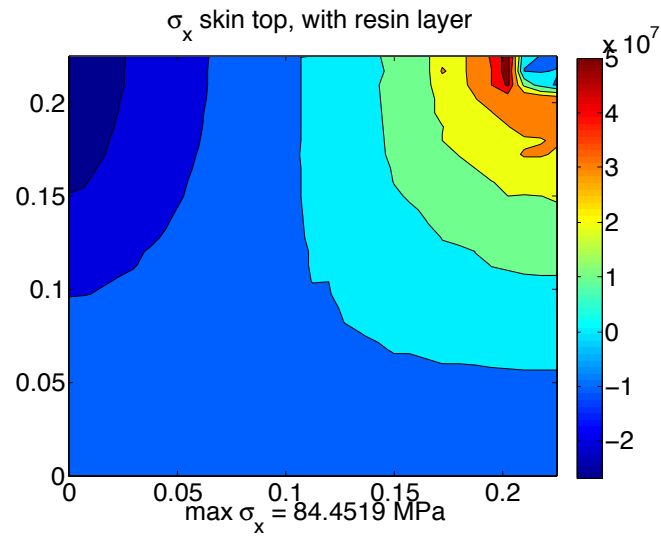


Figure 32: Planar stress on the skin of a damaged (by partial disconnection) clamped five-layer sandwich plate subject to concentrated center force, fine view

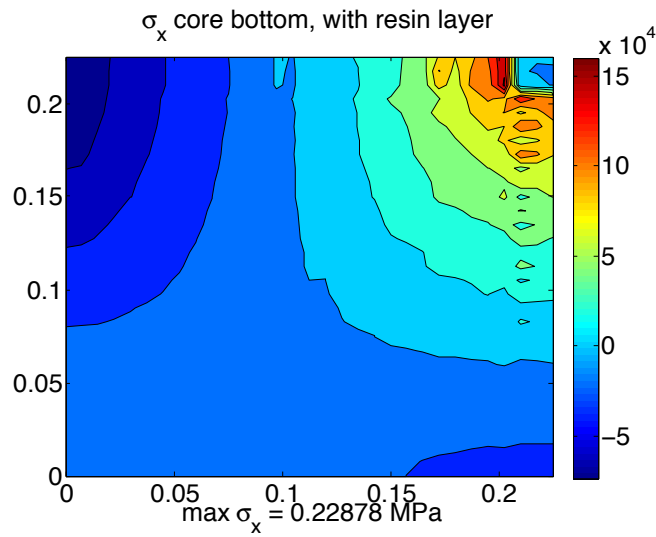


Figure 33: Planar stress on the core of a damaged (by partial disconnection) clamped five-layer sandwich plate subject to concentrated center force, fine view

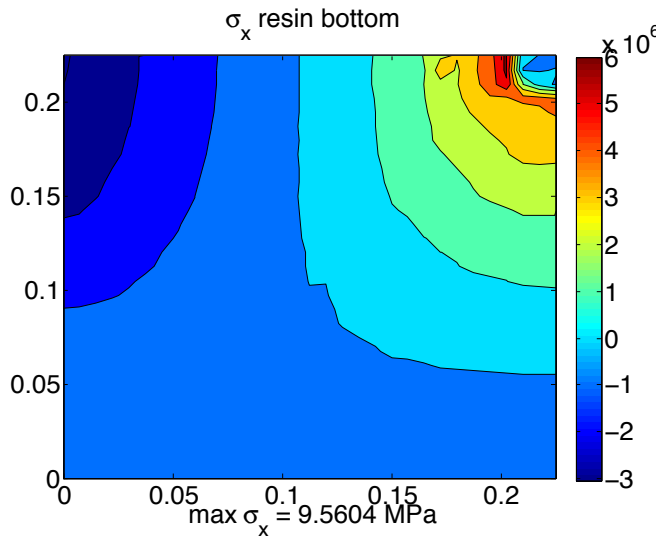


Figure 34: Planar stress in the resin layer of a damaged (by partial disconnection) clamped five-layer sandwich plate subject to concentrated center force, fine view

### 3. Damage via Reduced Moduli

The next method of imposing damage in this model was to leave all elements connected as in the undamaged state, but to reduce the effectiveness of the resin elements in the damage zone. The same resin elements identified in the previous attempt remained connected to their core counterparts, but their shear and elastic moduli were reduced to 1% of the values used for the rest of the layer—an arbitrarily chosen reduction. The resultant stresses are plotted in Figures 35 – 38. In this model, the stress in the core elements is comparable to that of the undamaged plate and the dramatically lower stress values in the center of the resin layer is entirely attributable to the lower modulus. This method would seem to be similar to Mergheim’s insertion of a traction-separation law to describe the progression from damage initiation to complete separation [22].

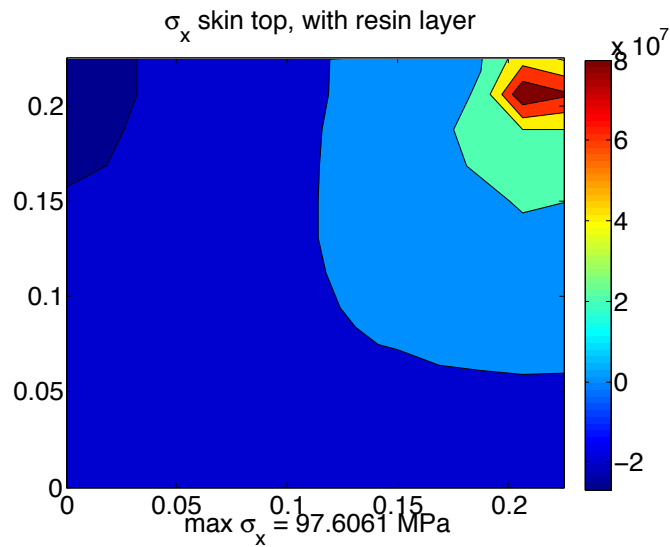


Figure 35: Planar stress on the skin of a damaged (by reduced modulus) clamped five-layer sandwich plate subject to concentrated center force

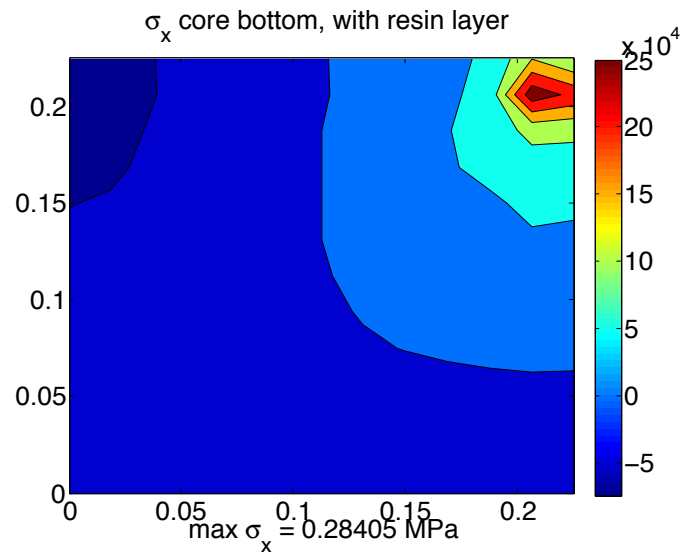


Figure 36: Planar stress on the core of a damaged (by reduced modulus) clamped five-layer sandwich plate subject to concentrated center force

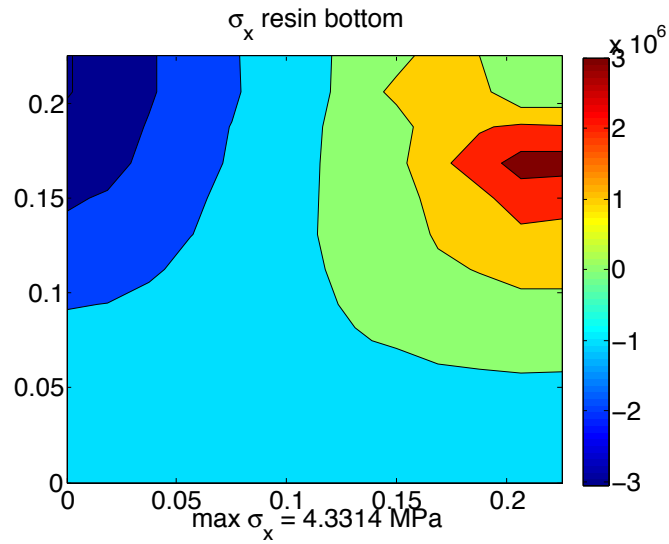


Figure 37: Planar stress on the bottom of the resin layer of a damaged (by reduced modulus) clamped five-layer sandwich plate subject to concentrated center force

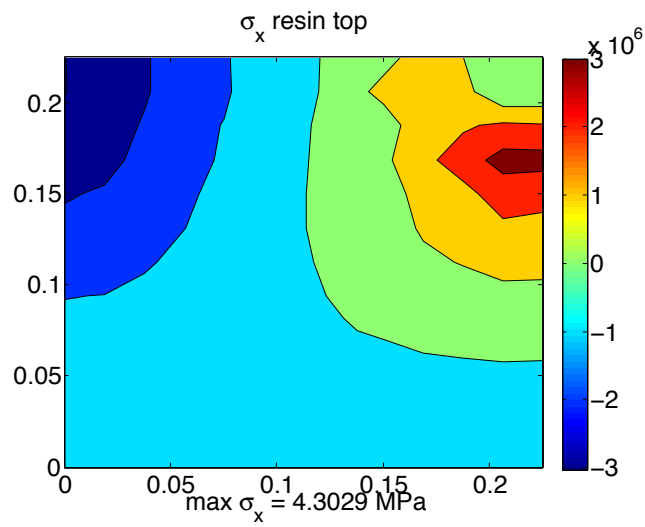


Figure 38: Planar stress on the top of the resin layer of a damaged (by reduced modulus) clamped five-layer sandwich plate subject to concentrated center force

## E. SYNTHESIS

Table 1 contains a summary of the above results; the numerical stress values displayed are of use only in their relationship to each other. These were all calculated from the twelve by twelve element quarter-plate, which corresponds to the coarsest discretization used in the convergence calculations displayed in Figure 15.

Complete elimination of interface terms from the global stiffness matrix does not correctly model physical constraints on the core from remaining layers in the structure below the section deemed to have been delaminated. Disconnection of the planar terms whilst retaining transverse interface terms does appear to correctly model expected physical behavior. Adjusting the physical properties of the resin or interface layer remains a potential tool for faithful modeling of traction-separation laws.

	Undamaged		Complete Disconnect		Semi-Disconnect		Reduced Modulus	
	value	location	value	location	value	location	value	location
skin	96.88	center	77.89	center	41.02	zone edge	97.61	center
core	0.280	center	4.389	center	0.111	zone edge	0.284	center
resin top	10.82	center	8.639	center	4.413	zone edge	4.331	zone edge
resin bottom	10.85	center	8.724	center	4.641	zone edge	4.303	zone edge

Table 1: Comparison of maximum planar stress values (in MPa) and locations for damaged and undamaged clamped sandwich plates subject to a concentrated center force

## IV. FLUID MODEL

Following the work of Olson and Bathe [23], Fluid-Structure Interaction (FSI) will be analyzed via a velocity potential in the fluid. The transverse plate velocity will be matched to the  $z$  component of the fluid velocity as a compatibility condition between the two domains. The scalar velocity potential follows the wave equation, so a sufficiently accurate and efficient model of that equation with appropriate boundary conditions is required for the fluid portion of this work.

A great many methods are available to model the fluid mechanics necessary for this work, but as our primary interest is in the structural side of the fluid-structure interaction, achieving adequate accuracy without incurring significant computational cost lead to the exploration of CA methods.

### A. VELOCITY POTENTIAL AND WAVE EQUATION THEORY

The velocity potential,  $\phi$ , in the fluid domain is defined as

$$\vec{v} = \nabla\phi \quad (51)$$

where  $\vec{v}$  is the velocity of the fluid. The wave equation is

$$\ddot{u} = c^2\nabla^2u \quad (52)$$

where  $c$  is the acoustic speed of the (fluid) medium. Coupled with appropriate initial conditions, this well-posed initial value problem has been much studied and discussed [44]. In one-dimension, the problem

$$u_{tt} = c^2u_{xx} \quad -\infty < x < \infty \quad 0 < t < \infty \quad (53)$$

$$u(x, 0) = f(x)$$

$$u_t(x, 0) = g(x)$$

is satisfied by the D'Alembert solution

$$u(x, t) = \frac{1}{2}[f(x - ct) + f(x + ct)] + \frac{1}{2c} \int_{x-ct}^{x+ct} g(\xi) d\xi. \quad (54)$$

The three-dimensional extensions are

$$u_{tt} = c^2 \nabla^2 u \quad (x, y, z) \in R^3 \quad (55)$$

$$u(x, y, z, 0) = \varphi(x, y, z)$$

$$u_t(x, y, z, 0) = \psi(x, y, z)$$

which is satisfied by

$$u(x, y, z, t) = t\bar{\psi} + \frac{\partial}{\partial t}[t\bar{\varphi}] \quad (56)$$

where  $\bar{\psi}$  and  $\bar{\varphi}$  are the averages of their respective initial conditions over the sphere of radius  $ct$  centered at  $(x, y, z)$ ; specifically,

$$\bar{\psi}(x, y, z) = \frac{1}{4\pi c^2 t^2} \int_0^\pi \int_0^{2\pi} \psi(x + ct \sin \phi \cos \theta, y + ct \sin \phi \sin \theta, z + ct \cos \phi) (ct)^2 \sin \phi d\theta d\phi \quad (57)$$

and

$$\bar{\varphi}(x, y, z) = \frac{1}{4\pi c^2 t^2} \int_0^\pi \int_0^{2\pi} \varphi(x + ct \sin \phi \cos \theta, y + ct \sin \phi \sin \theta, z + ct \cos \phi) (ct)^2 \sin \phi d\theta d\phi. \quad (58)$$

The integrals in (57) and (58) are rarely simple to evaluate analytically.

## B. FINITE ELEMENT MODEL OF THE WAVE EQUATION

Beginning with the wave equation as applied to the velocity potential,

$$c^2 \nabla^2 \phi = \frac{\partial^2 \phi}{\partial t^2} = \ddot{\phi} \quad (59)$$

multiply all terms by a test function,  $w$ , and integrate over the domain to get

$$\int_{\Omega} w \ddot{\phi} d\Omega - c^2 \int_{\Omega} w \nabla^2 \phi d\Omega = 0 \quad (60)$$

integrate the second term by parts and apply Green's Identity to get

$$\int_{\Omega} w \ddot{\phi} d\Omega + c^2 \int_{\Omega} \nabla w \cdot \nabla \phi d\Omega = c^2 \int_{\Gamma} w \nabla \phi \cdot \hat{n} d\Gamma \quad (61)$$

recall the definition of the velocity potential to transform the right-hand side,

$$\int_{\Omega} w \ddot{\phi} d\Omega + c^2 \int_{\Omega} \nabla w \nabla \phi d\Omega = c^2 \int_{\Gamma} w \vec{v} \cdot \hat{n} d\Gamma. \quad (62)$$

Choosing Galerkin test functions, the derivatives of the trial functions with respect to the unknowns, the two volume integrals become

$$[M_f] = \int_{\Omega} \{H\}^T \{H\} d\Omega \quad (63)$$

$$[K_f] = \int_{\Omega} \{\nabla H\}^T \{\nabla H\} d\Omega \quad (64)$$

where  $\{H\}$  is the vector of nodal interpolation functions. In the usual Finite Element (FE) matrix-vector form we get

$$[M_f] \{\ddot{\phi}\} + c^2 [K_f] \{\phi\} = c^2 \int_{\Gamma} w \vec{v} \cdot \hat{n} d\Gamma. \quad (65)$$

Equations (62) and (65) hold for each element of a finite element domain, and, if continuity between elements is enforced, also hold globally. Thus the right-hand side is only defined on the boundary of the domain. At the fluid-structure interface the velocity compatibility provides a convenient input to this finite element problem. Specified Dirichlet or Neumann boundary conditions can also be applied with relative simplicity, but for this work non-reflecting boundary conditions are most appropriate yet are not easily applied.

### C. CELLULAR AUTOMATA MODEL OF THE WAVE EQUATION

Cellular Automata (CA) are discrete, rule-based numerical methods that can model complex physical phenomena with relative simplicity. Generally, both space and time are treated discretely and the value of the quantity in question is limited to a finite set of values. As the space-time domain proceeds or grows the seemingly simple model converges to the complex real-world behavior. The simplicity of the chosen rules and their implementation lowers the computational cost while still achieving required accuracy. CA rules developed for modeling wave propagation are pre-cursors to the lattice Boltzmann method of modeling fluid flow.

Following the work of Chopard [25, 26], Kwon and Hosoglu [28] modeled the wave equation in one- and two-dimensions with fixed boundaries using the following rules:

$$\phi_C(t + \Delta t) = \phi_W(t) - \phi_C(t - \Delta t) + \phi_E(t) \quad (66)$$

$$\phi_C(t + \Delta t) = (\phi_W(t) + \phi_E(t) + \phi_S(t) + \phi_N(t) - 2\phi_C(t - \Delta t))/2. \quad (67)$$

The value of  $\phi$  at each interior grid point in the domain of interest ( $\phi_C$ ) is updated according to the values at its nearest Von Neumann neighbors ( $\phi_N, \phi_S, \phi_E, \phi_W$ ) as shown in Figure 39.

For convenience the set of points is divided into two sets, “black” and “white” (or “odd” and “even”), such that the neighbors of each white point are all black, and only one “color” is updated during each iteration. This model includes an evolution of the variable  $\phi$

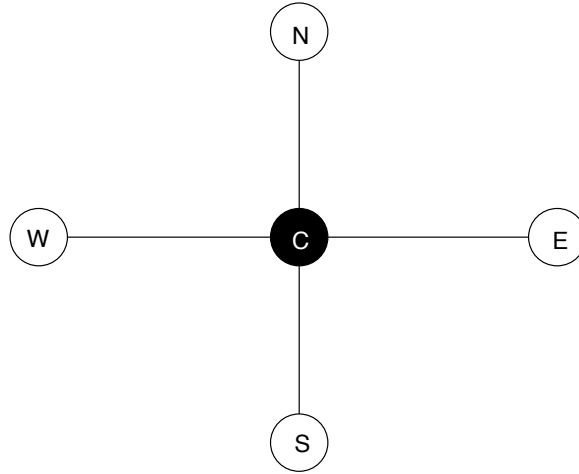


Figure 39: Center node (black) and its Von Neumann neighbors (white)

from being restricted to integer values (as in a traditional CA model) to being real valued. In its fully discrete form this CA rule was developed to model particle motion; with the relaxation that allows real-valued states, it also corresponds to the finite difference model of the wave equation on a uniform grid.

### 1. One Dimension

The classic illustration of D’Alembert’s solution to the one-dimensional wave equation is the perturbation of a string subject to tension. For the moment, we shall apply fixed boundary conditions to the ends of the “string” and focus our attention to interior points well away from those ends. Further discussion of appropriate boundary conditions will follow. Consider a string subject to a Gaussian perturbation at its midpoint as shown in Figure 40,

$$u_{tt} = c^2 u_{xx} \quad -\infty < x < \infty \quad 0 < t < \infty \quad (68)$$

$$u(x, 0) = f(x) = e^{-\frac{x^2}{2}}$$

$$u_t(x, 0) = g(x) = 0.$$

The D'Alembert solution to this problem is

$$u(x, t) = \frac{1}{2} \left[ e^{-\frac{(x-ct)^2}{2}} + e^{-\frac{(x+ct)^2}{2}} \right], \quad (69)$$

which agrees nicely with the CA solution computed using the rule found in Equation (66) as shown in Figure 41.

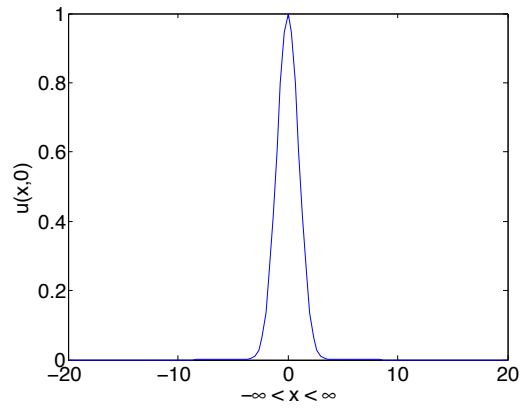


Figure 40: Initial perturbation of an infinite string

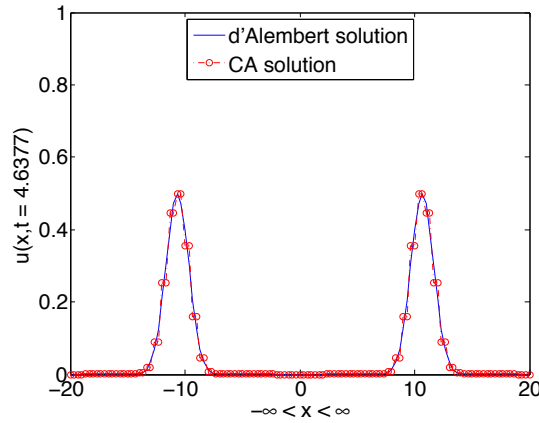


Figure 41: CA solution vs. D'Alembert's solution to the one-dimensional wave equation in an infinite string

## 2. Boundary Conditions

Fixed boundary conditions are easy to implement, but are of limited utility in modeling a potentially infinite fluid domain. One possible approach is to model a much larger domain than that of interest so that the area of interest is well away from the boundary and, as such, solutions within it are unpolluted by whatever boundary condition is imposed. This requires many computations that will be ignored—a seeming waste. Another approach is to generate a model of a non-reflecting boundary such that the wave in question is unaffected by its proximity. This is an active area of research in the finite element arena. In the CA arena, Chopard and Droz [25] suggested implementing boundary conditions by generating virtual cells adjacent to the boundary cells as shown in Figure 42. Fixed or specified boundary conditions do not require a virtual neighbor, but are shown for completeness. Non-reflecting (or zero-gradient or adiabatic) boundaries model the behavior in the heart of the domain of interest, well away from the influence of any boundary. The free boundary condition corresponds to that of a constant gradient. In practice, this can be implemented either by generating the virtual neighbor cells or by applying the resulting rule to the actual cells located on the boundary in question.

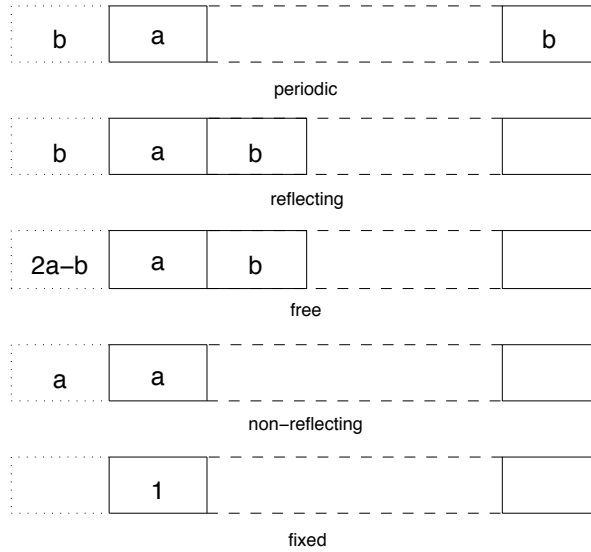


Figure 42: Virtual cell values for various boundary conditions in one dimension. After [25]

Figure 43 shows the application of several different boundary conditions to the positive side of the spatial domain of our one-dimensional wave equation. For reference the  $f(x - ct)$  portion of the D'Alembert solution is shown as an exact solution. The non-reflecting boundary condition corresponds quite well with the analytic. All four waves peak initially in unison; the reflecting wave (black) returns with equal amplitude while the free wave (red) returns with an inverse amplitude. The fluid domain to be modeled will have non-reflecting boundary conditions imposed at the arbitrary edge of the domain and a free boundary used to represent the air-water interface.

### 3. Discretization and Model Fidelity

The various waves modeled above by CA rules display a coarseness that results from updating the value of each point in space at alternating time steps. The initial perturbation displayed thus far has been a Gaussian wave of medium width that proved to be smooth enough to demonstrate the desired characteristics. Attempts to model a point source along the lines of  $f(x) = 0, x \neq 0, f(x) = 1, x = 0$  were unsuccessful, begging the question of how smooth a function or discretization are necessary to use CA to model the

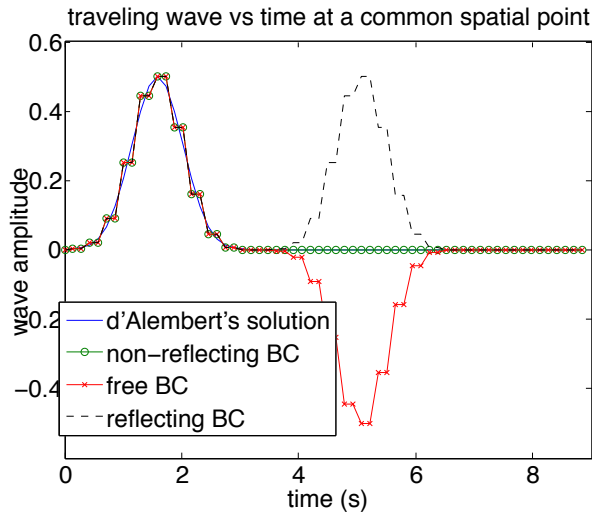


Figure 43: Application of various boundary conditions to CA calculation of one-dimensional wave propagation

wave equation. In order to determine a sufficiently fine discretization relative to the sharpness of the initial perturbation,  $f(x) = e^{-\frac{x^2}{2\sigma^2}}$ , a series of progressively narrower Gaussians as shown in Figure 44. For each initial condition, the CA solution to the wave equation was calculated for the same set of discretizations (progressively smaller  $dx$ ) and error norms relative to the D'Alembert solution were calculated at the same arbitrary time. Non-reflecting boundary conditions were applied in all cases. The resultant convergence as a function of  $dx$  is shown in Figure 45. An error norm of 1% was chosen as the comparison point. The largest  $dx$  value required to achieve that level of convergence was then plotted against the width at half maximum for each initial condition as shown in Figure 46. A linear estimate of that data is that  $dx_c = \frac{2}{3}\sigma$ . Applying this estimate to the specific  $f(x)$  used, 4.5 elements or nodes are required to represent the descent from peak value of  $f$  to 1% of that peak. Therefore, a discretization that uses eleven or more nodes to represent both sides of a peak should be sufficient.

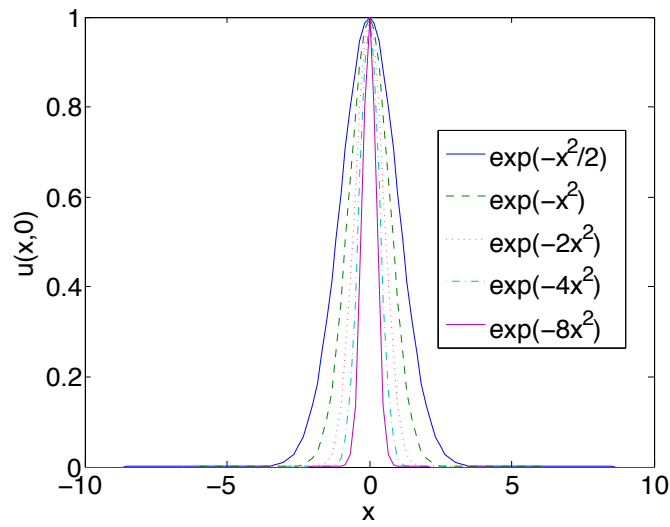


Figure 44: Initial perturbations of varying widths

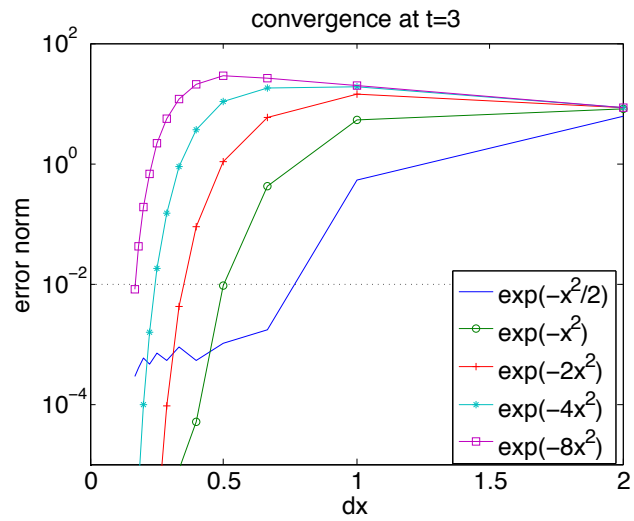


Figure 45: CA solution to 1d wave equation convergence as a function of  $dx$  for various initial conditions

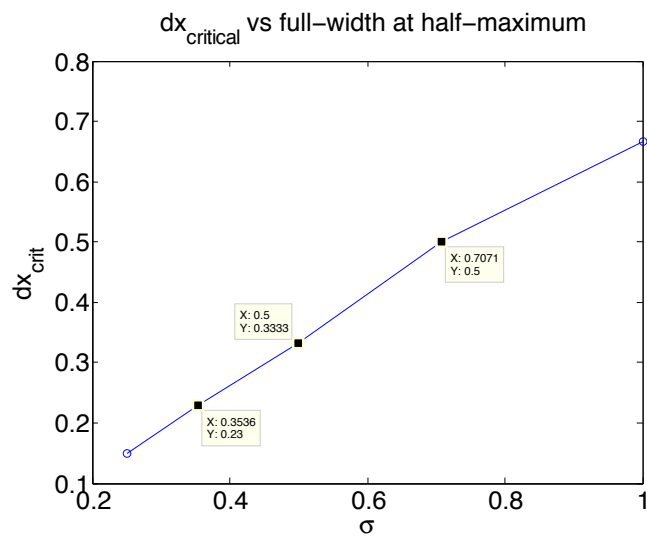


Figure 46: Critical discretization vs. initial perturbation width

#### 4. Convergence

To examine convergence of the present CA rule for wave propagation with respect to mesh or lattice spacing, comparison to the steady-state plane wave as presented by Junger and Feit [45] was used. Consider a semi-infinite fluid-filled space with a given uniform vibration,  $\dot{w}(t) = \dot{W}e^{-i\omega t}$  at the  $z = 0$  boundary and a non-reflecting boundary as  $z \rightarrow \infty$ . The steady state pressure in the wave guide is  $p(z, t) = \rho c \dot{W} e^{(ikz - i\omega t)}$  where  $k = \frac{\omega}{c}$ . The given function was applied to the  $z = 0$  nodes in a CA domain with the initial values everywhere else uniformly zero, the CA rule was applied for a number of iterations corresponding to over three periods of the steady-state solution, and point-by-point error was calculated relative to the analytic solution over the range  $z \in [0, \frac{2\pi}{k}]$  and plotted in Figure 47. The rate of convergence is linear, as expected for a first-order method.

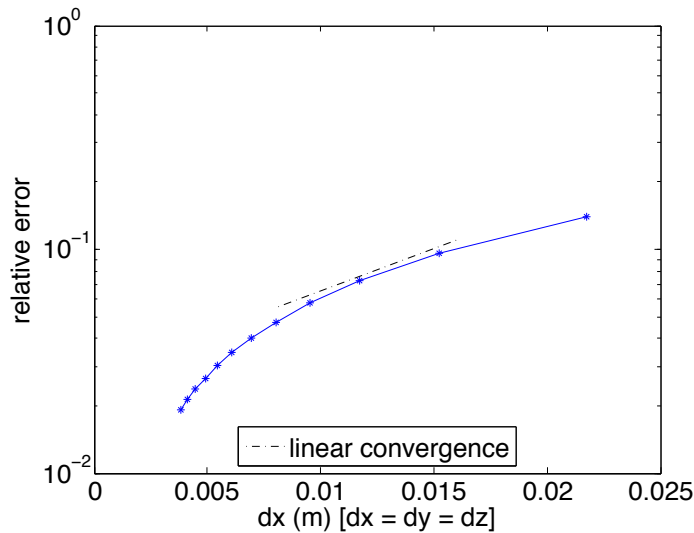


Figure 47: Convergence of CA wave equation rule to analytic solution as a function of  $dx$

## 5. Three Dimensions

It follows from Equations (66) and (67) that the three-dimensional wave equation can be modeled as

$$\phi_C(t + \Delta t) = \frac{1}{3}[\phi_W(t) + \phi_E(t) + \phi_S(t) + \phi_N(t) + \phi_F(t) + \phi_B(t) - 3\phi_C(t - \Delta t)] \quad (70)$$

with the subscripts on the new terms standing for “front” and “back,” respectively. To test this supposition, consider a “point” source located in the center of a domain of interest. As was discussed above, CA is not expected to faithfully model a true point source, so the source under consideration is a smooth radial function that has a maximum value of 1 at the origin of the domain and is zero valued outside a radius of five nodes from the origin. The domain is comprised of 73 equi-spaced nodes in each direction; non-reflecting boundary conditions were applied on all six sides of the domain. Three points in space will be examined: the origin, an arbitrary point inside the initial perturbation ( $r < 5dx$ ), and an arbitrary point outside the initial perturbation ( $r > 5dx$ ). Referring to the notation of Equations (55) - (58),

$$\varphi(x, y, z) = \begin{cases} 1 - \frac{r}{a} & \text{if } r < a, \\ 0 & \text{if } r \geq a \end{cases} \quad (71)$$

$$\psi(x, y, z) = 0 \quad (72)$$

where  $r$  is the cartesian radius,  $\sqrt{x^2 + y^2 + z^2}$ . The analytic solution of the integrals in Equation (58) is not easily calculated, but application of a composite Simpson’s Rule over intervals of  $\frac{\pi}{12}$  will yield a suitable comparison.

Figures 48 – 50 show the analytical solutions at the respective points plotted as a function of time directly over their CA counterparts plotted versus the number of iterations through which the rule has been applied. These plots illustrate a key challenge to CA as identified by Hosoglu [46]: matching the discrete iterations of a cellular automaton to the continuous time domain, or calculating an appropriate time scaling factor (TSF). In one dimension,  $dt = \frac{dx}{c}$  works well, but for three dimensions, as Figure 51 shows, there is a

phase difference resulting from a time scale mismatch. Consider a true point source located at the origin of an otherwise zero-valued CA domain. Following the current CA rule, the earliest a node at  $(dx, dy, dz)$  can reach a value other than zero is after the third iteration; thus  $3dt = \frac{1}{c}\sqrt{dx^2 + dy^2 + dz^2}$ , or, for an equi-axed mesh,  $dt = \frac{dx}{c\sqrt{ndim}}$ . The points of interest for this exercise were chosen arbitrarily, but in such a way that both the inside and outside points are displaced from the origin in all three directions. Comparisons between the analytical and CA solutions plotted with this time equivalency are shown in Figures 52-54.

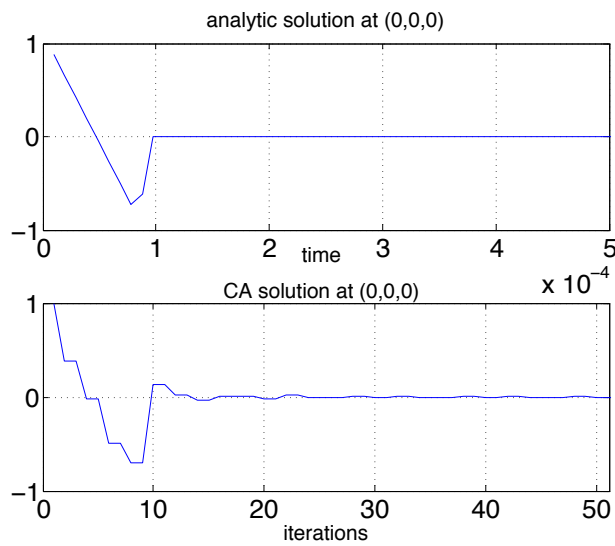


Figure 48: Three-dimensional wave model at domain origin: time vs. iterations

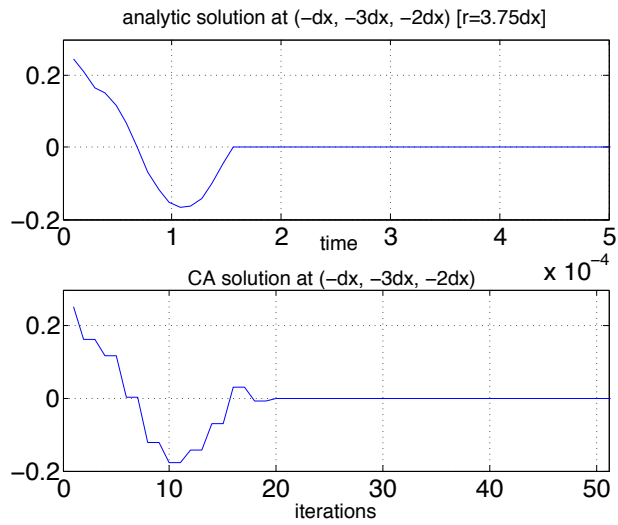


Figure 49: Three-dimensional wave model at a point inside the initial perturbation: time vs. iterations

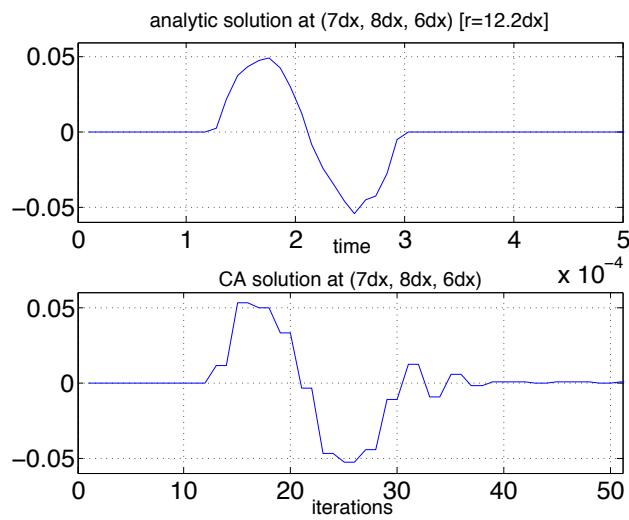


Figure 50: Three-dimensional wave model at a point outside the initial perturbation: time vs. iterations

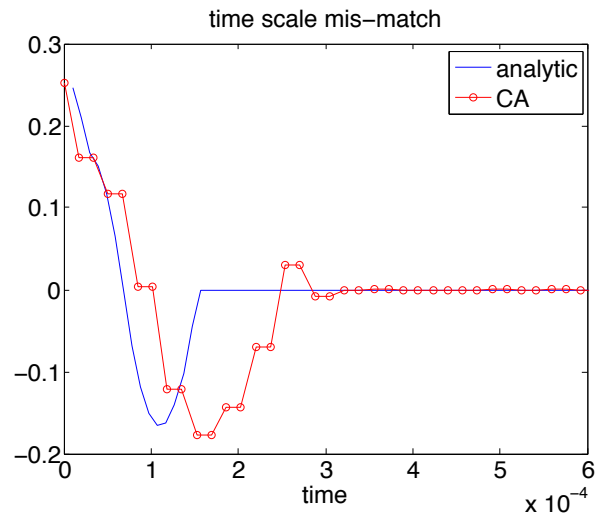


Figure 51: Three-dimensional wave model at a point inside the initial perturbation: analytic solution vs time, CA solution vs  $\frac{dx}{c}$

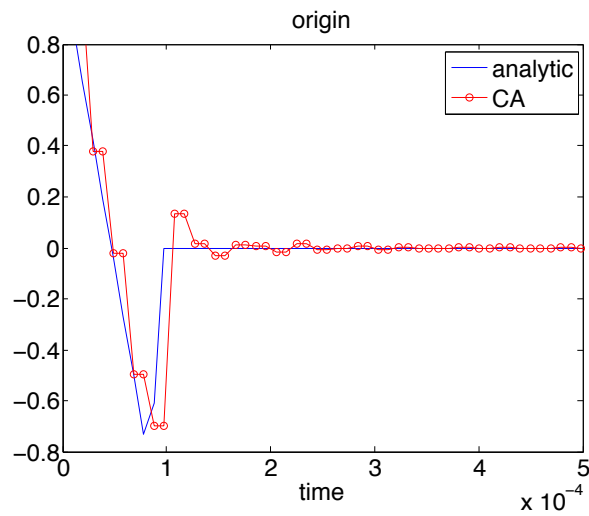


Figure 52: Three-dimensional wave model at a domain origin

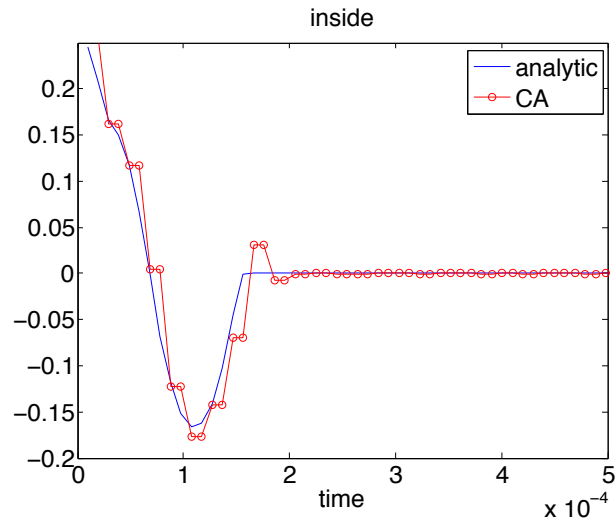


Figure 53: Three-dimensional wave model at a point inside the initial perturbation

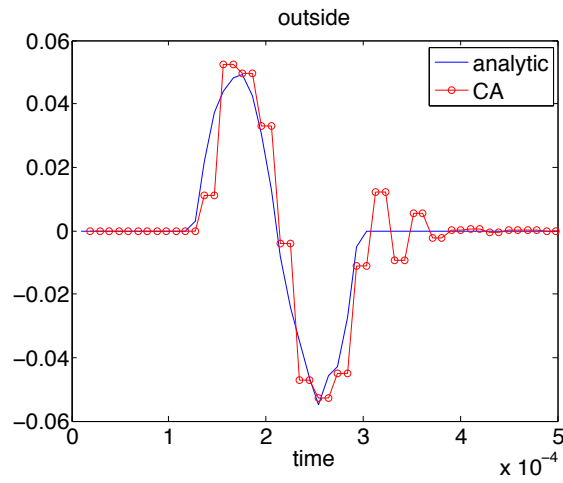


Figure 54: Three-dimensional wave model at a point outside the initial perturbation

#### **D. COUPLING OF FINITE ELEMENT AND CELLULAR AUTOMATA MODELS OF THE WAVE EQUATION**

The CA model of the wave equation for velocity potential is simple to implement and can easily be adapted to a variety of non-trivial boundary conditions, but converting velocity potential back into useful quantities like pressure and velocity as time- and spatial-derivatives is hampered by the alternating update nature of the model. The finite element model, on the other hand updates the value of every point every time-step, but can be computationally expensive and non-trivial boundary conditions can be difficult to implement. A combination of the two methods would seem to resolve the short-comings of each and enable a faithful model of the fluid portion of our fluid-structure interaction.

The general idea is to have several layers of finite elements in contact with the structure and then to have that fluid volume surrounded with a CA domain upon which the non-reflecting and free boundary conditions can be imposed as shown in Figure 55. The two fluid domains will overlap such that the outer layer of finite element nodes will be processed as interior CA nodes whose CA-calculated values become FE-specified boundary values. The next set of FE nodes inside the domain are calculated by the FE machinery and then passed to the CA domain to serve as neighbors for application of the CA rule to the outer set. These node sets are illustrated in Figure 56.

The pre-validation of this scheme was to establish comparable domains of each model, impose a specified velocity potential field on one face of the domains (the top), and specify a fixed, zero-valued boundary condition on the other five faces. The specified input is a radially scaled sinusoid—it achieves its maximum value at the center of the face over which it is applied and is zero beyond a radius of one-half the width of the region. The resulting value of the velocity potential at the respective domain centers compares favorably as shown in Figure 57.

The first full validation of the coupling scheme was to model a joint domain with an imposed velocity potential on the top of the FE portion of the domain which in turn rests atop the CA portion. The four sides of both domains have fixed zero-valued boundary

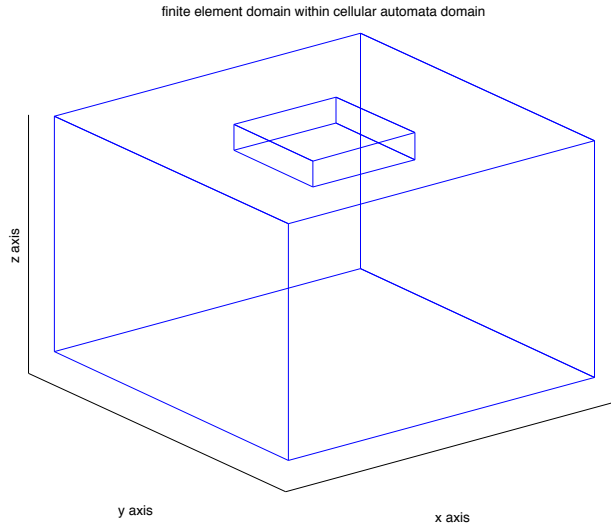


Figure 55: Finite Element fluid domain surrounded by Cellular Automata fluid domain

conditions and the bottom of the CA portion is non-reflecting. The value of the velocity potential on either side of the interface is shown in Figure 58. Next, the specified function on the top of the FE domain (the same radially scaled sinusoid) was treated as a velocity rather than velocity potential. Again, the values of  $\phi$  are compared near the interface between the two models and shown in Figure 59. Next, the domain and interfaces are expanded such that the CA domain surrounds the FE domain on five sides and the non-reflecting boundary condition is applied to all six sides of the outer domain with the exception of the top of the FE domain—velocity is specified there. Those results are shown in Figure 60.

The time-integration of Equation (65) was performed using a Newmark- $\beta$  algorithm with a zero valued  $[C]$  matrix.[47] The cases that involved fixed, zero boundary conditions (Figures 57 - 59) display noticeable high-frequency noise that is suspected to be caused by the sudden change in  $\phi$  value at the boundaries. Despite a smooth input function, the beginning of a similar phenomenon is noticeable in the case with completely non-reflecting boundary conditions as well (Figure 60). The particular Newmark- $\beta$  scheme used ( $\gamma = \frac{1}{2}$ ,  $\beta = \frac{1}{4}$ ) is unconditionally stable and was chosen to ameliorate any potential difficulty

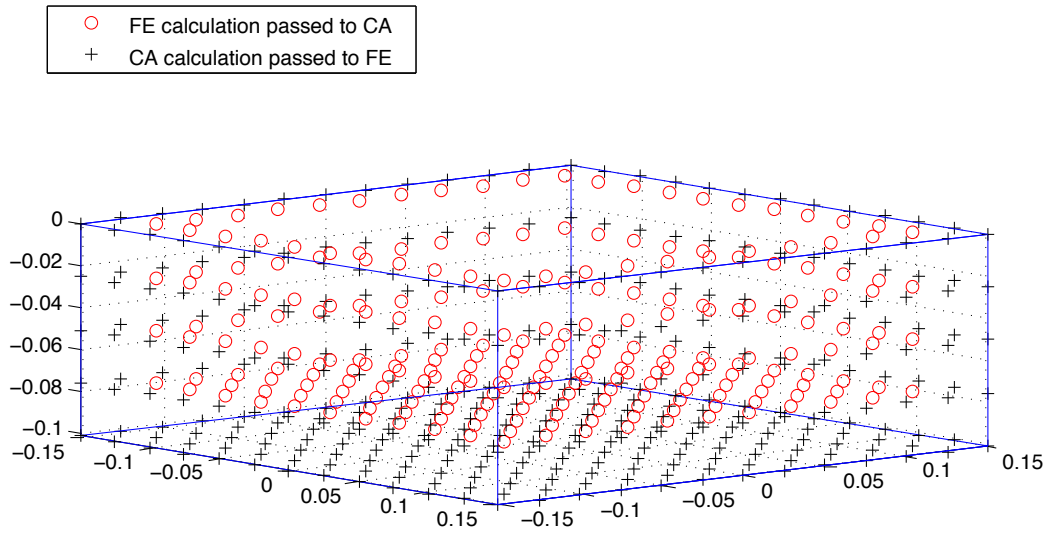


Figure 56: Node sets for exchange of data between fluid domains

arising from  $dt$  being a fixed function of  $dx$ , however a transition to an  $\alpha$ -method (or Hilber-Hughes-Taylor (HHT)) may be necessary to dampen this noise. See Appendix A for details on these methods.

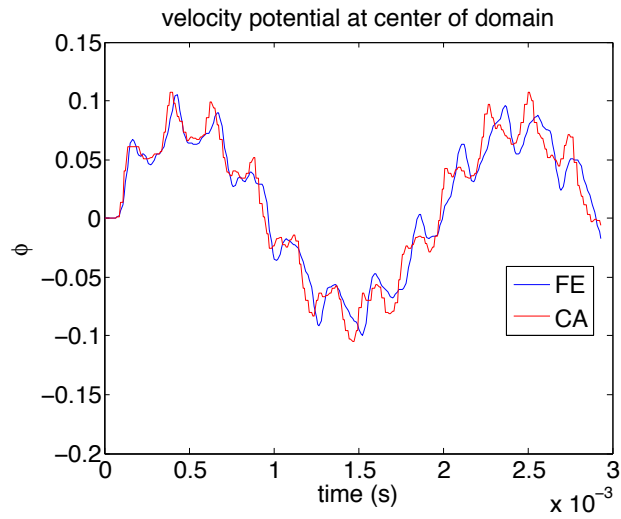


Figure 57: Comparison of velocity potential propagation between finite element and cellular automata models with common Dirichlet boundary conditions

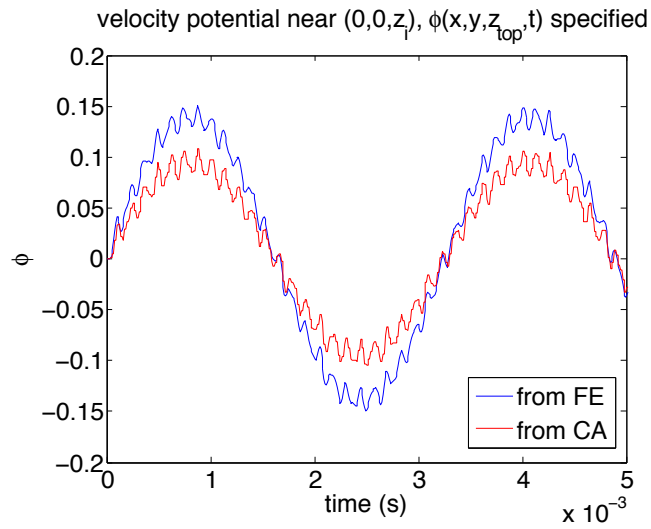


Figure 58: Velocity potential propagation between finite element and cellular automata domains, velocity potential ( $\phi(\text{top})$ ) specified

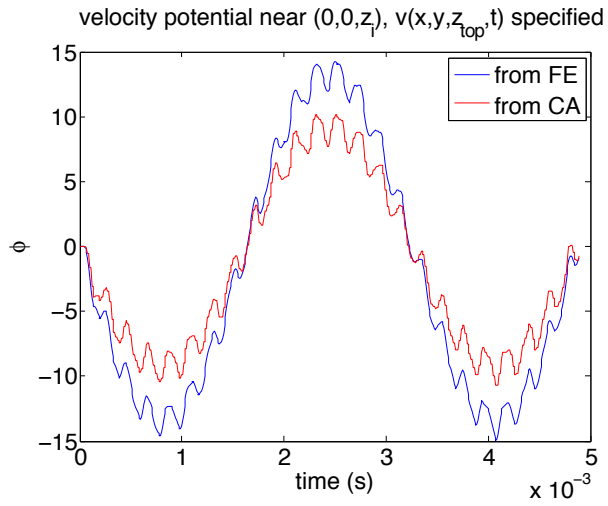


Figure 59: Velocity potential propagation between finite element and cellular automata domains, velocity ( $v(\text{top})$ ) specified

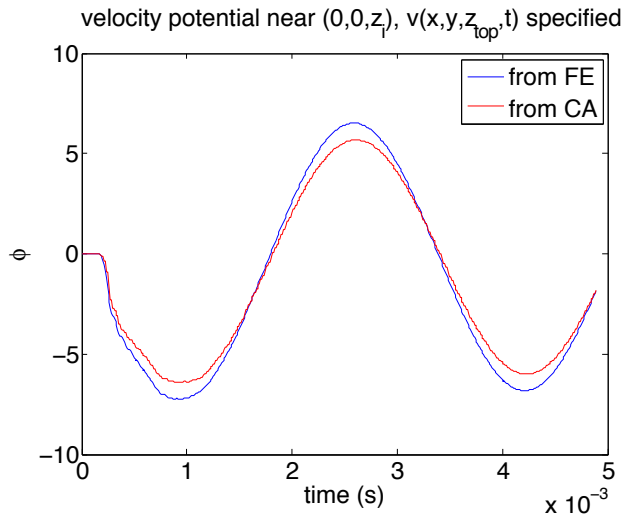


Figure 60: Velocity potential propagation between finite element and cellular automata domains, FE inside CA, velocity ( $v(\text{top})$ ) specified, non-reflecting boundary conditions

## 1. Comparison with Homogeneous Fluid Domain

Figure 61 demonstrates close agreement between the response of a composite domain and a homogeneous fluid domain subject to the same input and boundary conditions.

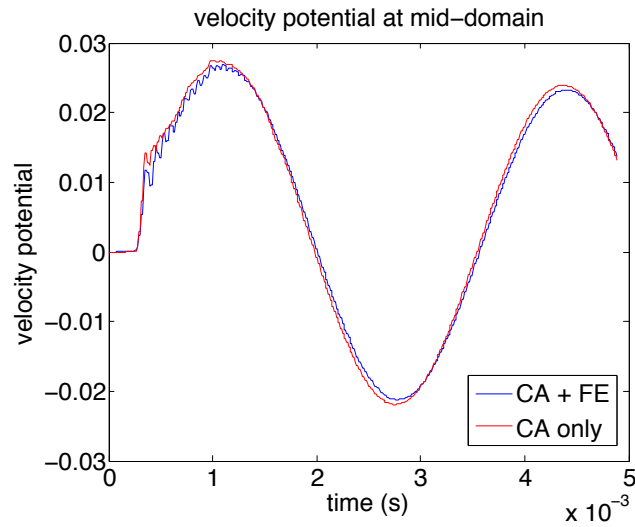


Figure 61: Comparison of velocity potential at mid-domain resulting from specified value on one face: FE + CA domain vs. homogeneous CA domain

THIS PAGE INTENTIONALLY LEFT BLANK

## V. RESULTS

### A. ACOUSTIC FIELD FLUID-STRUCTURE INTERACTION

This chapter will combine the structural and fluid models discussed so far and examine their interactions. Finally, comparison with experimental results will be presented.

#### 1. Information Exchange

As previously discussed, the fluid model used in this work is that of the velocity potential. At each time step the transverse velocity of the structure is transmitted into the fluid where it is converted to velocity potential and propagated through the fluid domain according to the wave equation. The resulting fluid pressure, a function of the time derivative of the velocity potential is then applied to the structure via its load vector for calculation of displacement and velocity during the next time step. Unconditionally stable time integrators across the various domains allows the selection of time step size based on the CA time-scaling factor.

For simplicity the meshes of the structure, the FE fluid, and the CA fluid are mutually conforming.

#### 2. Homogeneous Isotropic Single-Layer Structure

The algorithm described above was validated by modeling a clamped foot square plate one-quarter inch thick homogeneously comprised of an isotropic material. Both CG and DG models were generated. Fresh water material properties were used for the fluid model. Figure 62 shows the transverse displacement of the center of the plate subject to a constant concentrated force applied at its center. The dry case is the resulting oscillation about its predicted static deflection; the wet case shows that both magnitude and frequency of the oscillation have been altered as a result of the FSI. Kwon [48] discussed this phenomena and observed the effects of the elastic modulus and density of the structure. Specifically, he noted that a structure with a density close to that of the fluid would

be more affected by the interaction. This observation is borne out in Figures 63 and 64 for which the respective material properties were changed from the baseline case. The baseline model has a structural density 2.7 times that of the fluid, a frequency ratio (dry/wet) of 1.84 and an amplitude ratio (first peak - first trough, dry/wet) of 2.49. The double modulus case (Figure 63) shows a slightly higher frequency oscillation about a lesser static deflection in the dry case; the dry/wet frequency ratio is 1.86 and amplitude ratio is 2.15: a lesser relative change. The double density case (Figure 64) shows the expected lower frequency oscillation in the dry case, but also a dry/wet frequency ratio of 1.49. The dry/wet amplitude ratio for the double density case is 2.00.

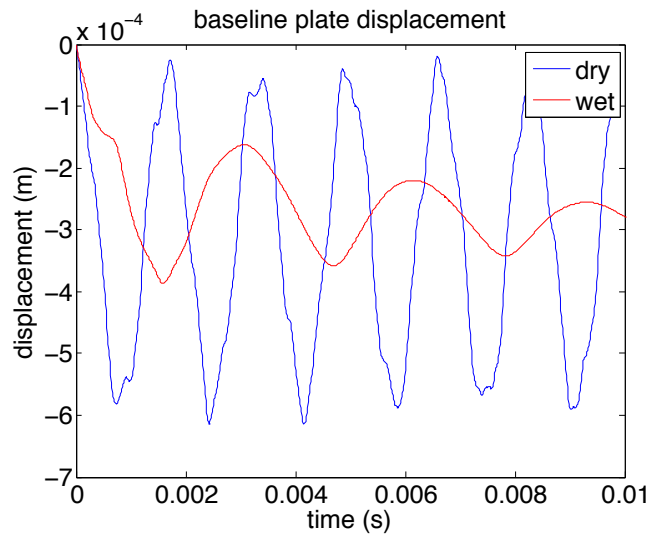


Figure 62: Displacement of clamped plate with and without fluid-structure interaction

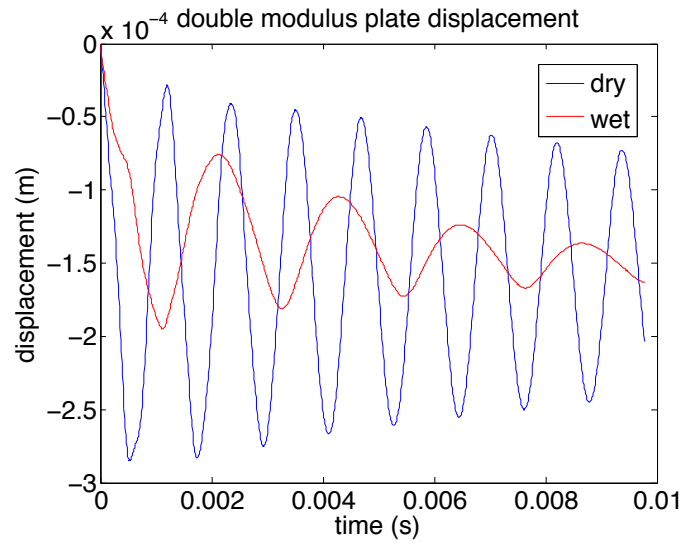


Figure 63: Displacement of clamped plate of double modulus with and without fluid-structure interaction

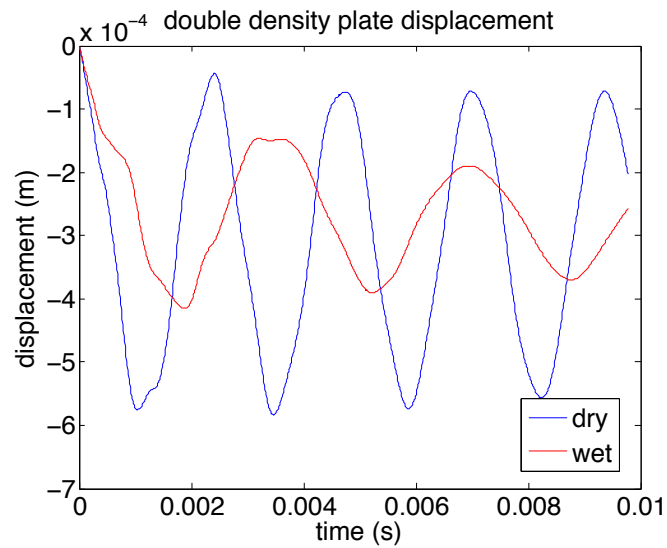


Figure 64: Displacement of clamped plate of double density with and without fluid-structure interaction

### 3. Two-layer Plates

The clamped plates modeled in this section are each 0.3048m x 0.3048m x 3.5mm and comprised of two thickness layers and sixteen elements in each planar direction. The material is an isotropic approximation of E-glass. Initial conditions were zero displacement and velocity; a constant concentrated force of 1000N applied at the center of the plate at the first time step. The “damaged” plates had a four element by four element debonding patch inserted between the two layers at the center of the plate. This debond was of the partial disconnection method described in Chapter III. Figures 65 – 67 display the time histories of displacement, velocity, and normal strain in the plane on the bottom of each plate. The stress profiles in Chapter III showed that maximum values were at the edges of the damage zone; similar phenomena are expected in strain values, but as Figure 68 shows, the strains at the center of the plate for both dry and wet cases is of greater magnitude than those at the  $+y$  edge of the damage zone (the maximum numerically of the four edges). This further suggests that an interface layer is necessary to properly model debonding in laminated composites and other layered structures. The density of E-glass is twice that of water, close enough to observe an added mass effect in the case of FSI. That is, a structure with density comparable to that of fluid reacts not only to the pressure effect of the fluid—dampening the amplitude of its vibrations, but also at a lower frequency as though it was a more massive structure.

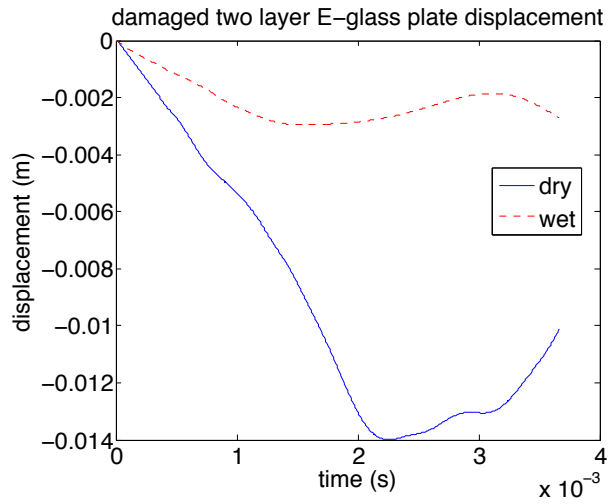


Figure 65: Displacement of damaged clamped two layer E-glass plate with and without fluid-structure interaction

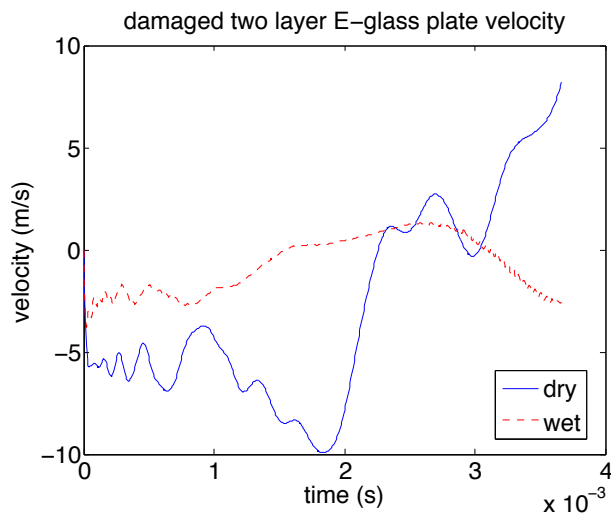


Figure 66: Velocity of damaged clamped plate two layer E-glass plate with and without fluid-structure interaction

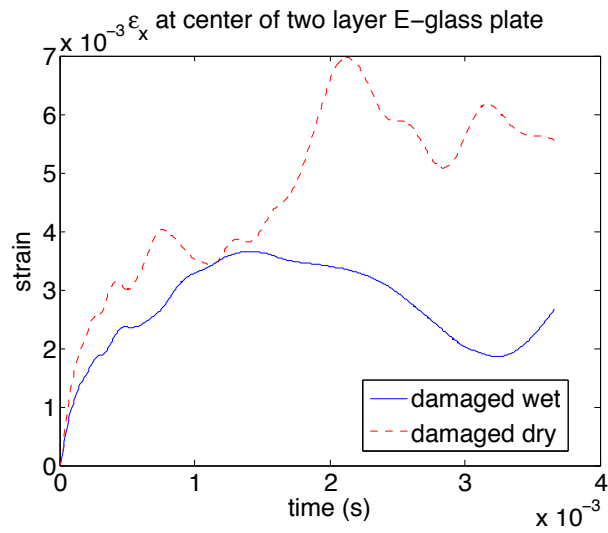


Figure 67: Strain at center of clamped two layer E-glass plate with and without fluid-structure interaction

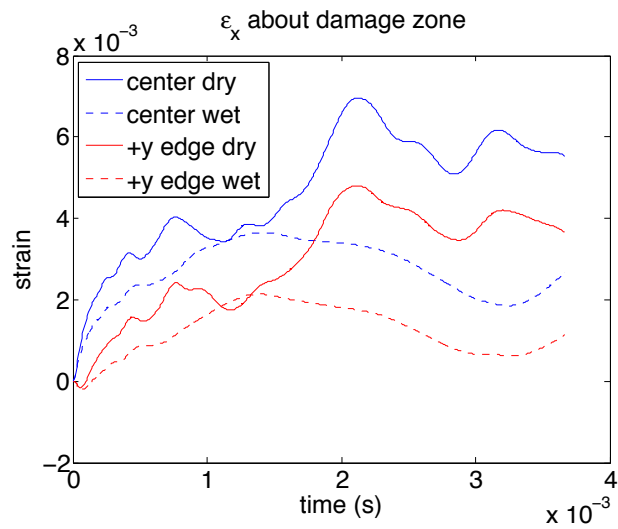


Figure 68: Strain at center and edge of damage zone of clamped two layer E-glass plate with and without fluid-structure interaction

#### 4. Three-layer Plates

The two-layer model of the previous sub-section did a poor job of reflecting debonding damage within a laminated plate. A three-layer model with a thin interface layer with properties approximating a common adhesive inserted between two layers of E-glass was subjected to the same loading and boundary conditions (zero initial displacement and velocity, 1000 N concentrated force at center, clamped edges); responses were calculated for five-hundred time steps. Figures 69 and 70 show that the displacement and velocity responses of the center of the plate do not reflect the presence or absence of a debonding zone, but do demonstrate FSI mass effects in a fashion similar to that of the two-layer model. Figure 71 shows that the strain calculated in the E-glass elements reflects presence or absence of damage only mildly. Figure 72, on the other hand, shows clearly that the interface layer is profoundly affected by the presence of a damage zone. To be clear, the strain values at the centers of the interface layers of the damaged plates are not identically zero, but they are four orders of magnitude lower than their undamaged counterparts.

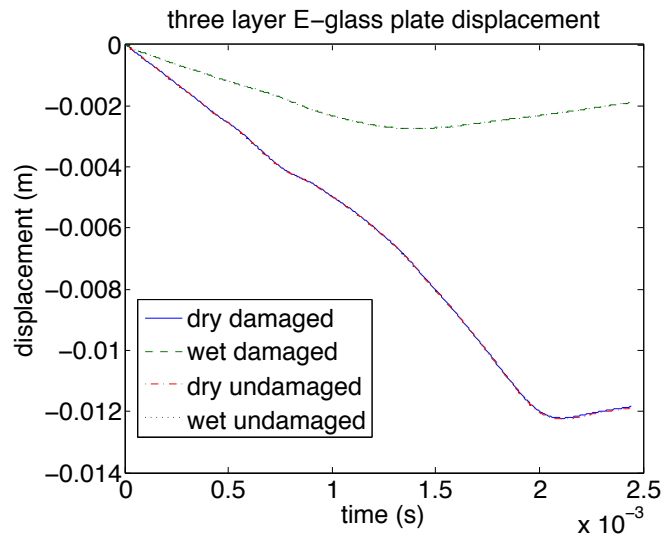


Figure 69: Displacement of clamped three layer E-glass plate with and without fluid-structure interaction and with and without damage

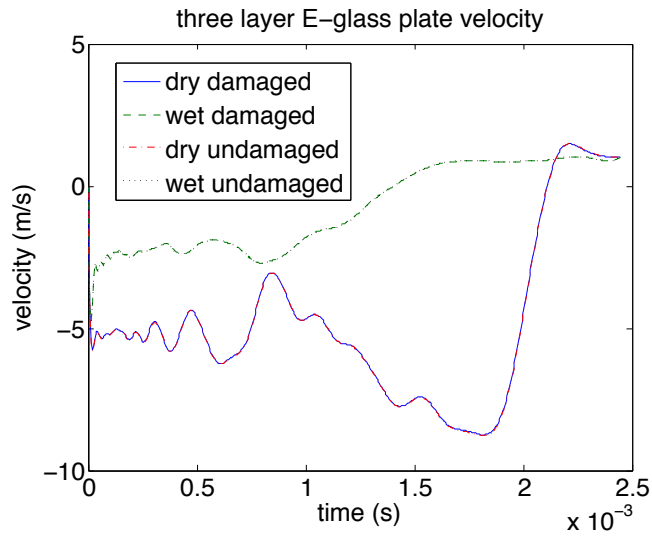


Figure 70: Velocity of clamped three layer E-glass plate with and without fluid-structure interaction and with and without damage

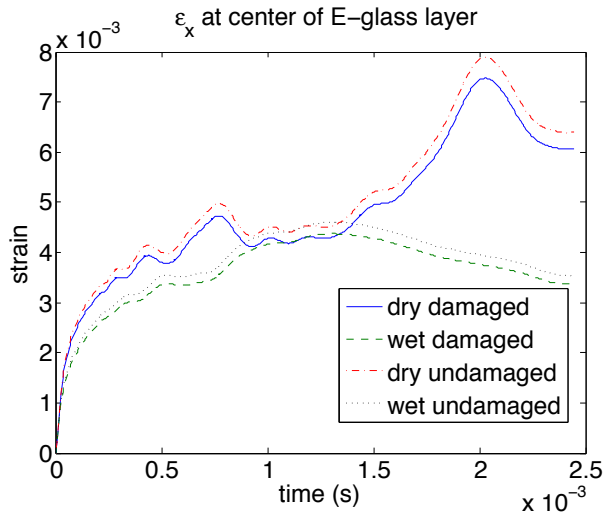


Figure 71: Strain of clamped three layer E-glass plate with and without fluid-structure interaction and with and without damage at center of lower E-glass layer

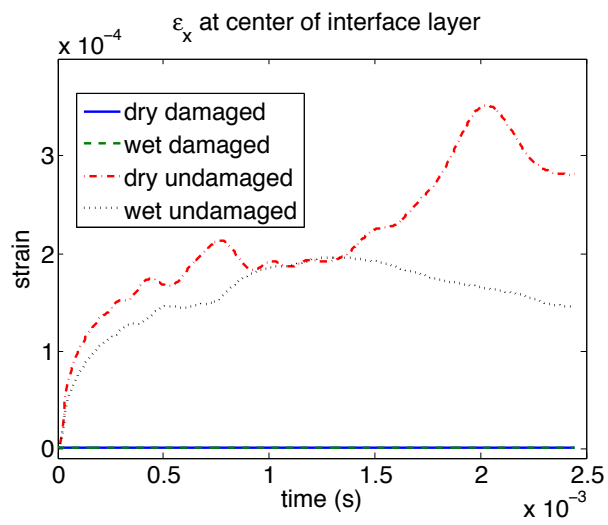


Figure 72: Strain of clamped three layer E-glass plate with and without fluid-structure interaction and with and without damage at center of interface layer

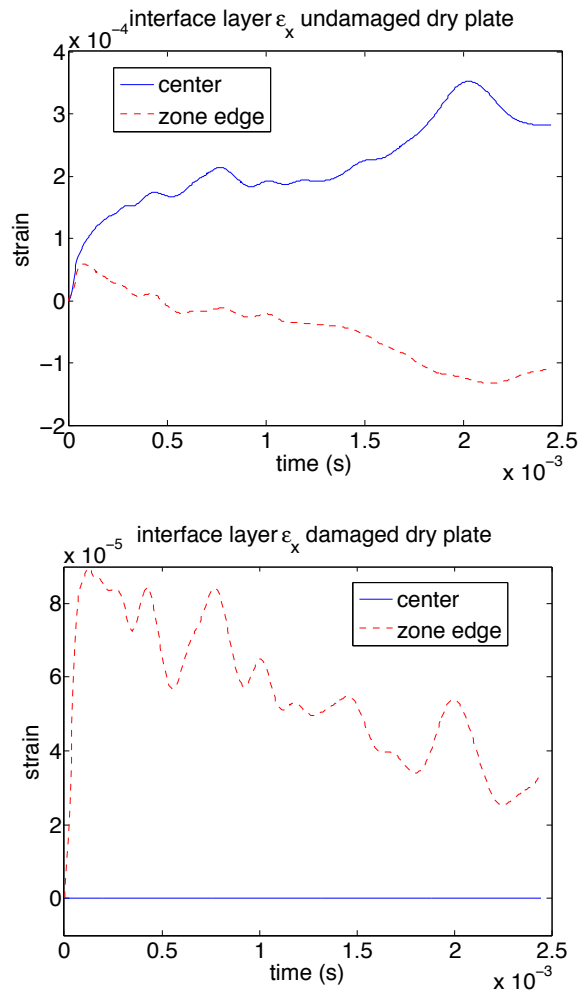


Figure 73: Strains in dry clamped three layer E-glass plate with and without damage

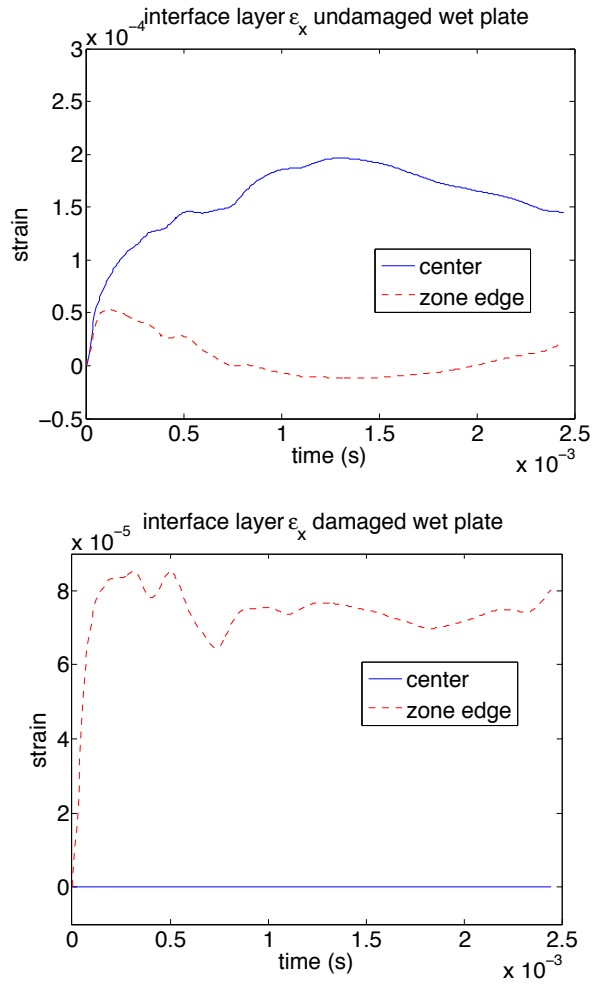


Figure 74: Strains in wet clamped three layer E-glass plate with and without damage

## B. EXPERIMENTAL VALIDATION

Recent experimental work by Kwon and his students [49], [50], [51], [29] examined the response of composite plates to low velocity impact with and without fluid-structure interaction(s). In general, they found that for a given impact weight dropped from the same height, structures with lower density relative to the fluid in question experienced higher resultant forces and consequently greater damage than the same material in dry conditions. Additionally, they noted that the initial observable damage mode was delamination occurring on the face of the plate opposite the impact site.

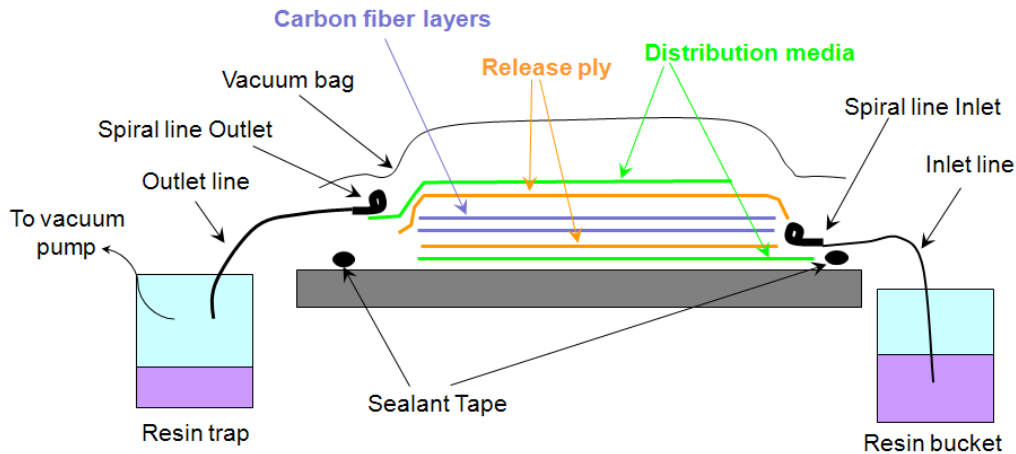


Figure 75: Schematic of VARTM for plate manufacture. From [49]

In his work, Conner [29] used a Vacuum Assisted Resin Transfer Molding technique, shown in Figure 75, to construct a series of 12in by 12in composite plates comprised of sixteen layers of E-glass (approximately 3.5mm thick in toto) and subjected them to low-velocity impact forces that resulted from dropping a 10.8kg weight from various heights to the center of the plate(s) using the assembly shown in Figures 76 and 77. The plates were instrumented with strain rosettes at four set positions and oriented such that one channel returned  $\varepsilon_x$  directly;  $\varepsilon_y$  was calculated as a function of all three channels and the included

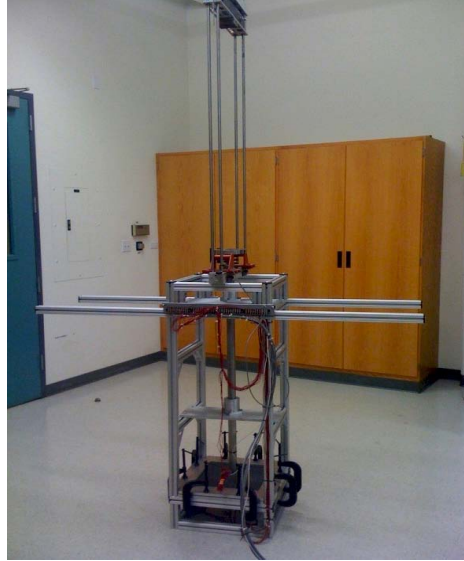


Figure 76: Drop Weight Rig used in Impact Testing. From [48]

angles as can be found in many solid mechanics textbooks including [52]. Data was sampled at a frequency of 10,000 Hz ( $dt = 10^{-4} s$ ).

Numerical comparison with this experimental data was conducted using a DG structural model comprised of a single layer of plate elements with a discretization of twelve elements in each planar direction. The overall structure has a length to thickness ratio of 87:1 and each element has a length to thickness ratio of 7.3:1. In this model the material properties used are those of E-glass, but treated as an isotropic material—the Young’s modulus along its fiber direction was taken in all three directions. The mass matrix is lumped and therefore, diagonal. The dry response was calculated using the  $\alpha$ -method time integration of the equation of motion for the plate. The wet, or FSI, response was calculated according to the acoustic field FSI described in the last chapter with time step size for the entire model equal to the TSF for the CA portion of the fluid model.

The force inputs to the numerical plates were smoothed versions of the experimentally measured force data in the time region of interest—the main impact. The smoothing was conducted by sampling the raw data every five time steps, generating an interpolation

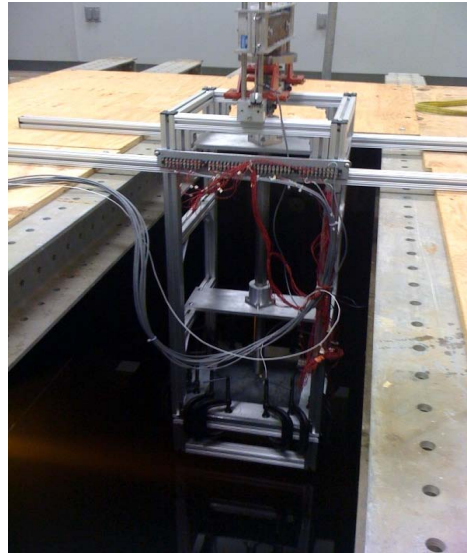


Figure 77: Drop Weight Rig as used for Impact Testing with FSI. From [48]

function (using MATLAB's `interp1` function with the `spline` option) and evaluating the interpolation function at every required time step for the model. For the dry cases, the same time step size as the experimental was used. Figure 78 shows the raw experimental force data and the smoothed version as generated for the dry case; Figure 82 shows the force data used for the FSI case.

The calculated time history of the displacement field was used to calculate a time history of the strain vector at nodal points throughout the domain of the plate. Those nodes closest to the positions of the strain gages in the experimental work were examined relative to the recorded data and are plotted in Figures 79 – 81 for the dry plate and Figures 83 – 85 for the FSI case. All show good qualitative agreement between experimental and numerical data. Differences can be attributed to the smoothing of the input force, ignoring impact effects, the isotropic treatment of an orthotropic material, the approximation of structural thickness, approximate positioning of strain gages, and mis-alignment of strain gages. The data correlating with gage 1 appears to show better overall agreement than the other two, most likely because that gage was located approximately equi-distant from both the point

of impact and the clamped boundaries of the plate. The other gages were closer to, and therefore, more exposed to the effects of the physical boundaries of the plate.

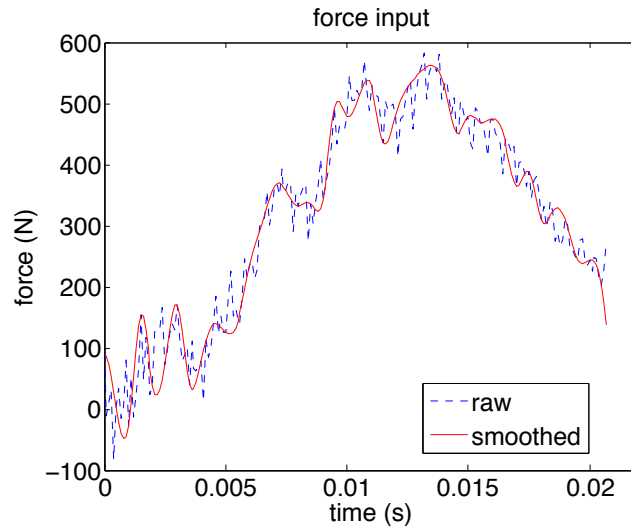


Figure 78: Raw and smoothed experimental force data for dry plate

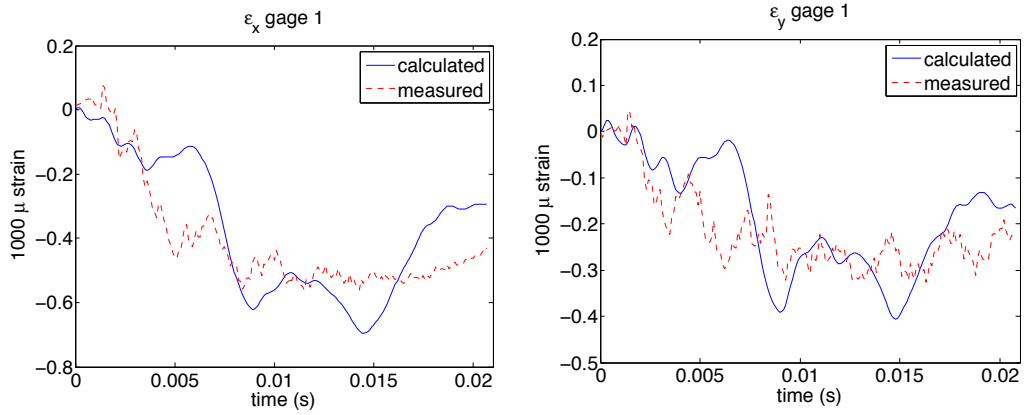


Figure 79: Measured versus calculated strain, dry plate, gage 1

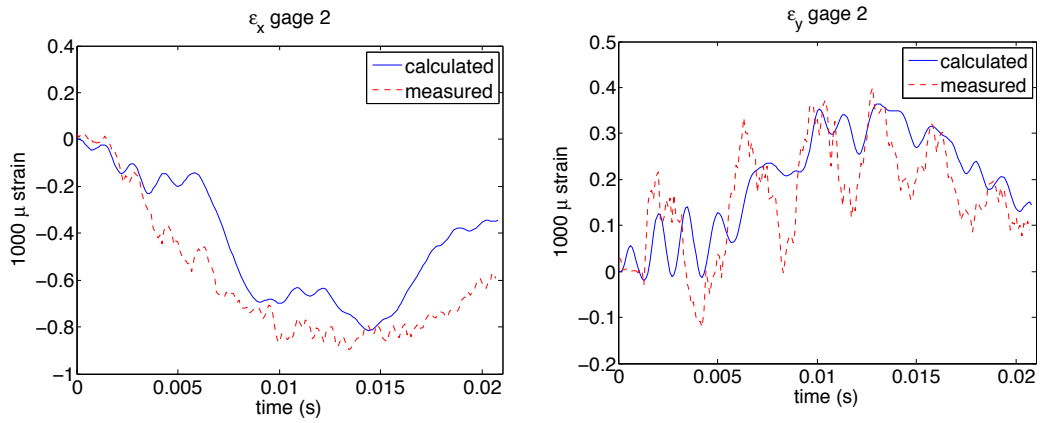


Figure 80: Measured versus calculated strain, dry plate, gage 2

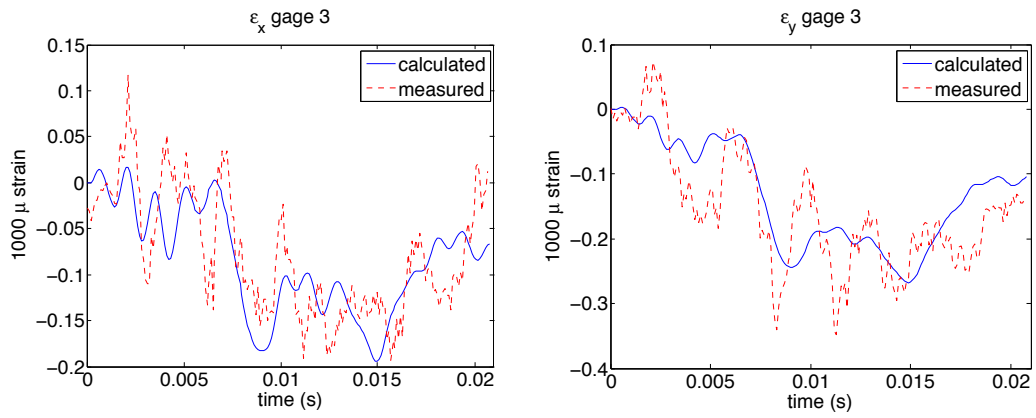


Figure 81: Measured versus calculated strain, dry plate, gage 3

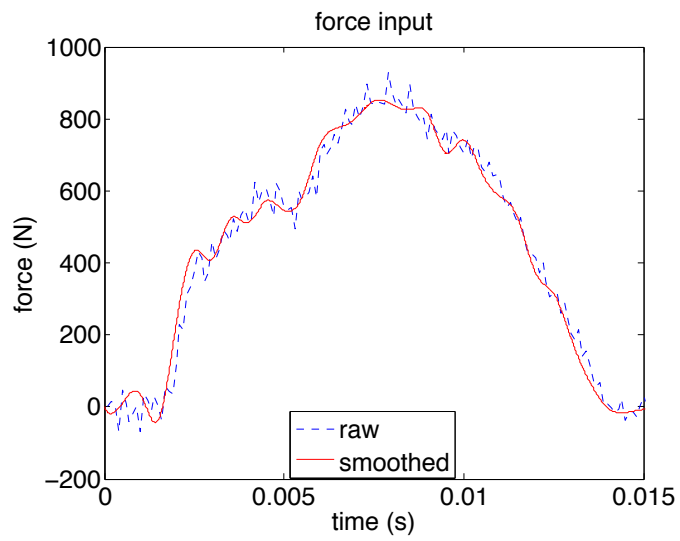


Figure 82: Raw and smoothed experimental force data for wet plate

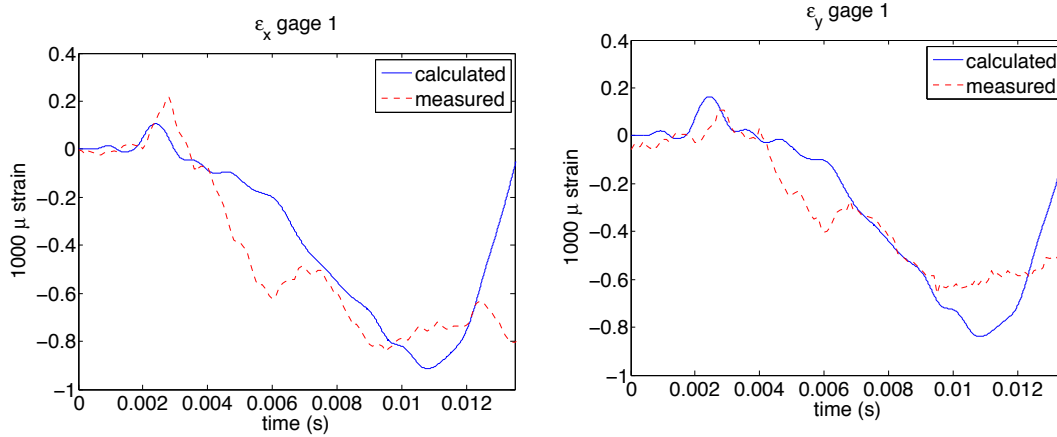


Figure 83: Measured versus calculated strain, wet plate, gage 1

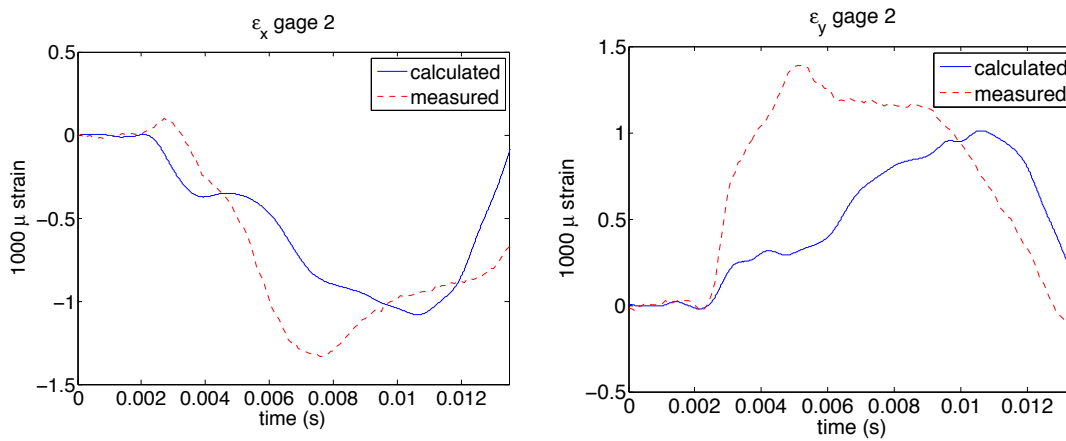


Figure 84: Measured versus calculated strain, wet plate, gage 2

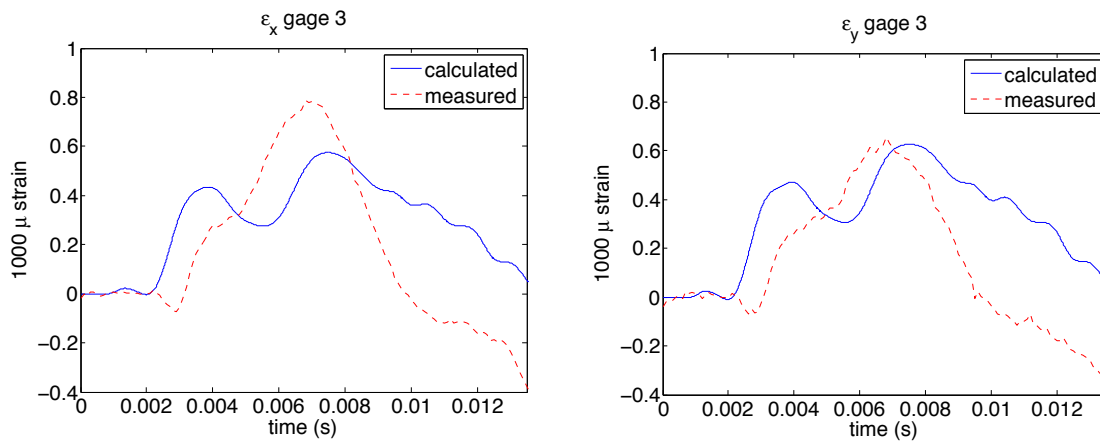


Figure 85: Measured versus calculated strain, wet plate, gage 3

THIS PAGE INTENTIONALLY LEFT BLANK

## VI. CONCLUSION

### A. SUMMARY OF FINDINGS

The goal of this work was to develop computational techniques to accurately model and simulate dynamic responses and failures of composite structures in an acoustic field. After implementing a nodal three-dimensional element to verify basic computational methodology, a displacement-only plate finite element was formulated and implemented using Discontinuous Galerkin (DG) methodology. Such a displacement-only element allows construction of multi-layered structures like sandwich plates and other laminated composites in a manner similar to full three-dimensional solid finite elements. Results generated from this formulation compare favorably with theoretical predictions as well as existing CG numerical models for both static and dynamic responses for both simple and multi-layered plate structures.

Application of the new element to the analysis of failure initiation and propagation in sandwich composite structures shows great promise. Static qualitative stress profiles are similar to those found using CG techniques, but the elemental rather than nodal connectivity used in DG formulations suggests a simple means of modeling debonding between material layers by disconnecting their respective elements in the global stiffness matrix. Complete disconnection of neighboring elements in an imposed debonding zone was shown to be incorrect because it allowed the core layer to deflect not only through the disconnected resin layer but also through the still-present skin layer. Partial disconnection—removing connectivity between opposing pairs of dofs in the planar directions but retaining weak connectivity for transverse pairs of dofs resulted in a stress profile that makes good qualitative sense. Maximum stress values in both skin and core layers decreased in magnitude and moved from the center of the plate to the edges of the debonding zone, behaving like a stress concentration. The simplicity of this partial disconnection method can be a tremen-

dous computational savings when modeling the progression of damage without need for re-meshing or recalculation of the global stiffness matrix.

Examination of FSI for the impact problem does not require a full fluid-flow model—the propagation of velocity potential according to the wave equation in the acoustic domain is sufficient for these purposes; as such, an extension of Cellular Automata (CA) from two to three-dimensions in modeling the acoustic field was demonstrated and validated. CA was chosen for this application not only because of the simplicity of its update rule, but also because of its flexibility in the implementation of non-reflecting boundary conditions. The alternating update nature of CA makes calculation of both spatial and time derivatives—required to convert the velocity of the structure into velocity potential in the fluid domain and to convert velocity potential into a pressure field—difficult. Insertion of a small finite element interface zone between the structure and the CA fluid domain resolved this difficulty for a relatively low computational cost. The combination of a small FE acoustic domain with an enveloping CA domain proved to be an efficient way to implement non-reflecting boundary conditions.

Finally, the combined model of a DG structure interacting with a FE+CA fluid domain was shown to have good agreement between calculated and experimentally measured strain values for plates subject to low-velocity impact in the pre-damage regime. In particular, the added mass effect on structures with low density relative to the fluid medium was apparent in both simulation and experimental comparisons.

The methods developed and examined in this study: the displacement-only DG plate finite element, the partial disconnection failure model, and the hybrid FE+CA acoustic field model, show great promise for flexible and accurate modeling of debonding initiation and propagation in sandwich and laminate composite structures subject to FSI.

## **B. FUTURE WORK**

This work should be viewed as a starting point for further investigation into the utility of DG methods in composite failure modeling.

First and foremost, the current formulation must be re-implemented to be a true element-wise computation in order to reap the benefits of DG not just pay the costs of solving for a greater number of dof. This type of update will enable more efficient and flexible modeling of larger problems, including more refined meshes, more complex geometry, and approaches that address all levels of multi-scale analysis of composite materials. Such a re-implementation should also enable the coupling of the current DG formulation with CG codes. This should be readily achievable as the current formulation is derived from one with such coupling as a specific goal. This sort of coupling can be used as an alternative to refining the mesh in the areas of interest like existing or expected damage by replacing the refined mesh with DG elements in order to better examine the physical phenomena.

A more computationally efficient implementation should also include and enable progressive failure modeling both through inclusion of traction-separation type models for the post-damage regime, but also through propagation of damage beyond its initiation site. Addition of a full impact-impulse model for force input should enable even more faithful modeling and closer comparison with experimental results.

The closer a computational model approaches observed physical phenomena, the more useful and trustworthy its results in evaluating more complex geometries and operating environments.

THIS PAGE INTENTIONALLY LEFT BLANK

## APPENDIX A. TIME INTEGRATION ALGORITHMS

This appendix contains explication of the algorithms used to solve the matrix-vector equation of motion in this work. Implicit methods are favored for their stability independent of size of time step—a concern when matching various domains. All methods are trying to solve

$$[M]\{\ddot{u}\} + [C]\{\dot{u}\} + [K]\{u\} = \{f\} \quad (73)$$

for  $\{u\}$ . Solutions for the two time derivatives are used as needed to update  $\{u\}$ ; in the finite element fluid domain  $\{\dot{u}\}$  is also used for a pressure calculation.

### A. NEWMARK- $\beta$ METHOD

The below algorithm, taken from [47] was initially implemented to serve as time integrator of Equation (73) by using the weighted averages

$$\{\dot{u}\}_{n+1} = \{\dot{u}\}_n + [(1 - \gamma)\{\ddot{u}\}_n + \gamma\{\ddot{u}\}_{n+1}] \cdot dt \quad (74)$$

$$\{u\}_{n+1} = \{u\}_n + \{\dot{u}\}_n \cdot dt + [(1 - 2\beta)\{\ddot{u}\}_n + 2\beta\{\ddot{u}\}_{n+1}] \cdot \frac{dt^2}{2} \quad (75)$$

substituting and rearranging terms results in

$$\begin{aligned} [M + \gamma dt C + \beta dt^2 K]\{\ddot{u}\}_{n+1} &= \{f\}_{n+1} \\ &- [(1 - \gamma)dt C + (1 - 2\beta)\frac{dt^2}{2}K]\{\ddot{u}\}_n - [C + dt K]\{\dot{u}\}_n - K\{u\}_n \end{aligned} \quad (76)$$

which can be solved for  $\ddot{u}$  and then  $\dot{u}$  and, in turn,  $u$  at each time step. The method is unconditionally stable for  $2\beta \geq \gamma \geq \frac{1}{2}$ . Parameter choices are  $\gamma = \frac{1}{2}$  and  $\beta = \frac{1}{4}$  correspond to Newmark's Constant Average Acceleration Method.

Dirichlet and Neumann boundary conditions can be imposed nodally by solving for the current acceleration on the boundary through Equations (74) and (75), zeroing the

corresponding rows of the compound left-hand-side matrix, setting the diagonal elements of those rows to 1 and substituting the boundary accelerations into the right-hand-side vector.

## B. $\alpha$ -METHOD

Hilber, Hughes, and Taylor improved upon Newmark- $\beta$  with their introduction of the  $\alpha$ -method [53]–[54]. This method is designed to dissipate high frequency noise without degrading the order of solution accuracy. The update rules for  $\{u\}$  and  $\{\dot{u}\}$  are the same as in (75) and (74), but now the equation of motion is also a weighted average:

$$[M]\{\ddot{u}\}_{n+1} + (1 + \alpha)[C]\{\dot{u}\}_{n+1} - \alpha[C]\{\dot{u}\}_n + (1 + \alpha)[K]\{u\}_{n+1} - \alpha[K]\{u\}_n = \{f(t_{n+1+\alpha})\} \quad (77)$$

which is rearranged to

$$[M + (1 + \alpha)dt(\gamma C + \beta dt K)]\{\ddot{u}\}_{n+1} = (1 + \alpha)f_{n+1} - \alpha f_n - (1 + \alpha)dt[(1 - \gamma)C + \frac{dt}{2}(1 - 2\beta)K]\{\ddot{u}\}_n - [C + dt(1 + \alpha)K]\{\dot{u}\}_n - K\{u\}_n \quad (78)$$

and then solved for  $\{\ddot{u}\}_{n+1}$  which is then used to update  $\{\dot{u}\}_{n+1}$ , and  $\{u\}_{n+1}$ . Dirichlet boundary conditions are applied nodally via rearrangement of Equation (75) to solve for prescribed values of the right hand side of Equation (78). This method is unconditionally stable when  $\alpha \in [-\frac{1}{3}, 0]$ ,  $\gamma = (1 - 2\alpha)/2$ , and  $\beta = (1 - \alpha)^2/4$ . When  $\alpha = 0$  this method reduces to Newmark's Constant Average Acceleration Method.

## C. TIME DISCONTINUOUS GALERKIN METHOD

Another time integrator considered but not fully implemented in this work is the Time Discontinuous Galerkin (TDG) method presented by Chien, Yang, and Tang [55].

They present time as yet another domain that can be discretized by finite elements, in particular as discontinuous finite elements, as shown in Figure 86. For the undamped equation of motion ( $[C]=0$  in Equation (73)), they generate the following matrix equation to solve for the displacement and velocity at each end of a particular time interval (or element):

$$\begin{bmatrix} \frac{1}{2}K & \frac{1}{2}K & -\frac{1}{3}\Delta t_n K & -\frac{1}{6}\Delta t_n K \\ -\frac{1}{2}K & \frac{1}{2}K & -\frac{1}{6}\Delta t_n K & -\frac{1}{3}\Delta t_n K \\ \frac{1}{3}\Delta t_n K & -\frac{1}{6}\Delta t_n K & \frac{1}{2}M & \frac{1}{2}M \\ \frac{1}{6}\Delta t_n K & \frac{1}{3}\Delta t_n K & -\frac{1}{2}M & \frac{1}{2}M \end{bmatrix} \begin{Bmatrix} u_1 \\ u_2 \\ v_1 \\ v_2 \end{Bmatrix} = \begin{Bmatrix} Ku_1^- \\ 0 \\ F_1 + Mv_1^- \\ F_2 \end{Bmatrix} \quad (79)$$

where  $K$  and  $M$  are the usual stiffness and mass matrices and

$$F_1 = \int_{I_n} \phi_1(t) F dt \quad (80)$$

$$F_2 = \int_{I_n} \phi_2(t) F dt \quad (81)$$

where  $F$  is the usual applied load vector and  $\phi_1(t)$  and  $\phi_2(t)$  are the time shape functions shown in Figure 86. Simplifying and recasting some terms results in

$$\begin{bmatrix} K & 0 & -\frac{1}{6}\Delta t_n K & \frac{1}{6}\Delta t_n K \\ 0 & K & -\frac{1}{2}\Delta t_n K & -\frac{1}{2}\Delta t_n K \\ 0 & 0 & M^* & \frac{2}{3}M \\ 0 & 0 & \frac{1}{3}\Delta t_n^2 K & M^* \end{bmatrix} \begin{Bmatrix} u_1 \\ u_2 \\ v_1 \\ v_2 \end{Bmatrix} = \begin{Bmatrix} Ku_1^- \\ Ku_1^- \\ F_1^* \\ F_2^* \end{Bmatrix} \quad (82)$$

where

$$M^* = M + \frac{1}{6}\Delta t_n^2 K \quad (83)$$

$$F_1^* = \frac{5}{3}(F_1 + Mv_1^-) - \frac{1}{3}F_2 - \frac{2}{3}\Delta t_n K u_1^- \quad (84)$$

$$F_2^* = F_1 + F_2 + Mv_1^- - \Delta t_n K u_1^- \quad (85)$$

which can be solved for the velocity terms from which displacements may be calculated directly. They also show that this method is also unconditionally stable, making it an intriguing avenue for future work in structural dynamics.

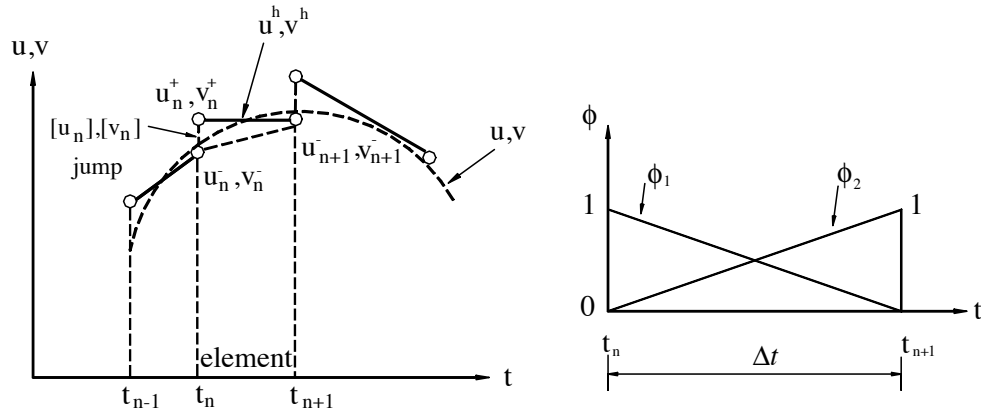


Figure 86: Temporal elements for TDG method. From [55]

## APPENDIX B. IMPLEMENTATION DETAILS

The discussion of the fluid and structural and fluid models in the main body of this thesis is (moderately) general and symbolic. All implementation was in MATLAB, and run on a MacBook Air (mid-2009), MacBook Pro (mid-2011), or on the Hamming cluster.

### A. MESHING

The various domains were meshed for human convenience rather than any matrix bandwidth considerations. In general, node and element numbering proceeds from  $(x_{min}, y_{min}, z_{min})$  along the  $x$ -axis, then increment up the  $y$ -axis, and then up the  $z$ -axis. While the code does execute full and proper Jacobian calculations for arbitrarily oriented elements, in general the  $x$ -axis corresponds to the canonical  $r$ -axis; the  $y$ -axis corresponds to the canonical  $s$ -axis, and the  $z$ -axis, which also generally corresponds to thickness, corresponds to the canonical  $t$ -axis.

The various meshes employed are conforming for human convenience. The fluid domain is entirely equi-axed. The FE portion is constructed using the coordinates of the bottom of the plate elements as a foundation and extending down a specified number of layers in the  $-z$  direction. The CA portion is constructed by specifying a factor by which plate length is multiplied—the cube of this value is the fluid volume. The CA nodes that are wholly inside the FE fluid domain and not needed are simply removed from the index sets and ignored.

### B. NUMERICAL INTEGRATION

Exact integration is performed using Gauss-Lobatto quadrature. Under-integration of the shear terms of plate elements is performed using Gauss-Legendre quadrature. Because the integration points for Gauss-Lobatto quadrature are still nodal (interpolation)

points, terms in  $K_s$  that are products of different cardinal interpolation functions will be uniformly zero, resulting in a too sparse shear stiffness matrix.

A numerical experiment comparing the static deflections calculated using the two different quadrature rules for calculating an under-integrated  $K_s$  with both theoretical static deflection and that resulting from an exactly integrated  $K_s$  was conducted. For a clamped plate of dimensions 0.3048m x 0.3048m x 0.00635m (12in x 12in x 1/4in), elastic modulus 70 GPa, Poisson's ratio 0.3 subjected to a concentrated load of 1000N, predicted static deflection of the center of the plate is 0.31697mm [33]. Calculated deflection for Gauss-Lobatto quadrature was 0.0945mm; for Gauss-Legendre quadrature: 0.3086mm; for exact integration of  $K_s$ : 0.0325mm. Clearly, Gauss-Legendre quadrature is a better choice for under-integration of the shear stiffness matrix in this application.

### **C. APPLICATION OF BOUNDARY CONDITIONS AND EXTERNAL LOADS**

Boundary conditions and external loads are applied nodally. For boundary conditions, rows of the mass and stiffness matrices corresponding to constrained dofs are zeroed; their diagonal elements are set to 1, and the corresponding element in the right-hand-side vector is set to the constrained value. External loads must first be converted to units of force and then distributed to the appropriate elements of the right-hand-side vector. For the pressure exerted by the fluid domain on the wet side of our notional plate, the nodal pressure vector is multiplied by a two-dimensional interpolation (mass) matrix to convert it to a force vector. For application to the DG structure, that resulting vector is decomposed to reflect the number of dof found at each geometric position; in this way, the force applied at a point "shared" by four separate discontinuous elements will be parsed among them equally.

## D. MATLAB SPECIFICS

### 1. Sparse Matrices

The lumped mass and global stiffness matrices are sparse, the former is diagonal and the latter is block tri-diagonal. MATLAB does allow assembly of a full stiffness matrix followed by `K=sparse(K)`, but the calculation and assembly designed from the outset to be sparse is a more efficient use of computing resources. To do so, the global indices of each element of the collection of elemental  $K$  matrices are stored in vectors `i_v` and `j_v` with the corresponding values stored in `k_v`. After the elemental calculations are complete, `K=sparse(i_v, j_v, k_v)` returns the sparse global stiffness matrix.

### 2. CA Implementation

The CA portion of the fluid model is updated using sets of node indices. The domain is comprised of  $N$  nodes where  $N = N_x \times N_y \times N_z$ . In this work  $N_x = N_y = N_z =$ an odd number; this keeps the eight corners of the domain in the odd set and is convenient, not required. The CA coordinate array is used to match node numbers of corresponding geometric points between the two fluid domains; an  $N \times 6$  array named `neighbor` tracks the eponymous relations by node number with a 0 entry indicating the end of the domain in that direction, the velocity potential in CA domain is described by the two  $N$ -vectors, `phi` and `phiold`. A large portion of the CA set-up is the definition of index sets for these two vectors. The largest two are the odd and even interior points, `oint` and `eint`. The six faces and twelve edges of the rectangular fluid domain are likewise split into odd and even index sets. This infrastructure makes an iteration of the CA rule a simple matter of calling subroutines `UpdateFace` or `UpdateEdge` with arguments of `phiold`, `neighbor`, the index set of the area to be updated, and a flag indicating the boundary condition to be employed.

## E. MATERIAL PROPERTIES

The following tables specify the material properties used for various calculations in this study.

Property	Value
$G_{xz}$	345 MPa
$G_{yz}$	345 MPa

Table 2: Material Properties of aluminum honeycomb, From [41], [42]

Property	Value
E	72.4 GPa
$\nu$	0.3

Table 3: Material Properties of aluminum skins, From [41], [42]

Property	Value
$E_x$	17.24 GPa
$\rho$	$2020 \frac{\text{kg}}{\text{m}^3}$
$\nu_{xy}$	0.3
$G_{xy}$	6.619 GPa
$E_y$	17.24 GPa
$E_z$	7.929 GPa
$\nu_{xz}$	0.24
$\nu_{yz}$	0.24
$G_{xz}$	2.896 GPa
$G_{yz}$	2.896 GPa

Table 4: Material Properties of E-glass, From [56]

Property	Value
$E$	8.34 GPa
$\rho$	$1180 \frac{\text{kg}}{\text{m}^3}$
$\nu$	0.28

Table 5: Material Properties of Epoxy Resin, From [57]

THIS PAGE INTENTIONALLY LEFT BLANK

## LIST OF REFERENCES

- [1] J. Nitsche, “Über ein Variationsprinzip zur Lösung von Dirichlet-Problemen bei Verwendung von Teilräumen, die keinen Randbedingungen unterworfen sind,” *Abhandlungen aus dem Mathematischen Seminar der Univ. Hamburg*, vol. 36, no. 1, pp. 9–15, 1971.
- [2] J. Douglas, Jr. and T. Dupont, “Interior penalty procedures for elliptic and parabolic Galerkin methods,” in *Computing Methods in Applied Sciences and Engineering*, pp. 207–216, New York: Springer-Verlag, 1975.
- [3] D. N. Arnold, “An interior penalty finite element method with discontinuous elements,” *SIAM Journal on Numerical Analysis*, vol. 19, no. 4, pp. 742–760, 1982.
- [4] G. A. Baker, “Finite element methods for elliptic equations using nonconforming elements,” *Mathematics of Computation*, vol. 31, pp. pp. 45–59, Jan. 1977.
- [5] M. F. Wheeler, “An elliptic collocation-finite element method with interior penalties,” *SIAM Journal on Numerical Analysis*, vol. 15, no. 1, pp. 152–161, 1978.
- [6] D. N. Arnold, F. Brezzi, B. Cockburn, and D. Marini, “Discontinuous Galerkin methods for elliptic problems,” in *Discontinuous Galerkin methods: Theory, Computation and Applications*, pp. 89–101, Berlin: Springer, 2000.
- [7] D. N. Arnold, F. Brezzi, B. Cockburn, and L. D. Marini, “Unified analysis of discontinuous Galerkin methods for elliptic problems,” *SIAM Journal on Numerical Analysis*, vol. 39, no. 5, pp. 1749–1779, 2002.
- [8] P. Castillo, “Performance of discontinuous Galerkin methods for elliptic PDEs,” *SIAM Journal on Scientific Computing*, vol. 24, no. 2, pp. 524–547, 2003.
- [9] F. Brezzi, B. Cockburn, L. D. Marini, and E. Suli, “Stabilization mechanisms in discontinuous Galerkin finite element methods,” *Computer Methods in Applied Mechanics and Engineering*, vol. 195, no. 25-28, pp. 3293–3310, 2006.
- [10] B. Riviere, S. Shaw, M. F. Wheeler, and J. R. Whiteman, “Discontinuous Galerkin finite element methods for linear elasticity and quasistatic linear viscoelasticity,” *Numerische Mathematik*, vol. 95, no. 2, pp. 347–376, 2003.
- [11] P. Hansbo and M. G. Larson, “Discontinuous Galerkin methods for incompressible and nearly incompressible elasticity by Nitsche’s method,” *Computer Methods in Applied Mechanics and Engineering*, vol. 191, no. 17, pp. 1895–1908, 2002.

- [12] L. Noels and R. Radovitzky, “A general discontinuous Galerkin method for finite hyperelasticity. formulation and numerical applications,” *International Journal for Numerical Methods in Engineering*, vol. 68, no. 1, pp. 64–97, 2006.
- [13] L. Noels and R. Radovitzky, “A new discontinuous Galerkin method for non-linear mechanics,” in *47th AIAA/ASME/ASCE/AHS/ASC Structures, Structural Dynamics and Materials Conference, May 1, 2006 - May 4*, vol. 9, (Newport, RI, United States), pp. 6290–6297, American Institute of Aeronautics and Astronautics Inc, May 2006.
- [14] L. Noels, “Alternative approaches for the derivation of discontinuous Galerkin methods for nonlinear mechanics,” *Journal of Applied Mechanics*, vol. 74, no. 5, pp. 1031–1036, 2007.
- [15] D. N. Arnold, F. Brezzi, and L. D. Marini, “A family of discontinuous Galerkin finite elements for the Reissner-Mindlin plate,” *Journal of Scientific Computing*, vol. 22-23, pp. 25–45, 2005.
- [16] F. Celiker, B. Cockburn, S. Guzey, R. Kanpady, S.-C. Soon, H. K. Stolarski, and K. Tamma, “Discontinuous Galerkin methods for Timoshenko beams,” in *Numerical Mathematics and Advanced Applications, ENUMATH 2003* (M. Feistauer, V. Dolejsi, P. Knoblock, and K. Najzar, eds.), (Germany), pp. 221–231, Springer, August, 2003 2004.
- [17] G. Engel, K. Garikipati, T. Hughes, M. Larson, L. Mazzei, and R. Taylor, “Continuous/discontinuous finite element approximations of fourth-order elliptic problems in structural and continuum mechanics with applications to thin beams and plates, and strain gradient elasticity,” *Computer Methods in Applied Mechanics and Engineering*, vol. 191, no. 34, pp. 3669–3750, 2002.
- [18] A. Lew, A. Ten Eyck, and R. Rangarajan, “Some applications of discontinuous Galerkin methods in solid mechanics,” in *Proceedings of the IUTAM Symposium on Theoretical, Computational and Modelling Aspects of Inelastic Media* (B. Daya Reddy, ed.), Springer, 2008.
- [19] F. Stan, “Discontinuous Galerkin method for interface crack propagation,” *International Journal of Material Forming*, vol. 1, pp. 1127–1130, 2008.
- [20] F. Stan, “Simulation of delamination using discontinuous Galerkin finite element methods and cohesive models,” *Key Engineering Materials*, vol. 417, pp. 501–504, 2010.
- [21] R. Liu, M. F. Wheeler, and C. N. Dawson, “A three-dimensional nodal-based implementation of a family of discontinuous Galerkin methods for elasticity problems,” *Computers and Structures*, vol. 87, pp. 141–150, February 2009.

- [22] J. Mergheim, E. Kuhl, and P. Steinmann, “A hybrid discontinuous Galerkin/interface method for the computational modelling of failure,” *Communications in Numerical Methods in Engineering*, vol. 20, no. 7, pp. 511–519, 2004.
- [23] L. G. Olson and K.-J. Bathe, “Analysis of fluid-structure interactions. a direct symmetric coupled formulation based on the fluid velocity potential,” *Computers and Structures*, vol. 21, no. 12, pp. 21–32, 1985.
- [24] J. Lindquist, *Unstructured High-order Galerkin-Temporal-Boundary Methods for the Klein-Gordon Equation with Non-Reflecting Boundary Conditions*. PhD., Naval Postgraduate School, 2010.
- [25] B. Chopard and M. Droz, *Cellular Automata Modeling of Physical Systems*. Cambridge: Cambridge University Press, 1998.
- [26] B. Chopard, “A cellular automata model of large-scale moving objects,” *Journal of Physics A: Mathematical and General*, vol. 23, no. 10, p. 1671, 1990.
- [27] R. A. Krutar, S. K. Numrich, R. K. Squier, J. Pearson, and G. Doolen, “Computation of acoustic field behavior using a lattice gas model,” in *Proceedings of Oceans '91, October 1, 1991 - October 3*, vol. 1, (Honolulu, HI, USA), pp. 446–452, Publ by IEEE, 1991.
- [28] Y. W. Kwon and S. Hosoglu, “Application of Lattice Boltzmann method, finite element method, and cellular automata and their coupling to wave propagation problems,” *Computers and Structures*, vol. 86, no. 7-8, pp. 663–670, 2008.
- [29] R. P. Conner, “Fluid structure interaction effects on composites under low velocity impact,” M.S. thesis, Naval Postgraduate School, 2012.
- [30] B. Cockburn and C.-W. Shu, “Local discontinuous Galerkin method for time-dependent convection-diffusion systems,” *SIAM Journal on Numerical Analysis*, vol. 35, no. 6, pp. 2440–2463, 1998.
- [31] F. X. Giraldo, “Element-based Galerkin Methods (MA4245: Mathematical Principles of Galerkin Methods).” unpublished.
- [32] Y. W. Kwon and H. Bang, *The Finite Element Method using MATLAB*. CRC Mechanical Engineering Series, Boca Raton, FL: CRC Press, 1997.
- [33] S. Timoshenko and S. Woinowsky-Krieger, *Theory of Plates and Shells*. New York: McGraw-Hill Book Company, second ed., 1959.
- [34] T. S. Lok and Q. H. Cheng, “Bending and forced vibration response of a clamped orthotropic thick plate and sandwich panel,” *Journal of Sound and Vibration*, vol. 245, no. 1, pp. 63–78, 2001.

- [35] M. Ainsworth, “A posteriori error estimation for discontinuous Galerkin finite element approximation,” *SIAM Journal on Numerical Analysis*, vol. 45, no. 4, pp. 1777–1798, 2007.
- [36] Y. Epshteyn and B. Riviere, “Estimation of penalty parameters for symmetric interior penalty Galerkin methods,” *Journal of Computational and Applied Mathematics*, vol. 206, no. 2, pp. 843–872, 2007.
- [37] K. Shahbazi, “An explicit expression for the penalty parameter of the interior penalty method,” *Journal of Computational Physics*, vol. 205, no. 2, pp. 401–407, 2005.
- [38] M. Ainsworth and R. Rankin, “Technical note: A note on the selection of the penalty parameter for discontinuous Galerkin finite element schemes,” *Numerical Methods for Partial Differential Equations*, vol. 28, no. 3, pp. 1099–1104, 2012.
- [39] M. Ainsworth and R. Rankin, “Fully computable error bounds for discontinuous Galerkin finite element approximations on meshes with an arbitrary number of levels of hanging nodes,” *SIAM Journal on Numerical Analysis*, vol. 47, no. 6, pp. 4112–4141, 2010.
- [40] Y. Kwon, “Multiscale and multilevel modeling of composites,” in *Multiscale Modeling and Simulation of Composite Materials and Structures*, pp. 165–202, New York: Springer, 2008.
- [41] L. A. Schmit, Jr. and G. R. Monforton, “Finite deflection discrete element analysis of sandwich plates and cylindrical shells with laminated faces,” *AIAA Journal*, vol. 8, pp. 1454–1461, August 1970.
- [42] H. H. Kanematsu, Y. Hirano, and H. Iyama, “Bending and vibration of CFRP-faced rectangular sandwich plates,” *Composite Structures*, vol. 10, no. 2, pp. 145–163, 1988.
- [43] Y. Kwon and L. Craugh, “Progressive failure modeling in notched cross-ply fibrous composites,” *Applied Composite Materials*, vol. 8, no. 1, pp. 63 – 74, 2001.
- [44] S. J. Farlow, *Partial Differential Equations for Scientists and Engineers*. New York: Dover Publications, Inc., 1993.
- [45] M. C. Junger and D. Feit, *Sound, Structures, and Their Interaction*. Cambridge, MA: The MIT Press, 1986.
- [46] S. Hosoglu, “Cellular automata: An approach to wave propagation and fracture mechanics problems,” M.S. thesis, Naval Postgraduate School, 2006.
- [47] R. R. Craig and A. J. Kurdila, *Fundamentals of Structural Dynamics*. Hoboken, NJ: Wiley, 2006.

- [48] Y. Kwon, "Study of fluid effects on dynamics of composite structures," *Journal of Pressure Vessel Technology, Transactions of the ASME*, vol. 133, no. 3, 2011.
- [49] A. C. Owens, J. M. Didoszak, A. S. Kwon, and Y. W. Kwon, "Underwater impact of composite structures," in *ASME 2010 Pressure Vessels and Piping Division/K-PVP Conference, PVP2010, July 18, 2010 - July 22, 2010*, vol. 4, (Bellevue, WA, United states), pp. 231–240, 2010.
- [50] Y. Kwon, M. Violette, R. McCrillis, and J. Didoszak, "Transient dynamic response and failure of sandwich composite structures under impact loading with fluid structure interaction," *Applied Composite Materials*, pp. 1–20, 2012. in press.
- [51] Y. W. Kwon and M. A. Violette, "Damage initiation and growth in laminated polymer composite plates with fluid-structure interaction under impact loading," *The International Journal of Multiphysics*, vol. 6, pp. 29–42, March 2012.
- [52] A. C. Ugural and S. K. Fenster, *Advanced Strength and Applied Elasticity*. Upper Saddle River, NJ: Prentice Hall PTR, 1995.
- [53] H. M. Hilber, T. J. R. Hughes, and R. L. Taylor, "Improved numerical dissipation for time integration algorithms in structural dynamics," *Earthquake Engineering and Structural Dynamics*, vol. 5, no. 3, pp. 283–292, 1977.
- [54] T. J. R. Hughes, *The Finite Element Method: Linear Static and Dynamic Finite Element Analysis*. Mineola, NY: Dover Publications, 2000.
- [55] C. C. Chien, C. S. Yang, and J. H. Tang, "Three-dimensional transient elastodynamic analysis by a space and time-discontinuous Galerkin finite element method," *Finite Elements in Analysis and Design*, vol. 39, pp. 561–580, April 2003.
- [56] R. D. McCrillis, "Dynamic failure of sandwich beams with fluid-structure interaction under impact loading," M.S. thesis, Naval Postgraduate School, 2010.
- [57] T. R. Greene, "Analytical modeling of composite-to-composite (scarf) joints in tension and compression," M.S. thesis, Naval Postgraduate School, 2007.

THIS PAGE INTENTIONALLY LEFT BLANK

## INITIAL DISTRIBUTION LIST

1. Defense Technical Information Center  
Ft. Belvoir, VA
2. Dudley Knox Library  
Naval Postgraduate School  
Monterey, CA
3. Distinguished Professor Young W. Kwon  
Naval Postgraduate School  
Monterey, CA
4. Professor Garth V. Hobson  
Naval Postgraduate School  
Monterey, CA
5. Professor Clyde Scandrett  
Naval Postgraduate School  
Monterey, CA
6. Professor Francis X. Giraldo  
Naval Postgraduate School  
Monterey, CA
7. Associate Professor Joshua H. Gordis  
Naval Postgraduate School  
Monterey, CA
8. Erik A. Rasmussen  
Head, Structures and Composites Division Code 65  
NSWC Carderock Division
9. Douglas Loup  
Structures and Composites Division Code 65  
NSWC Carderock Division
10. Frederick A. Costanzo  
Head, Underwater Explosions Research and Development Branch  
NSWC Carderock Division
11. CDR Linda E. Craugh  
United States Naval Academy  
Annapolis, MD